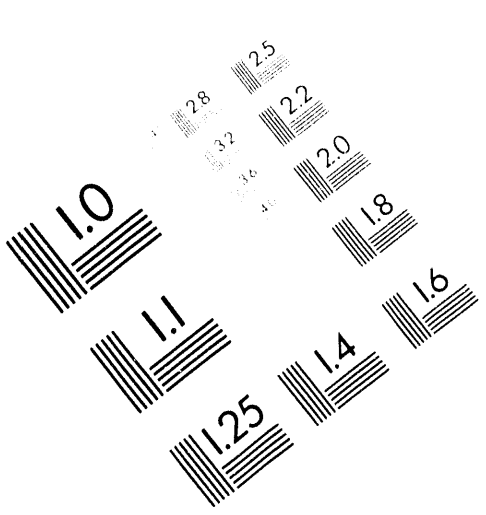


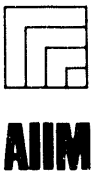

**AIIM**

**Association for Information and Image Management**

1100 Wayne Avenue, Suite 1100
Silver Spring, Maryland 20910
301/587-8202

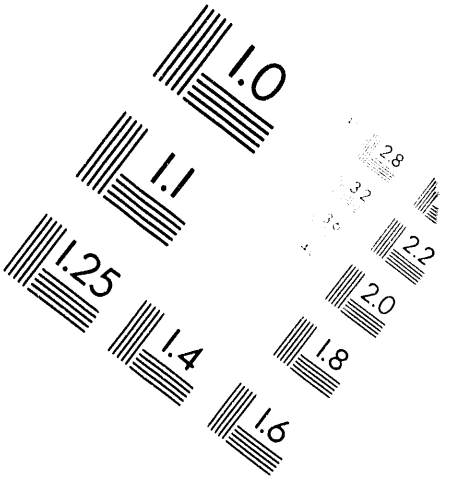


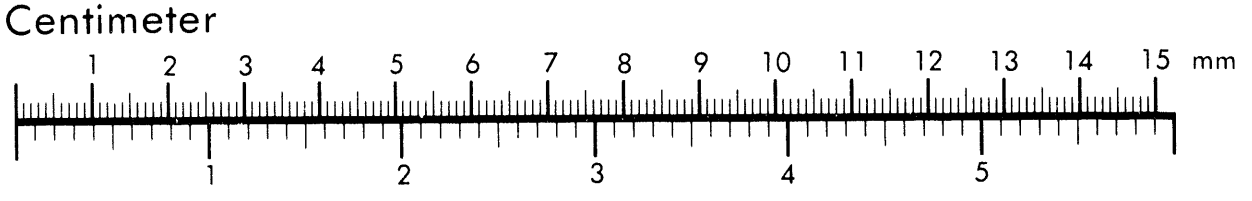


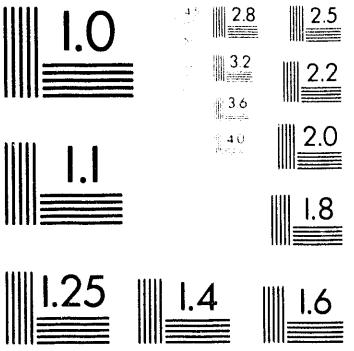


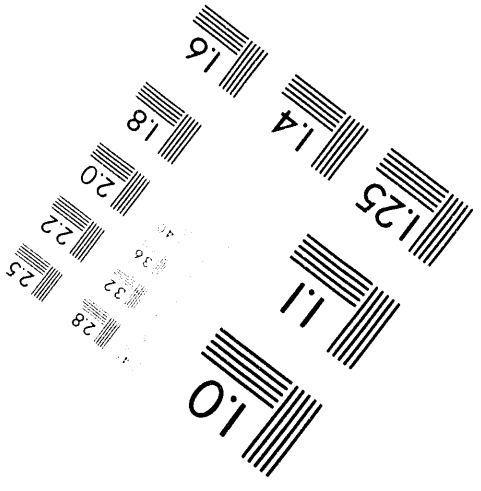


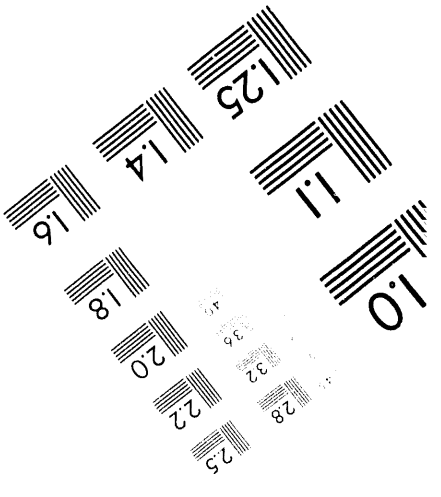


MANUFACTURED TO AIIM STANDARDS
BY APPLIED IMAGE, INC.

1 of 2

M-1
1

92PC92104-TPR-5
DOE/PC/92104--T5

# ADVANCED THERMALLY STABLE JET FUELS

## Technical Progress Report
## July 1993 - September 1993

H.H. Schobert, S. Eser, C. Song, P.G. Hatcher, P.M. Walsh, M.M. Coleman

Contributions from:

R. Arumugam, J. Bortiatynski, D. Clifford, K. Gergova, W.-C. Lai, L. Hou, J. Li, D. McKinney, Y. Peng, P. Saghani, J. Stallman, E. Yoon, and J. Yu

December 1993

Prepared for U.S. Department of Energy
under
Contract No. DE-FG22-92PC92104

PENNSTATE

College of Earth and Mineral Sciences

M-1
1

92PC92104-TPR-5

# ADVANCED THERMALLY STABLE JET FUELS

## Technical Progress Report
## July 1993 - September 1993

H.H. Schobert, S. Eser, C. Song, P.G. Hatcher, P.M. Walsh, M.M. Coleman

Contributions from:

R. Arumugam, J. Bortiatynski, D. Clifford, K. Gergova, W.-C. Lai, L. Hou, J. Li, D. McKinney, Y. Peng, P. Saghani, J. Stallman, E. Yoon, and J. Yu

December 1993

Prepared for U.S. Department of Energy
under
Contract No. DE-FG22-92PC92104

PENNSTATE

College of Earth and Mineral Sciences

92PC92104-TPR-5

# ADVANCED THERMALLY STABLE JET FUELS

## Technical Progress Report
## July 1993 - September 1993

H.H. Schobert, S. Eser, C. Song, P.G. Hatcher, P.M. Walsh, M.M. Coleman

Contributions from:

R. Arumugam, J. Bortiatynski, D. Clifford, K. Gergova, W.-C. Lai, L. Hou, J. Li, D. McKinney, Y. Peng, P. Saghani, J. Stallman, E. Yoon, and J. Yu

December 1993

Prepared for U.S. Department of Energy
under
Contract No. DE-FG22-92PC92104

PENNSTATE

(814) 865-6511
FAX: (814) 865-3075

Fuel Science Program
Department of Materials Science
& Engineering
College of Earth and Mineral Sciences

The Pennsylvania State University
209 Academic Projects Building
University Park, PA 16802-2303

January 12, 1994

Dr. Shelby Rogers
U.S. Department of Energy
922-H PM 10SR
PETC
P.O. Box 10940
Pittsburgh, PA 15236-0940

Dear Dr. Rogers:

Enclosed is a new "Table of Contents" to the latest Jet Fuels Report. I seemed to have gotten some of the page numbers confused. I am sorry for any inconvenience that this may have caused.

Sincerely,

Jackie Kunes
Secretary

/jsk

## OBJECTIVES

The Penn State program in advanced thermally stable coal-based jet fuels has five broad objectives: 1) development of mechanisms of degradation and solids formation; 2) quantitative measurement of growth of sub-micrometer and micrometer-sized particles suspended in fuels during thermal stressing; 3) characterization of carbonaceous deposits by various instrumental and microscopic methods; 4) elucidation of the role of additives in retarding the formation of carbonaceous solids; and 5) assessment of the potential of production of high yields of cycloalkanes by direct liquefaction of coal.

## SUMMARY

An exploratory study was conducted to investigate the pyrolysis of *n*-butylbenzene in a flow reactor at atmospheric pressure. A number of similarities to trends previously observed in high-pressure static reactions were identified. In both cases, ethylene and propylene appear to go through a maximum and then decline. In both cases, the same major compounds are formed, including benzene, toluene, ethylbenzene, styrene, methylstyrene, naphthalene, biphenyl, $C_3$-benzenes, and $C_4$-benzenes. However, there are also some differences between the two reaction systems. For example, styrene was the most abundant product in the flow reactions, whereas toluene and ethylbenzene dominate among the microautoclave products. Further work will be needed to elucidate the chemistry in the flow reactor system and to compare fully the flow reactions with the microautoclave (static reactions).

The product distribution from pyrolysis of *n*-tetradecane at 400° and 425°C was investigated. Modelling studies show that the product distribution cannot be predicted by known reaction mechanisms reported in the literature, such as the Kossiakoff-Rice mechanism or the Fabuss-Smith-Satterfield mechanism. Modelling work based on our own proposed mechanisms is now in progress.

The critical temperatures of a suite of petroleum- and coal-derived jet fuels were measured by a rapidly heating sealed tube method. The measured results appear satisfactory and exhibit good reproducibility.

Work has continued on refining the measurements of deposit growth for stressing mixtures of coal-derived JP-8C with tetradecane. Current work has given emphasis to the initial stages of fuel decomposition and the onset of deposition. The results to date suggest that a simple model of a first-order decomposition step leading to reactive intermediates, followed by reaction of the intermediates to give particles and settling of the particles, may

be sufficiently detailed to describe deposit formation and provide a quantitative framework for calculation of rate coefficients for the rate-determining step.

Pretreatment of JPTS fuel with PX-21 activated carbon (50 mg of PX-21 in 15 mL JPTS) delayed degradation and prevented carbon deposition during thermal stressing at 425°C for 5 h in nitrogen and air atmospheres. To delay degradation at 450°C requires 300 mg PX-21 per 15 mL fuel. The carbonaceous solid formed during stressing is deposited on the activated carbon surface.

Clear indications of initial and subsequent deposit formation on different metal surfaces have been indentified for thermal stressing of dodecane. Nickel surface catalyzes deposition by formation of filamentous carbon, and copper surface by formation of fibrous carbon. A stainless steel surface appears to have no catalytic effects on the deposit formation process. Eventually the metal surface becomes covered by carbon layers with circular or oval rings on the carbon layers. The ring-formation process is probably related to steady-state growth of the deposit on all the available surface.

Seven additives were tested for their ability to retard decomposition of dodecane at 450°C under nitrogen. Of these seven compounds, 9,10-dihydrophenanthrene and 1,2,3,4-tetrahydroquinoline gave superior results. The superior performance of 9,10-dihydrophenanthrene is due to the fact that it has excellent thermal stability at 450°C and good resonance stabilization of the radical scavenger.

Nuclear magnetic resonance data for Dammar resin indicates that structures proposed in the literature are not entirely correct. A new structural composition must be proposed for polycadinene-like resin polymers like Dammar resin. Considering the fact that the Dammar resin is very similar to the resinite from the Blind Canyon bituminous coal, significant progress have been made toward developing a working structural model for this component of a potential feedstock for jet fuel production.

# TECHNICAL PROGRESS

## Task 1. Investigation of the Quantitative Degradation Chemistry of Fuels

*1. Exploratory Study of Gas Phase Pyrolysis of n-Butylbenzene at Atmospheric Pressure in Flow Reactor (Contributed by Ying Peng)*

Introduction

Previous studies have been conducted at elevated pressures, with 100 psi ultra-high purity (UHP) $N_2$ (cold) as the most often used operating condition. The present study was conducted with the aim of comparing the pyrolysis reactions of alkylbenzenes (*n*-butylbenzene in the current work) stressed under elevated pressures and at the atmospheric pressure.

The reaction mechanisms and kinetics of most short-chain alkylbenzenes have been studied at high temperature, short residence times and in the gas phase (1). This operating condition enhances the primary reactions of the substrate molecule, minimizing the complex secondary reactions, therefore simplifying the reaction mechanism and kinetics. Also, it is recognized that β-bond scission is promoted in an atmospheric pressure reaction relative to H-transfer reactions (2). The present work was conducted at three different temperatures, 600°C, 550°C and 500°C. It was hoped that, by extrapolating the high-temperature gas-phase reaction to the complex supercritical reaction condition (450°C, 100 psi UHP $N_2$) typically used for alkylbenzene stressing by taking into account the pressure effect, a more detailed reaction mechanism could be elucidated and a model describing the complex reaction kinetics could be established.

Experimental

*n*-Butylbenzene was pyrolyzed under 600°C, 550°C and 500°C in a Xytel Automat IV flow reactor shown in Figure 1, assembled by Xytel Engineering. It was designed for semi-unattended operation. The reactor is constructed of stainless steel with three heating zones (zone 2, 3 and 4) and one preheating zone (zone 1). The volume of the reactor is 24.83 mL. There are three gas delivery systems. Two of them are for $N_2$ and one is for air. Only one $N_2$ line is used in this study. $N_2$ is used in the study as a diluent gas. *n*-Butylbenzene is provided through a 50 mL feed supply syringe and the 5 mL feeding syringe to the reactor. Manual and computer-controlled electronic solenoid valves combine with the mass flow meters to isolate and distribute the required gas flow through the system. The product isolation and analysis network consists of a liquid product receiver (cooling trap) and a gaseous product receiver. Gaseous products are collected after reaction into gas bags by water displacement. The amount

of product gas obtained can be calculated by the mass of water displaced and recorded by the balance. All these data are collected and stored by the computer. The amount of liquid products can be obtained by weighing the liquid receiver before and after the reaction. The solid formation is neglected because of the residence times of the reactions are considered to be short.

The gaseous and liquid products are identified and analyzed according to the methods described previously (3).

Results and Discussion

1. The Experiment Profiles. A total of 23 preliminary experiments, lumped into 5 groups, have been conducted on the Xytel Equipment. Groups 1 and 2 tested the effects of changing the flow rate of $N_2$ and *n*-butylbenzene. Groups 3, 4 and 5 were carried out with the intent of varying the reaction temperatures and residence times of *n*-butylbenzene while keeping the molar ratio of $N_2$ and *n*-butylbenzene unchanged. Table 1 shows the experimental parameters and raw data obtained from the 23 runs.

2. Residence time calculation. Residence time of each run is determined by the volume of the reactor (V, mL) divided by the total volumetric flow (V', mL/s). Volumetric flow through the reactor depends on the flow rate of *n*-butylbenzene ($R_{NB}$, ml/min), flow rate of $N_2$ ($R_{N_2}$) and total molar density of the two feeds, and calculated from the following equation:

$$V' = (n_1 + n_2) / (\rho_1 + \rho_2) \qquad (1)$$

where $\rho_1$ (mol/mL) is the molar density of *n*-butylbenzene, $\rho_2$ (mol/mL) is the molar density of $N_2$, $n_1$ is the molar flow rate of *n*-butylbenzene (mol/s) and $n_2$ is the molar flow rate of $N_2$ (mol/s). From the ideal gas law,

$$\rho_1 = \rho_2 = P / RT \qquad (2)$$

The molar flow rate of *n*-butylbenzene (mol/s) can be determined from:

$$n_1 = R_{NB} \times 0.86 / (60 \times 134) \qquad (3)$$

The molar flow rate of $N_2$ (mol/s) can be determined from:

$$n_2 = R_{N2} / (22400 \times 60) \qquad (4)$$

Therefore, the residence time $\tau$ can be calculated as follows:

$$\tau = V/V' = (\rho_1 + \rho_2) \times V / (n_1 + n_2) \qquad (5)$$

3. Product distribution and analysis. It should mentioned that only preliminary data are reported here. Some make-up experiments and data analysis will be completed and reported in future reports. Figures 2, 3 and 4 show the variations of the rates of formation of some major gaseous and liquid products with $N_2$ flow rate. It can be seen that for most of the product compounds, the amount formed per minute declines as the $N_2$ flow rate is increased. The amount formed per minute of $C_4$ gaseous species seems to be increasing as the rate of $N_2$ increases. But, because their concentrations are relatively limited compared to other gaseous species, these fluctuations might be in the range of experimental error. The other trend worth mentioning is that of ethylene and propylene. Similar to the situations in the tubing bomb reactions where elevated pressures are used, they go through a maximum as the rate of $N_2$ is increased. Far fewer compounds are detected in the liquid products, as compared with the tubing bomb reactions, although the major compounds identified are the same, such as benzene, toluene, ethylbenzene, styrene, $C_3$-benzene, methylstyrene, $C_4$-benzene, naphthalene, and biphenyl. Among them, styrene stands out as the most abundant. This is a significant difference compared to pressurized reactions, where toluene and ethylbenzene comprised a high portion of liquid and styrene was always less important. Figures 5, 6 and 7 show the variations of some major gaseous and liquid products with varying *n*-butylbenzene flow rate. Monotonic increasing of each product with the concentration of butylbenzene has been observed. Similar to the above, styrene shows highest amount among the products.

The pyrolysis of *n*-butylbenzene was also conducted at 600°C, 550°C and 500°C. Under similar molar ratio of 0.8 (*n*-butylbenzene to $N_2$), different flow rate combinations of the two feed materials were selected (Table 1) in order to vary the residence time of each run. The residence time range chosen was from 4.5 s. to 3.63 min. The results are shown in Figures 8 to 14. It is obvious from these Figures that the rates of formation of all species (mol/min) decrease after a relatively long reaction time. A similar type of rate inhibition effect was observed in tubing bomb reactions where the rates of decomposition of the substrate compounds decrease with thermal stressing time. At 600°C, the decreasing trends for most of compounds are monotonic, as can be seen from Figures 8, 9 and 10. For 550°C and 500°C, the rates of most of species go through a maximum before finally declining at long residence times. The reason for this phenomenon is not fully understood. Further work needs to be done to clarify or elucidate it.

References

1 Freund, H.; Olmstead, W.N., "Detailed Chemical Kinetic Modeling of Butylbenzene Pyrolysis". International J. of Chem. Kinet., 1989, 21, 561.

2 Fabuss, B.M.; Smith J.O.; Satterfield, C.N. "Thermal Cracking of Pure and Saturated Hydrocarbons. Adv. Petrol. Chem. Refin., 1964, 9, 158.

3 Schobert, H.H.; Eser, S.; Song, C.; Hatcher, P.G.; Walsh, P.M.; Coleman, M.M., Advanced Thermally Stable Jet Fuels, Technical Progress Report, August 1992-October 1992, Prepared for U.S. Department of Energy under Contract No. DE-FG22-92PC92104.

## 2. *Product Distribution of the Pyrolysis of n-Tetradecane at 400°C and 425°C. (Contributed by Wei-Chuan Lai and Chunshan Song)*

### Introduction

This study was undertaken to complement our previous study of the pyrolysis of n-tetradecane (n-$C_{14}$) at 450°C for 6–480 min, which has led to the 1) the proposed reaction mechanisms of the condensed-phase pyrolysis of n-$C_{14}$ at elevated pressures; 2) the mechanisms accounting for the characteristic product distribution patterns and their changes with residence time; and 3) the observations of the fate of olefinic products and formation of cyclic compounds during the long-duration pyrolysis (Song et al., 1993; Schobert et al., 1993a). The reaction temperatures in this work are 400°C and 425°C, which are lower than that of previous study, 450°C. This section will present the detailed product distribution of the pyrolysis of n-$C_{14}$ at 400°C and 425°C, and the global kinetic parameters of n-$C_{14}$ pyrolysis. The modelling work based on the mechanism of Fabuss-Smith-Satterfield (1964a) is also presented in this report. It was found that the product distribution observed under the conditions used in our work cannot be predicted by the known reaction mechanisms in the literature such as those proposed by Kossiakoff and Rice (1943) and Fabuss-Smith-Satterfield (1964a). The modelling work based on our proposed reaction mechanisms is in progress and will be reported in the future.

### Experimental

Aldrich reagent-grade normal tetradecane, $CH_3(CH_2)_{12}CH_3$, with purity of 99+ % (MW: 198.4; d: 0.763 g/mL) was used as received for all the pyrolysis experiments. The pyrolyses were performed in 25 mL tubing bomb reactors at 400°C or 425°C for a heating

period of 21–240 min under an initial pressure of 0.69 MPa UHP $N_2$ (cold). After being loaded with 5 mL sample, the reactor was first leak-tested and then purged repetitively (6 times) with 6.9 MPa UHP $N_2$ to remove oxygen or air in the reactor or dissolved in the sample. The reactor pressure and temperature were monitored immediately after the reactor was plunged into the sandbath. The sample reached within 4°C of the desired pyrolysis temperature in about 4–6 min. The reactor was removed from the fluidized sandbath after the desired stressing time, and immediately quenched in a cool water bath. The products were collected and separated into gas, liquid, and solid deposits immediately after the reactor was cool enough. The fresh gaseous and liquid products were then analyzed by GC and GC-MS.

The gaseous products were analyzed using a Perkin-Elmer Autosystem GC equipped with two detectors, a thermal conductivity detector and a flame ionization detector. The liquid products were analyzed on an HP 5890 Series II GC coupled with an HP 5971A Mass Selective Detector and quantified by a Perkin-Elmer GC 8500. More analytical details may be found found elsewhere (Lai and Song, 1993; Song et al., 1993).

## Results and Discussion

1. Decomposition kinetic parameters. The detailed products for the pyrolysis of *n*-$C_{14}$ at 400°C and 425°C are reported in Table 2, where only major individual reaction products are presented. The hydrocarbon products are expressed as molar percentage of the initial amounts of reactants (*n*-$C_{14}$). The major products include $C_1$–$C_4$ gaseous yields and liquid yields such as alkanes, alkenes, and cycloalkanes. We approximated the thermal decomposition by a first-order relation as shown in Equation (1).

$$-\frac{dC}{dt} = kC \tag{1}$$

where C is the reactant concentration, t is the reaction time, and k is the first-order rate constant. The rate constant can then be expressed as a function of the reactant conversion ($\alpha$, the fraction of reactant reacted) as shown in Equation (2).

$$k = \frac{1}{t} \ln \frac{1}{1-\alpha} \tag{2}$$

As mentioned earlier, the preheat or heat-up (from room temperature to the desired reaction temperature) time is about 4–6 min, and has to be accounted for in calculating an adjusted (effective) reaction time. From least-squares regression, the calculated pseudo-first-order rate

constants at 400°C, 425°C, and 450°C, are 0.000734, 0.00580, 0.02405 $min^{-1}$, respectively. The relation between activation energy ($E_a$) and the rate constant (k) is given by the Arrhenius equation:

$$k = A\, e^{-E_a / RT} \qquad (3)$$

where A is the Arrhenius frequency factor (often called the pre-exponential factor), R is the gas constant, and T is the absolute temperature in K. Figure 15 presents the Arrhenius plot (ln k vs 1/T). Determined from the Arrhenius plot, the activation energy ($E_a$) and the Arrhenius frequency factor (A) are 67.6 kcal/mol and $7.17 \times 10^{18}$ $min^{-1}$, respectively. The overall reaction kinetics, i.e., $E_a$ = 67.6 kcal/mol and A = $7.17 \times 10^{18}$ $min^{-1}$, are comparable with available literature values. The observed activation energies for first-order reactions of long-chain alkanes, for example, *n*-dodecane and *n*-hexadecane, are generally in the range of 60±5 kcal/mol. Ford (1986) reported that the kinetics for both liquid-phase and gas-phase pyrolysis of *n*-hexadecane are similar, and the activation energy for both is about 60 kcal/mol.

Figure 16 compares the experimental *n*-$C_{14}$ conversions (over the range from 0.02 to 0.70) to the values predicted from the kinetic parameters. The line corresponding to exact agreement is drawn as a diagonal. We can see that the predicted and experimental conversions are generally in good agreement; however, there exist more significant deviations at high conversions. Fabuss et al. (1964b) observed the phenomena of so-called self-acceleration and self-inhibition. It was reported that self-inhibition was generally observed in the decomposition of alkanes due to the formation of free radical inhibitors such as alkenes. On the other hand, self-acceleration can also occur. Recall that the system pressure displayed a monotonic increase with increasing residence time due to the continuous decomposition of *n*-$C_{14}$ to form smaller compounds and the secondary decomposition reactions of the primary products (Schobert et al., 1993b). It was reported that an increase in pressure can result in self-acceleration (Fabuss et al., 1964b). Our earlier study on the pyrolysis of *n*-$C_{14}$ at 450°C for 30 min also indicated that there was significant pressure dependence of n-$C_{14}$ conversion though a few fundamental questions remain to be answered (Schobert et al., 1993b). All these suggest that hydrocarbon pyrolysis at elevated pressure is very complex kinetically. A simple first-order relation as shown in Equation (1) might not suffice to represent the thermal decomposition over the whole conversion range; however, the simple first-order relation seemed to give good approximation for the thermal decomposition up to about 50% conversion.

2. Pyrolysis products. Figure 17 presents the ratio of *n*-alkane to the corresponding 1-alkene for $C_2$–$C_{13}$ products from the pyrolysis of *n*-tetradecane at 400°C. It can be seen that in

the early stage of the pyrolysis (up to 60 minutes, conversion 4.5%), except for $C_2$, the ratios were less than 1.0; in other words, the yield of an *n*-alkane in the $C_3$–$C_{13}$ range was lower than the corresponding 1-alkene. However, all the $C_2$–$C_{13}$ ratios increase progressively with time, and the $C_3$–$C_{11}$ *n*-alkanes begin to exceed the corresponding 1-alkenes at the conversion level of about 6–7% (approximated by interpolation). The products in the $C_{12}$ and $C_{13}$ groups are quite different from the others; the yields of *n*-$C_{12}$ and *n*-$C_{13}$ are very low compared with other *n*-alkane products. In similar fashion, Figure 18 presents the ratio of *n*-alkane to the corresponding 1-alkene for $C_2$–$C_{13}$ products from the pyrolysis of *n*-tetradecane at 425°C. Figure 18 also shows that, in the early stage of the pyrolysis, the yield of an *n*-alkane in the $C_5$–$C_{13}$ range was lower than the corresponding 1-alkene. Note that the $C_5$–$C_{11}$ *n*-alkanes begin to exceed the corresponding 1-alkenes at a higher conversion level of about 10% at 425°C than that at 400°C. It was found that at 450°C the $C_5$–$C_{11}$ *n*-alkanes did not exceed the corresponding 1-alkenes until at a much higher conversion level of greater than 20%. These observations imply that the lower temperature favors bimolecular reaction (H-abstraction) to form alkanes while higher temperature facilitates unimolecular reaction (β-scission) to form alkenes. This may be explained by the fact that the activation energy required for a bimolecular H-abstraction is lower than that for an unimolecular β-scission.

Figure 19 presents the *n*-$C_{14}$ selectivity at 400°C to *n*-alkanes ($C_1$–$C_{13}$) and 1-alkenes ($C_2$–$C_{13}$). The reactant selectivity was defined as the ratio of a product's molar yield to the conversion of reactant. There are several trends that can be seen from Figure 19. First, at low conversion (2.1 mol%), ethane and propylene are the most abundant alkane and alkene, respectively, and there are no particular alkanes in the liquid products ($C_5$ to $C_{11}$) that have high selectivity. Second, the yield of *n*-$C_{12}$ is very low compared with any of the $C_1$–$C_{11}$ alkanes, and the amounts of *n*-$C_{13}$ products are even smaller. The formation of *n*-tridecane becomes apparent only long after 60 min, but it is still much less than $C_1$–$C_{11}$ alkanes. Third, the selectivities of most of the 1-alkenes increase and reach a maximum after a certain period of time, then start to decrease. Fourth, it was shown in our earlier report that at 450°C there appeared a selectively enhanced formation of 1-hexene and 1-pentene from *n*-$C_{14}$ when the *n*-$C_{14}$ conversion reached 17 mol %. This kind of product distribution was also observed at lower temperatures (400°C), as shown in Figure 19. We have proposed a facile isomerization of primary radicals to account for such selectivity; *i.e.*, the preferential formation of 1-hexene and 1-pentene was attributed to a 1,5-shift and 1,4-shift, respectively, coiling-type isomerization of a primary radical generated from substrate molecule followed by a β-scission. Fifth, with further increase in residence time or conversion, the peak of carbon number distribution for alkane products shifts toward four. This is also true for the pyrolysis at 425°C as shown in Figure 20, which displays the *n*-$C_{14}$ selectivity at 425°C to *n*-alkanes ($C_1$–$C_{13}$)

and 1-alkenes ($C_2$–$C_{13}$). Note that for the pyrolysis at 450°C, ethane is always the most abundant alkane through the studied conversion range (from 4% to 99%) in spite of the fact that there appeared an slightly enhanced formation of *n*-$C_4$. The much enhanced formation of *n*-$C_4$ at 400°C and 425°C was attributed to the preferential formation of certain types of radicals from isomerization of primary radicals, followed by a β-scission. The following types of radicals are the sources of n-$C_4$: $C_{12}^6$ and $C_m^{m-5}$ , where $6 \leq m \leq 11$ and $C_{12}^6$ represents a 6-dodecyl radical.

3. Modelling results based on Fabuss-Smith-Satterfield mechanism. The Fabuss-Smith-Satterfield mechanism (1964a) was based on the modified Kossiakoff-Rice radical theory (1943). The modelling results based on Fabuss-Smith-Satterfield mechanism are discussed below. The two-step F-S-S decomposition can be represented by Equations (4)-(7):

| | | |
|---|---|---|
| $M \rightarrow R_1$ | radical formation | (4) |
| $R_1 \rightarrow R_1' \rightarrow Ol_1 + R_2$ | first-step isomerization and fission | (5) |
| $R_2 \rightarrow R_2' \rightarrow Ol_2 + R_3$ | second-step isomerization and fission | (6) |
| $R_3 + M \rightarrow R_3H + R_1$ | hydrogen transfer | (7) |

where M is the decomposing reactant,

$R_1$ is a first-generation free radical,

$R_1'$ is a free radical isomerized from $R_1$,

$Ol_1$ and $R_2$ are respectively a first-generation olefin and a second-generation free radical produced from scission of $R_1'$,

$R_2'$ is a free radical isomerized from $R_2$,

$Ol_2$ and $R_3$ are respectively a second-generation olefin and a third-generation free radical produced from scission of $R_2'$, and

$R_3H$ is an alkane converted from $R_3$ by hydrogen transfer.

The basic assumptions are 1) for radical formation, the activation energy difference is 2 kcal for removing a second and primary hydrogen and 4 kcal for removing a tertiary and primary hydrogen; 2) for radical isomerization, the activation energy difference for internal hydrogen transfer between a primary and a secondary position is 4 kcal, and the different secondary radicals are formed in equal amounts; 3) for scission reaction, the scission occurs at a β C-C bond from the radical position, and they are assumed to have equal probability when there are two β positions available except when one of the scission results in a methyl radical, whose probability is assumed to be one-fourth instead of one-half.

Figure 21 presents the predicted versus measured *n*-$C_{14}$ selectivity to *n*-alkanes and 1-alkenes at 400°C; both results from 2-step and 1-step (without second-step isomerization and fission, i.e., Equation 6) decomposition are shown for comparison. It can be seen that for 1-step decomposition mechanism, the experimental 1-alkene yields were in fair agreement with the prediction though the yields of propylene, 1-undecene, 1-dodecene, and 1-tridecene were overpredicted and 1-pentene and 1-hexene were underpredicted. The 1-step decomposition mechanism, however, did a poor job in predicting the experimental *n*-alkane yields; smaller alkanes were underpredicted, and on the other hand predicted decane and undecane yields were much higher than the experimental data. Figure 21 also shows that the *n*-alkanes were better predicted by the 2-step decomposition mechanism. However, the model tends to underpredict longer alkanes and exaggerate the 1-alkenes yields. In short, the overall product distribution including alkanes and alkenes could not be accurately predicted by either 1-step or 2-step F-S-S decomposition mechanism. The F-S-S mechanism tends to result in the significantly preferential formation of 1-alkenes, which is not true for our data especially when the conversion level is high. The failure of the F-S-S model in predicting our experimental data can be attributed to the following causes. First, the pressure in our pyrolysis experiments was high (>24 atmospheres). Higher pressure favors the bimolecular H-transfer, which leads to more alkanes, whereas lower pressure favors β-scission, that gives more alkenes. Second, too few initial primary radicals were produced based on their assumption. More alkanes can be produced from H-abstraction reactions between more abundant primary radicals and reactant. Third, the lack of alkene consumption step resulted in the monotonic increase of alkenes. Fourth, the omission of possible 1,5-shift and 1,4-shift isomerization led to unsuccessful prediction of 1-hexene and 1-pentene. We have taken these into consideration in our proposed reaction mechanisms, and the modelling work based on our proposed reaction mechanisms is in progress.

References

1. Fabuss, B. M., Smith, J. O., Satterfield, C. N. In Advances in Petroleum Chemistry and Refining; McKetta, John J., Ed.; 1964a, Volume 9, pp.156-201. Interscience Publishers: New York.
2 Fabuss, B. M.; Kafesjian, R.; Smith, J. O.; Satterfield, C. N. Ind. Eng. Chem. Proc. Des. Dev. 1964b, 3(3), 248-254.
3 Ford, T.J. Ind. Eng. Chem. Fundam., 1986, 25, 240-243.
4 Kossiakoff, A.; Rice, F.O. J. Am. Chem. Soc. 1943, 65, 590-595.
5 Lai, W.-C.; Song, C. Fuel , 1993, submitted.

6 Schobert, H. H.; Eser, C.; Song, C.; Hatcher, P. G.; Walsh, P. M.; Coleman, M. M. Advanced Thermally Stable Jet Fuels. Technical Progress Report (November 1992 - January 1993), March 1993a, The Pennsylvania State University.

7 Schobert, H. H.; Eser, C.; Song, C.; Hatcher, P. G.; Walsh, P. M.; Coleman, M. M. Advanced Thermally Stable Jet Fuels. Technical Progress Report (February 1993 - March 1993), July 1993b, The Pennsylvania State University.

8 Song, C.; Lai, W.-C..; Schobert, H. H. Ind. Eng. Chem. Res. 1993, submitted.

*3. Determination of Critical Properties of Jet Fuels (Contributed by Jian Yu and Semih Eser)*

Introduction

With the development of high speed aircraft, it is expected that the future jet fuel will be exposed to temperatures above the critical temperature due to increased thermal management requirements [1]. At higher temperatures, the fuel will decompose to form detrimental solid deposits. Previous studies show that the deposit formation from jet fuels exposed to high-temperature stress has a complex dependence on temperature [2]. In general the deposit formation rate rises with temperature, drops abruptly in a transition region (*e.g.* 350–425 °C), and then again increases with temperature. The sharp drop in deposit formation rates appears to reflect an effect of the transition from the liquid phase to the supercritical phase. Fluids near the critical point exhibit unusual physicochemical properties, such as large partial molar volume, local anisotropy, and high compressibility [3], which are expected to have a significant influence on the deposit formation in the transition region. The mechanisms of deposit formation from jet fuels under supercritical conditions are not known. In view of the fact that the future jet fuels will encounter supercritical conditions, there is a need to study specifically the effects of supercritical conditions on deposit formation from jet fuels. It is clear that the critical properties of the jet fuel must be determined to define sub- and supercritical regions before further studies are undertaken.

The are two ways of determining critical properties of substances: experimental measurement and estimation. Suitable experimental methods can produce reliable data, but they are rather laborious. Various experimental methods have been developed to determine critical properties of substances ranging from pure compounds to complex mixtures such as petroleum fractions [4–6]. Lately Teja and his coworkers have developed two novel methods for the determination of the critical properties of thermally unstable fluids, *i.e.*, a rapidly heating sealed tube method and a low residence time flow method [7]. The first can be used to measure the critical temperature and density while the second can be used to determine the critical

temperature and pressure. These two methods can produce the critical data with high precision for thermally unstable fluids due to low residence time of the sample in the apparatus before the critical point is reached. For critical temperature measurement of thermally unstable fluids the results from the flow method seem to be more accurate since the fluids are maintained at their critical temperatures for a short period (*ca.* 10–50 seconds) which minimizes thermal decomposition [8].

Compared to experimental methods, the determination of the critical properties of fluids using suitable prediction or correlation equations is quite convenient. For complex multicomponent mixtures such as jet fuels, there are no suitable predication equations. Instead a variety of correlation methods for estimating critical properties of petroleum fractions have been reported [4, 9–11].

In this work the critical temperatures of nine jet fuels were measured using a sealed tube method [6, 12] and the critical temperatures and pressures of the fuels were estimated using the methods recommended in [11]. The measured and estimated critical temperatures were compared and the suitability of the estimation method is discussed.

## Experimental

1. Samples. Six petroleum-derived jet fuels (JP-8P, JP-8P2, Jet A, Jet A-1, JP-7, and JPTS) and three coal-derived jet fuels (JP-8C, JP-8CA, and JP-8CB) were used in this work. The primary compositions of these fuels, except for JP-8CA and JP-8CB, can be found in [13]. The petroleum-derived jet fuels are composed mainly of long-chain alkanes while JP-8C consists mainly of monocyclic and bicyclic alkanes and some two-ring hydroaromatic compounds. The compositions of JP-8CA and JP-8CB are similar to those of JP-8C although JP-8CA has more low-boiling-point JP-8CB has more high-boiling-point components.

2.Critical Temperature Measurement. A sealed tube method was used to measure the critical temperatures of jet fuels [6, 12]. This method consists of sealing a certain amount of sample in a glass tube with a volume which is approximately equal to the volume of the sample at the critical temperature and then heating it rapidly in a furnace until the critical point is reached. The critical temperature is taken as the point at which the meniscus of the vapor and liquid disappears on heating or reappears on cooling through the critical point. If the filling density of the sample is equal to the critical density, then the meniscus will disappear or reappear at the half-volume of the tube. On the other hand, if the filling density is slightly larger than the critical density, then the disappearance, or reappearance, of the meniscus will occur slightly above the mid point of the tube, or vice versa. There is no need for the filling density to be exactly equal to the critical density for the measurement of the critical temperatures of the jet

fuels since the precision within 1–2 °F is enough for such complex mixtures as jet fuels consist of hundreds of compounds [13].

*Apparatus:* The apparatus used in this work was constructed by Lyons [14] as an adaptation of the Mogollon apparatus [15]. The details of this equipment can be found in [14]. The furnace consists of 22 nichrome heating elements arranged coaxially and strung longitudinally parallel to the cylindrical heating space. The heating space is 7 inches high and 2.25 inches in inner diameter. The heating assembly is enclosed in a 13 inch long, 3 inch outer diameter glass tube with quarter-inch wall thickness. The entire furnace is contained in an iron frame which is mounted on supports through an axis to permit rotation from horizontal to vertical position.

The temperature in heating space is regulated through a 120 V.A.C., 20 ampere variac. The temperature measurement is done using a model 115 JF Omega digital thermometer connected to an iron-constantan thermocouple probe.

The glass tube for holding the sample consists of two sections with an total length of 6.5 inches before loading. One section is the sample tube, which is made of non-precision quarter-inch outer diameter and 1 mm bore capillary tubing with a 5.25 inch length. The other section, which is fused to the sample tube, is used as the thermocouple well and is made of precision, quarter-inch outer diameter, 2 mm bore capillary tubing with a 1.25 inch length.

A nitrogen gas line is connected to the bottom of the furnace. This is used to provide an inert atmosphere which can prevent fire hazard in case of tube breakage, lower the oxidation of the nichrome heating elements, and increase the cooling rate of the interior heating space. However, the nitrogen gas was used only in the preheating period and in the interval between two measurements and was never used at temperature approaching the critical temperature since it caused severe temperature fluctuations even when a low nitrogen flow rate was used.

*Sample Loading:* As stated above, very accurate sample loading is not necessary for the purpose of this work. Therefore, the critical volumes of all fuels were assumed to be approximately equal to three times the volumes of liquid samples [12]. Usually the effective length of the sample tube after sealing was about 4.5 cm and corresponding sample loading length was around 1.5 cm. After suitable amount of sample was loaded using a glass syringe with a 0.5 mm outer diameter and 6 inch long needle, a band was marked around the tube at sealing position using a permanent marker. The loaded and marked sample tube was cooled in a beaker filled with ice for a few minutes. Noncondensible vapor was then removed with the help of a vacuum pump. The surface tension of the liquid in 1 mm bore capillary tubing was

large enough for keeping the liquid at the bottom of the tube. After removing vapor, the sample tube was sealed off using an oxy-acetylene torch with the marked band as a guide.

*Procedure:* Before a critical temperature measurement was started, the empty furnace was heated to the predetermined critical temperature by Roess equation [11], discussed later, using previously obtained voltage-temperature relationships as a guide. The sealed tube was fastened onto a loading/holding tube and was then inserted into the furnace and, simultaneously, a stopwatch was started to record the heating time. Then the voltage was quickly increased to the predetermined value for the required heating program. As the temperature approached the estimated critical temperature by approximately 60 °F the heating rate was reduced by decreasing voltage to the original voltage setting and the furnace was rotated continuously from horizontal to vertical position to mix the sample for maintaining a uniform temperature. When critical opalescence was observed the temperature and the time were recorded simultaneously. The temperature was then reduced by slightly decreasing the voltage. When the smoke-gray fog appeared followed by the reappearance of the meniscus, the temperature and the time were recorded as before. Procedure was repeated by increasing temperature above the critical point and decreasing it below the critical point while recording the temperature and time at the critical temperature. For reliable critical temperature readout it must be noted that the heating rate should be lower than 4 °F/min before a critical temperature was measured. Usually the first critical temperature was measured within 3–4 minutes and each measurement lasted about 20 minutes.

*Data Analysis:* From each measurement, a observed critical temperature vs. time curve can be obtained. For a thermally stable fluid, the observed critical temperature does not change with time within the experimental error. For a thermally unstable substance, however, the observed critical temperature may decrease or increase with time depending on whether decomposition or polymerization predominates. Usually decomposition reactions lead to lower critical temperature while polymerization reactions tend to increase the critical temperature. Therefore, for the thermally unstable substance, a suitable extrapolation must be used to determine the true critical temperature of the original substance. Several procedures have been suggested to determine the true critical temperature from the observed critical temperature vs. time data. Mogollon et al. [12] used a polynomial to fit the observed critical temperature vs. time curve and then extrapolated curve to zero time to get the true critical temperature. An obvious drawback of Mogollon procedure is that the rate of change in the observed critical temperature with time is the highest at room temperature which corresponds to zero time. This probably results in the overestimation of the true critical temperature. Lyons [14] modified the

Mogollon procedure and extrapolated the observed critical temperature vs. time curve to a time corresponding to a decomposition temperature at which the sample began to decompose. The decomposition temperature was determined by a decomposition test. In principle, the modified Mogollon procedure is more reasonable but additional experiments must be done. Anselme and Teja [16] developed another extrapolation procedure in which the critical temperature vs. time curve was extrapolated to the time at which the sample was stable. This time was determined by a stability test. The first two data points were used for linear extrapolation. The true critical temperature was then obtained by averaging the linearly extrapolated value and the first observed value.

For jet fuel samples it was found that the rate of change in the critical temperature with time was moderate. The observed critical temperatures for all nine jet fuels (eighteen samples) did not change with time in 8–10 minutes. Figure 22 shows the observed critical temperature vs. time curve for two jet fuels: JP-8P and JP-8C. Initial critical temperature vs. time relationships hint that the initial chemical changes of the jet fuel probably has a negligible effect on the critical temperature. Therefore, in this work the first observed critical temperature was taken as the true critical temperature.

Simulated Distillation by Gas Chromatography. To estimate the critical properties of jet fuels using methods recommended in [11], volumetric average boiling point (VABP) must be known. VABP can be calculated from ASTM D86 distillation data. In this work ASTM D86 distillation data were obtained from simulated distillation data by ASTM D2887, simulated distillation by gas chromatography, through the methods described in [11].

In the simulated distillation experiment, a calibration mixture of hydrocarbons of known boiling points covering the boiling point range of the sample is run in a gas chromatograph and a calibration curve is obtained by plotting boiling point vs. retention time. If the sample contains significant amounts of *n*-alkanes which can be identified on the chromatogram, these peaks can be used as internal boiling point calibrations. Since the jet fuel JP-8P contains identifiable *n*-alkanes from $C_8$–$C_{17}$, the peaks of these *n*-alkanes were used as internal boiling point calibration. A mixture of *n*-pentane, *n*-hexane, and *n*-heptane was run to cover the initial boiling points of jet fuels. Figure 23 shows the relationship between the retention times of n-paraffins and the corresponding atmospheric boiling points. After obtaining the calibration curve, various jet fuel samples were run in the gas chromatograph of the same operating conditions and the retention times at 0, 10, 30, 50, 70, 90, and 100 weight percent points were obtained. Table 3 gives retention times of jet fuels at different weight percent points. Simulated distillation temperatures at corresponding weight percent points were then determined using the calibration curve shown in Figure 23 by converting retention times to

the corresponding boiling points. Table 4 shows simulated distillation temperatures of jet fuels at different weight percent points.

Critical Property Calculations

The critical temperature $T_C$ and critical pressure $P_C$ of the jet fuels can be estimated by the methods described in [11].

$T_C$ can be calculated by the Roess equation:

$$T_C = 186.16 + 1.6667\Delta - 0.7127(10^{-3})\Delta^2 \quad (1)$$

$$\Delta = (\text{sp gr})(\text{VABP} + 100.0) \quad (2)$$

where Tc is the true critical temperature of the jet fuel, in degrees Fahrenheit; sp gr is specific gravity, 60°F/60°F and VABP refers to volumetric average boiling point, in degrees Fahrenheit, which is determined from ASTM D86 distillation temperatures at 10, 30, 50, 70, and 90 volume percent distilled points as described as follows:

$$\text{VABP} = (T_{10} + T_{30} + T_{50} + T_{70} + T_{90}) / 5 \quad (3)$$

In this work ASTM D86 distillation temperatures were obtained from ASTM D2887, simulated distillation (SD) by gas chromatography, through the following method as shown in [11].

$$\text{ASTM D86} = a(\text{SD})^b F^c \quad (4)$$

where a, b, and c are constants varying with percent distilled as given in Table 5; ASTM D86 is ASTM D86 distillation temperatures at 0, 10, 30, 50, 70, 90, and 100 volume percent points, in degrees Rankine; SD is simulated distillation temperatures at corresponding weight percent points, in degrees Rankine, and F is parameter given by Equation 5.

$$F = 0.009524(\text{SD } 10\%)^{0.05434}(\text{SD } 50\%)^{0.6147} \quad (5)$$

where SD 10% is SD temperature at 10% point, in degrees Rankine and SD 50% is SD temperature at 50% point, in degrees Rankine. Table 6 shows ASTM D86 temperatures of jet fuels at different volume percent points converted from simulated distillation temperatures at corresponding weight percent points.

$P_C$ can be determined by Figure 4D 2.1 given in [11]. In addition to VABP, API gravity and ASTM slope must be known beforehand to determine $P_C$, which are calculated from Equations 6 and 7:

$$\text{API gravity} = 141.5 / (\text{sp gr}) - 131.5 \quad (6)$$

$$\text{ASTM slope} = (T_{90} - T_{10}) / (90 - 10) \quad (7)$$

Table 7 lists related properties of jet fuels for determining critical properties and Table 8 gives calculated critical temperatures and pressures of nine jet fuels.

Results and Discussion

The apparatus was tested by measuring the critical temperatures of tetralin, *n*-decane, *n*-dodecane, and *n*-tetradecane, the reliable critical data of which are available from references [17, 18]. The purities of samples were 99+%. It was found that there were some temperature variations along the axial direction of the furnace. For the sample tube used in this work, the position of thermocouple probe was about 3.5 cm away from the position of vapor-liquid meniscus observed just before the critical point was reached. Tests showed that this resulted in about 5 °F temperature difference between these two positions with higher temperature at the position of thermocouple probe. Table 9 shows temperature distributions along axial direction of the furnace. Three tests gave similar temperature distribution tendency although different temperature ranges were used. Consequently the observed critical temperature was corrected by subtracting 5 °F from the thermometer readout. Table 10 shows the comparison between observed critical temperatures and literature values for four compounds stated above. The observed critical temperatures of tetralin and *n*-decane didn't change with time in 15 minutes and were taken as the true critical temperatures. For *n*-dodecane and *n*-tetradecane the observed critical temperatures changed with time and the true critical temperatures were determined using the method suggested by Anselme and Teja [16] except that the critical temperature vs. time curves were extrapolated to zero time for simplicity. Figure 24 shows the observed critical temperature vs. time curve for *n*-tetradecane. The results shown in Table 10 demonstrate that the largest deviation of the measured values from the reported data is 0.32%. This indicates that the apparatus and the extrapolation method are suitable for the purpose of this work.

Table 11 shows measured and estimated critical temperatures of nine jet fuels. The reproducibility of measurement is quite satisfactory. The selected value from two runs for each fuel is based on relative reliability, judging from vapor-liquid meniscus position. Usually sample loading did not deviate from critical loading for a significant degree. The disappearance or reappearance of meniscus at critical point occurred near the mid point of the tube. For two

samples of the same fuel, if the meniscus position of one sample was closer to the mid point of the tube when the critical temperature was measured, then this value was selected as the true critical temperature.

From Table 11 one can find that the deviations of the calculated critical temperatures from measured values are within 10 °F for petroleum-derived jet fuels except for JP-8P which shows a deviation of 18 °F. This agreement between the measured and estimated values is quite satisfactory for the complex mixtures such as jet fuels. For three coal-derived jet fuels, however, the calculated critical temperatures are 20–30 °F lower than the measured values. The larger deviations are probably related to the composition of coal-derived jet fuels. Roess equation was set up on the basis of the measured critical temperatures of many petroleum fractions which are composed mainly of paraffinic compounds. For coal-derived jet fuels, the main components are monocyclic and bicyclic alkanes and some hydroaromatic compounds. In these cases Roess equation may give larger deviations.

## Conclusions

The critical temperatures of petroleum- and coal-derived jet fuels were measured by a rapidly heating sealed tube method. The measured results are satisfactory and exhibit good reproducibility. In view of the fact that few experimental critical temperature data for jet fuels are found in literature, present results are significant.

The critical temperatures and pressures of jet fuels were estimated using the method recommended in [11]. While the Roess equation can give satisfactory critical temperature prediction for petroleum-derived jet fuels, the same equation is less reliable for coal-derived jet fuels.

## References


1. "Advanced Fuel Composition and Use," FY 93 New Initiative, Joint AFOSR and WPAFB Announcement, Summer 1991.
2. Taylor, W. F., Ind. Eng. Chem. Prod. Res. Develop., 13, 133 (1974).
3. Brennecke, J. F., In Supercritical Fluid Engineering Science: Fundamentals and Applications, Kiran, E. and Brennecke, J. F., Eds., ACS Symposium Series 514, ACS, Washington, DC, 1993, p. 201.
4. Roess, E. E., J. Inst. Petro. Tech., 22, 665 (1936).
5. Kobe, K. A. and Lynn, R. E., Chem. Rev., 52, 117 (1953).
6. Hicks, C. P. and Young, C. L., Chem. Rev., 75, 119 (1975).
7. Teja, A. S., Gude, M., and Rosenthal, D. J., Fluid Phase Equil., 52, 193 (1989).
8. Rosenthal, D. J. and Teja, A. S., AIChE J., 35, 1829 (1989).

9. Twu, C. H., Fluid Phase Equil., 16, 137 (1984).
10. Pedersen, K. S., Thomassen, P., and Fredenslund, A., Ind. Eng. Chem. Process Des. Dev., 23, 163 (1984).
11. Technical Data Book-Petroleum Refining, 4th ed., American Petroleum Institute, Division of Refining, Washington, DC, 1987.
12. Mogollon, E., Kay, W. B., and Teja, A. S., Ind. Eng. Chem. Fundam., 21, 173 (1982).
13. Lai, W-C, Song, C., Schobert, H. H., and Arumugam, R., ACS Div. Fuel Chem. Prepr., 37(4), 1671 (1992).
14. Lyons, R. L., M.S. Thesis, The Pennsylvania State University, University Park, Pennsylvania, 1985.
15. Mogollon, E., M.S. Thesis, The Ohio State University, Columbus, Ohio, 1969.
16. Anselme, M. and Teja, A. S., Fluid Phase Equil., 40, 127 (1988).
17. Daubert, T. E. and Danner, R. P., Physical and Thermodynamic Properties of Pure Chemicals, Design Institute for Physical Property Data, AIChE, 1992.
18. Teja, A. S., Lee, R. J., Rosenthal, D. J., and Anselme, M., Fluid Phase Equil., 56, 153 (1990).

## Task 2. Investigation of Incipient Deposition

*Growth and Deposition of Particles During Heating of Coal-Derived Aviation Gas Turbine Fuels (Contributed by Prashant C. Sanghani and Peter M. Walsh)*

In our previous report, measurements of deposit growth on the bottom of a tubing bomb reactor during stressing of mixtures of coal-derived jet fuel and tetradecane were compared with calculations based on the settling velocities of particles. At a stressing time of 8 hours the calculations and measurements were in satisfactory agreement, but at longer times the calculated rates were higher than observed. Recent work focussed on the refinement of the measurements, with emphasis on the initial stages of decomposition of the fuel and the onset of deposition.

Mixtures containing 81.5 wt% JP-8C and 18.5 wt% tetradecane were used for all of the experiments. The sizes and concentrations of suspended particles and the masses of deposits on the side walls and bottom of the reactor were measured after stressing the mixture for 2, 4, 6, 9, and 24 hours at 450°C under nitrogen. The top of the reactor, where some complicated deposition behavior had been observed in earlier experiments, was simplified by filling in the

cavity in the fitting which serves as the end cap. The top surface in the new reactor is perfectly flat, except for a 4 mm diameter hole through which the reactor is connected to a pressure gauge. The deposit formed at the top is now more uniform and easier to collect and weigh. The concentration of suspended particles, volume-based mean size of the particles, and growth of deposit on the bottom of the reactor are shown as functions of time in Figures 25, 26, and 27, respectively. Figure 27 shows a comparison of measurements of deposition on the bottom surface in the old and new reactor designs. Deposition on the bottom rises more rapidly in the new design, but the qualitative features of the time dependence are similar in both reactors, even out to 24 hours.

Assuming that particle size and concentration are quasi-steady, with particle formation from reactive species just balanced by the loss due to settling, deposition rates per unit area were found from the product of settling velocity and particle concentration. The deposit mass/area calculated by integrating these deposition rates is shown by the line drawn in Figure 27. Between 4 and 8 hours the calculated and observed rates (slopes) are in good agreement. At times less than 4 hours the growth of deposits is underestimated, and at times longer than 8 hours the rate is greatly overestimated. There are two difficulties: 1. more measurements are needed during the period when particles are growing to sizes which settle at significant rates (2 to 4 hours), and 2. the sizes of particles separated from the liquid products increases markedly after 12 hours (see Figure 26), causing an even more dramatic increase in the calculated settling velocity. The latter problem is thought to arise from the fact that some of the particles settling to the bottom at long times are not strongly attached to the deposit and are therefore included in the measurements of the size and mass of material suspended in the liquid at the end of each run. Because the most important practical problem is to delay the onset of deposit formation, rather than minimize the ultimate yield of deposits at high conversion (although the two may well be connected), we intend to concentrate in future work on the formation of particles at times shorter than about 8 hours, where the settling model seems to provide a satisfactory estimate of the deposition rates.

Measurements of deposit and particle formation from mixtures of coal-derived jet fuel and tetradecane covering the entire range of compositions from pure fuel to pure tetradecane, reported previously, showed that the yield of insoluble material was approximately proportional to the initial tetradecane concentration. This suggested that there may be a simple, direct relationship between tetradecane decomposition and the formation of active species responsible for particles and deposits. The decomposition of tetradecane was followed by GC-MS analysis of the liquid remaining after stressing of 18.5 wt% tetradecane mixtures for different times, with the results shown in Figure 28. The early stages of the decomposition are approximately pseudo-first-order, with a characteristic time of approximately 4 hours.

Comparison with the deposit growth measurements, in Figure 27, shows that the time constant for deposit growth is similar, suggesting that a relatively simple model consisting of a first-order decomposition step leading to reactive intermediates, followed by reaction of the intermedates to form particles, and settling of the particles, may be sufficiently detailed to describe deposit formation and provide a quantitative framework for calculation of rate coefficients for the rate-determining step. The rate equations for this mechanism will be developed and compared with the observations in the next period of work.

## Task 3. Characterization of Solid Gums, Sediments, and Carbonaceous Deposits.

### *1. Effects of Pretreatment with High Surface Area Activated Carbon PX-21 on Thermal Stressing of JPTS Jet Fuel (Contributed by Katia Gergova, Rathnamala Arumugam, and Semih Eser)*

Introduction

We have shown that the addition of high surface area activated carbon PX-21 to jet fuel stops the formation of carbonaceous solids on the reactor walls upon thermal stressing. The addition of PX-21 also inhibits thermal degradation of JPTS jet fuel even under severe conditions ( > 400°C). The performance of an additive depends on a number of factors, such as type of fuel, fuel composition, additive concentration, and temperature of stressing. It is well known that a fuel which shows the highest degree of instability also has the highest free radical concentration [1]. We assume that the presence of an activated carbon during thermal stressing terminates the free radical chain reactions by stabilizing the reactive species on active carbon surfaces [2]. The behavior of several carbons added to jet fuel during thermal stressing indicates that the surface area of an added carbon is an important parameter which determines its effectiveness [3]. Spiro [4] studied the catalytic effect of carbons on reactions in solution and reported that the surface area played an important role on carbon catalytic activity.

The amount of activated carbon PX-21 which needs to be added to JPTS jet fuel depends on the temperature of thermal stressing. We studied two relatively high temperatures and long times for thermal stressing, 425°C and 450°C for 5 h. There is no visible change in the color of the initial jet fuel mixed with 50 mg PX-21 after thermal stressing at 425°C for 5h. At a higher temperature (450°C for 5h) 100 mg PX-21 was sufficient to prevent carbon deposition on the reactor walls and enhanced the thermal stability of jet fuel [5]. It is known that thermal degradation of jet fuels is usually more severe or occurs at a much lower temperature if the fuel is saturated with air [6]. The addition of PX-21 delayed the degradation of JPTS more effectively in nitrogen

than in air. However, even at 450°C in air no carbonaceous deposit was observed on the reactor walls after stressing JPTS with PX-21..

Considering that high surface area activated carbons adsorb significant quantities of fuel and, depending on the surface properties of the carbon, selective adsorption of certain species in a given fuel may strongly affect its thermal stability. Especially if reactive compounds (*e.g.*, heteroatom species) can be removed by adsorption on a surface, the stability of fuels at high temperatures can be increased substantially. We performed a set of experiments to investigate the effects of contacting jet fuel with PX-21 in a batch system over a prolonged time period on its thermal stability during subsequent thermal stressing of the filtered fuel. In many cases, contacting the fuel with the activated carbon prior to thermal stressing appeared to be more effective than stressing it in the presence of the carbon.

Experimental

Two simultaneous sets of experiments were carried out on JPTS at 425°C for 5h in nitrogen atmosphere. One set of experiments was performed by stressing a mixture of 10 mL JPTS mixed with 50 mg PX-21. In the other set, 15 mL samples of JPTS were mixed separately with 50, 100, and 200 mg PX-21. The mixtures were stored in a nitrogen atmosphere for 3 days. Then the jet fuel samples were filtered to remove the activated carbon, and 10 mL samples of filtered JPTS was stressed alone at 425°C for 5h in a nitrogen atmosphere. The same experiments were conducted in an air atmosphere. For this series experiments the JPTS jet fuel was pretreated with 50 mg PX-21. Additionally, JPTS was treated for 3 days with 100, 150, 200, 300, and 500 mg PX-21 and was stressed at 450°C, for 5h in a nitrogen atmosphere.

GC analysis of the liquids treated with PX-21 for 3 days and stressed liquids after removing of PX-21 were conducted using Perkin Elmer 8500 with a fused silica capillary column. The quantitative analysis of the liquid products was performed based on calibration curves obtained from external standards. The compounds in the liquid products were identified by capillary gas chromatography-mass spectrometry (GC-MS) using a Hewlett Packard 5890 II GC coupled with HP 5971A mass selective detector.

The apparent surface area of activated carbon PX-21 was determined after pretreatment (*i.e.*, contacting) with JPTS jet fuel for 3 days and was compared with the apparent surface area of activated carbon PX-21 stressed with JPTS in nitrogen and air atmosphere at 425°C for 5h. Quantachrome automated adsorption apparatus Autosorb-1, model ASIT, was used to determine the apparent surface area by $N_2$ adsorption at 77 K. From the adsorption data, the BET surface areas were calculated [7].

The microstructures of original activated carbon PX-21, PX-21 after treatment with JPTS jet fuel for three days, and PX-21 after stressing with JPTS were examined by scanning electron microscope (SEM), ISI ABT, model SX-40A.

Results and Discussion

The results and discussion will be presented in three parts. First, we will present the visual observations and the product yield data on the samples of JPTS pretreated with different amounts of activated carbon PX-21 followed by thermal stressing of the treated fuel at 425°C and 450°C for 5h. Second, we will present and discuss the data on the analysis of liquid products obtained after stressing of pretreated jet fuel with PX-21 compared with the data on the neat JPTS, liquids from JPTS stressed alone, and those from JPTS stressed with PX-21. Third, we will present data on the microstructure and surface area of original PX-21 carbon, PX-21 treated with jet fuel, and PX-21 stressed with JPTS jet fuel.

1. Visual Observations and Product Yields. The pretreatment of JPTS jet fuel with PX-21 activated carbon was conducted on 15 mL fuel and 100, 150, 200, 300, and 500 mg carbon in $N_2$ atmosphere. Table 12 presents the results obtained after pretreatment of JPTS jet fuel as well as after stressing the treated fuel at 450°C for 5h in nitrogen.

The results in Table 12 show the effects of using different amounts of activated carbon used for pretreatment of jet fuel on the appearance of the liquid products from stressing. Slight change in color was observed in the stressing products obtained from JPTS pretreated with 100, 150 and 200 mg PX-21. Stressing the fuel pretreated with 100 mg of carbon at 450°C leads to a considerable amount deposit, approximately 80 mg. The deposit formed on the reactor walls decreases in quantity to almost one-half, 45 mg, when JPTS is pretreated with 200 mg PX-21 compared to 100 and 150 mg, but the results are still not satisfactory. The color of the resulting liquids is dark brown with high extents of degradation, as was also evident from the low liquid yields and relatively high pressures in the cold reactors after stressing. The most important observation is that no carbonaceous solid can be seen on the reactor walls after thermal stressing at 450°C for 5 h when the jet fuel is pretreated with 300 and 500 mg PX-21. The color of the resulting liquids is lighter compared to the color of the liquids obtained after stressing of JPTS pretreated with smaller quantities of PX-21. Also, the liquid yields are higher, and the pressures of the cold reactors are lower compared to the experiments done with smaller amount PX-21. It should be noted, however, that increasing the amount of activated carbon used for pretreatment of jet fuel leads to an increasing amount of liquid adsorbed on the activated carbon surface. There is little change in the adsorbed quantity of fuel during pretreatment and in the liquid yield after stressing when the amount of activated carbon used for pretreatment is increased from 300 to 500 mg.

We conducted stressing experiments also at 425°C for 5h in $N_2$. A 15 mL sample of JPTS jet fuel was treated with 50, 100, and 200 mg PX-21. The results from these experiments are summarized in Table 13. Additionally, we carried out stressing experiments at 425°C for 5h in air atmosphere using JPTS jet fuel pretreated with 50 mg PX-21, the results of which are also shown in Table 13. The data in Table 13 show that pretreatment of JPTS jet fuel with 50 mg PX-21 is sufficient to prevent the formation of carbonaceous solid on the reactor walls during stressing at 425°C and to slow down the degradation processes considerably. Practically, there is no difference between pretreatment with 50, 100, and 200 mg PX-21 when jet fuel is stressed at 425°C. The results obtained from stressing the pretreated JPTS at 425°C in air (last row in Table 13) suggest that the pretreated fuel is stable even in the presence of oxygen during thermal stressing.

We analyzed the liquid products obtained after pretreatment with PX-21 as well as after stressing of pretreated jet fuel in order to understand how the pretreatment of jet fuel with PX-21 affects the stressing process at high temperatures.

2. Analysis of liquid products obtained after pretreatment of JPTS with PX-21 and after stressing of pretreated jet fuel at 425°C for 5h in $N_2$. GC and GC/MS analyses were conducted on the liquid obtained after treatment of JPTS with PX-21 and the liquid obtained after stressing the pretreated jet fuel. Table 14 shows the weight percentages of selected compounds of the JPTS neat and JPTS after treatment with PX-21 as well as JPTS pretreated and stressed at 425°C for 5h in $N_2$. It appears that pretreatment with PX-21 selectively removes some *n*-alkanes from JPTS. Concentrations of some branched-chain alkanes and substituted cyclohexanes increased slightly upon pretreatment. Thermal stressing of the pretreated fuel produced only slight changes in its composition, including the formation of $C_5$–$C_7$ alkanes by cracking processes. There are slight decreases in the concentrations of long-chain alkanes $C_9$–$C_{11}$. Interestingly, the concentrations of reactive *n*-$C_{12}$–$C_{15}$ alkanes show slight increases in the liquid obtained after stressing of pretreated JPTS. Small changes are also noted in the concentrations of toluene and ethylbenzene.

Table 15 lists the weight percents of the same selected compounds as in Table 14 for JPTS neat and liquids obtained after stressing JPTS alone as well as pretreated JPTS and JPTS stressed with 50 mg PX-21. Additionally, Table 15 shows the concentration of naphthalenes in the analyzed liquids. The thermal stressing experiments were conducted at 425°C for 5 h in nitrogen. There are naphthalenes in JPTS neat and JPTS stressed after pretreatment with PX-21 in contrast to liquids obtained after thermal stressing of JPTS alone and with PX-21. The $C_3$–$C_5$ benzenes are not listed in Table 15 because there is no considerable difference in their concentrations between different samples. However, there are considerable differences in the concentrations of toluene and ethylbenzene. The concentration of toluene is very small in the original JPTS and JPTS stressed after pretreatment with PX-21 and increases significantly in the liquid obtained after stressing of JPTS alone and the liquid obtained after stressing of JPTS with PX-21. The same

trends can be seen for ethylbenzene. Another interesting observation is that the long-chain alkanes $C_{10}$-$C_{15}$ are in higher concentration in the liquid obtained after stressing of JPTS pretreated with PX-21 than those obtained after stressing JPTS with 50 mg PX-21. Both liquids, however, have higher concentrations of long-chain alkanes than JPTS stressed alone. The opposite trends can be clearly seen for the short-chain alkanes. They are in higher concentrations in the liquid obtained after stressing JPTS with PX-21 in comparison with the liquid pretreated with PX-21 before stressing.

The results from Table 14 and 15 suggest that pretreatment of JPTS jet fuel with 50 mg PX-21 before stressing is more effective in slowing the degradation reactions than heating JPTS mixed with 50 mg PX-21. Apparently, carbon pretreatment removes reactive compounds which accelerate thermal degradation reactions.

3. Microstructure and surface area of activated carbon PX-21 before and after interaction with JPTS jet fuel. Figure 29 shows the scanning electron micrographs of the original activated carbon PX-21 (a), PX-21 after treatment with JPTS (b), and PX-21 after thermal stressing with JPTS at 450°C for 5h (3). Different microstructures of the original PX-21 and PX-21 stressed with JPTS are observed. The very smooth and rounded structure in position (c) suggests that a thin layer of carbonaceous solid covered the activated carbon surface. The structures of untreated carbon (a) and PX-21 treated with JPTS but not stressed (b) are uneven and rougher than the structure of PX-21 stressed with JPTS (c). Some areas have a sponge-like surface which most probably reflects the microporous structure. It is impossible to observe the micropores with scanning electron microscope. However, there is no doubt that PX-21 has a very microporous structure because of the high BET $N_2$ surface area (2090 $m^2/g$). It is well known that the high surface area of activated carbon is mainly due to the micropores. Most probably micropores of activated carbon are filled with selected compounds from original jet fuel but the appearance of the PX-21 structure did not change. It should be noted that some small and round particles can be clearly seen on the surface of PX-21 after thermal stressing with JPTS (c). These particles show that the carbonaceous solid on the PX-21 surface is deposited not only in the form of thin layer, which makes the carbon surface round and smooth, but also in the form of discrete particles. These results are not unexpected. We have been examined the surface of other activated carbons stressed with jet fuel and they showed the same features [8].

Figure 30 shows the higher magnification micrographs of PX-21 treated with JPTS (a) and PX-21 stressed with JPTS at 450°C for 5h in nitrogen. Some cracks and big pores are detected on the rough carbon texture (a). Even at the higher magnification the surface of the stressed PX-21 is very smooth and no pores can be noticed (b).

The apparent surface area of activated carbon PX-21 was measured before and after treatment with JPTS and was compared with the surface area of PX-21 after stressing with JPTS at

450°C and 425°C in $N_2$ and air atmosphere, reported previously [5]. From Table 16 one can see that the surface area of treated activated carbon decreases considerably (from 2090 to 1150 $m^2/g$). Nevertheless, the surface area of treated PX-21 is higher than the surface area of stressed activated carbons. This layer does not allow nitrogen molecules to penetrate the porous structure of activated carbon.

## Conclusions

The results from stressing experiments of JPTS jet fuel pretreated with PX-21 show that pretreatment of 15 mL JPTS with 50 mg of PX-21 activated carbon delayed the degradation processes and prevented carbon deposition during thermal stressing at 425°C for 5h in nitrogen and air atmospheres. It appears that it is necessary to pretreat 15 mL JPTS with 300 mg of PX-21 activated carbon in order to delay degradation processes at 450°C. After pretreatment with 300 mg PX-21 no carbonaceous deposit was observed on the reactor walls when the fuel is stressed at 450°C for 5h. GC and GC/MS analysis of liquid products after stressing at 450°C were not conducted but it should be noted that the color of the liquids obtained was darker than the color of the liquids obtained after stressing of pretreated JPTS at 425°C.

The examination of the surface of PX-21 before and after stressing with JPTS shows that is covered with thin layer of carbonaceous deposit as well as small discrete particles when activated carbon is stressed with jet fuel. These results suggest that the carbonaceous solid formed during thermal stressing is deposited on the activated carbon surface. The activated carbon treated with JPTS shows the same microstructure as the original activated carbon. We can not observe the micropores with SEM but most likely small concentrations of jet fuel compounds are adsorbed on the microporous structure of activated carbon which decrease the carbon surface area.

## References

1. Batts, B. D., and Fathoni Zuhdan A. Energy and Fuels 5, 2, 1991.
2. Schobert, H. H., Eser, S., Song, C., Hatcher, P., Walsh, P., Coleman, M. Advanced Thermally Stable Jet Fuels, Technical Progress Report, November 1992-January 1993.
3. Schobert, H. H., Eser, S., Song, C., Hatcher, P., Walsh, P., Coleman, M. Advanced Thermally Stable Jet Fuels, Technical Progress Report, February 1993-March 1993.
4. Spiro, M. Catalysis Today 7, 167, 1990.
5 Schobert, H. H., Eser, S., Song, C., Hatcher, P., Walsh, P., Coleman, M. Advanced Thermally Stable Jet Fuels, Technical Progress Report, April 1993-June 1993.

6. Mayo, F. R. Free Radical Autoxidation of Hydrocarbons, Accounts of Chemical Research 7, 193, 1968.
7. Gregg, S., and Sing, K. S. W. Adsorption , Surface Area, and Porosity, Academic Press, London, 285, 1982.
8. Song, C., Eser, S., Schobert, H.H., Hatcher, P. Coleman, M., Walsh, P. Advanced Thermally Stable Coal-derived Jet Fuel, Technical Progress Report July 1991-November 1991.

## Task 4. Coal-based Fuel Stabilization Studies

### *1. Screening Potential Jet Fuel Stabilizers Using the Model Compound Dodecane*

*(Contributed by Emily M. Yoon, Michael M. Coleman, and John B. Stallman)*

Introduction

This study is a continuation of the work from the previous quarterly report [1]. Dodecane has been used as a model compound to quantitatively study the effect of hydrogen donor additives. In order to understand the hydrogen donor mechanism and compare the free radical scavenging capabilities of the additives, studies based on molar equivalents were performed. Additionally, new hydrogen donor additives have been evaluated.

Experimental

The reactants used in these studies were purchased from Aldrich Chemical Co. Dodecane(DoD), 1,2,3,4-tetrahydronaphthalene (I), 9,10-dihydrophenanthrene (II), 1,2,3,4-tetrahydroquinoline (III), benzyl alcohol (IV), benzaldehyde dimethyl acetal (V), phthalan (VI), and 1,2,3,4-tetrahydro-1-naphthol (VII) were used without further purification.

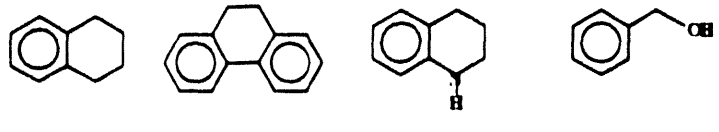

I II III IV

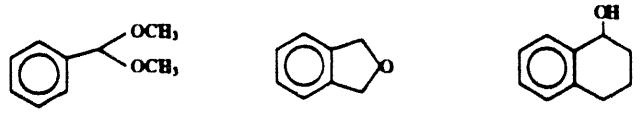

V VI VII

Thermal stressing was performed at 450°C in 25mL type 316 stainless steel microreactors under 0.69 MPa of UHP-grade $N_2$. The microreactor containing the sample was purged five times with UHP-grade $N_2$ at 7.0 MPa to minimize the presence of dissolved oxygen and finally pressurized with 0.69 MPa of $N_2$. It was then placed in a preheated sand bath at 450°C for 10-45 min, followed by quenching into cold water.

The liquid products were quantitatively analyzed using a Hewlett Packard GC with a FID detector. The column temperature was programmed from 40°C to 280°C at a heating rate 4°C/min after 5 min isothermal period at 40°C, followed by 10 min isothermal period at 280°C. The split mode of injection was used. The calculation of dodecane (DoD) conversion (mol%) was described in previous report [1]. A Hewlett Packard GC with mass detector was used for the qualitative analysis of reaction products.

Results and Discussion

Ten mol% (equivalent to about 5–6 volume%) of each additive was added based upon dodecane. Figures 41a, 41b, and 41c show the effects of the additives on the degradation of dodecane after thermally stressing for time periods of 10 to 45 min at 450°C. In the absence of additives, the amount of dodecane remaining after 10, 20, 30, 40 min is 96, 73, 65, 56 mol%, respectively. Except for compound V, which is not included in Figure 41, the presence of the additives significantly reduces the amount of dodecane conversion. Additive V was totally ineffective as a radical scavenger, most probably due to the cleavage of the side group at 450°C.

The figure illustrates that compounds II and III are superior to other additives. For example, after 45 min of reaction, about 92 mol% of the original dodecane remains. Compounds I, IV, and VII retard degradation and are in the middle range, *i.e.* about 70 mol% dodecane is left after 45 min of reaction. Compound VI is not a good radical scavenger although it did inhibit the dodecane decomposition somewhat. Although compound VII was expected to be superior to benzyl alcohol (IV), because of the additional tetralynic protons [2], the decomposition rate is similar to that of benzyl alcohol. This may be explained by the relatively rapid decomposition of compound VII to naphthalene as the mechanism is shown above. In essence, although compound VII gives up four protons in forming naphthalene, the conversion is too rapid and none of the additive VII exists in the mixture after 25 min as determined by GC/MS. Similarly, but for reasons not fully elucidated, compound VI in dodecane is decomposed after 35 min of reaction.

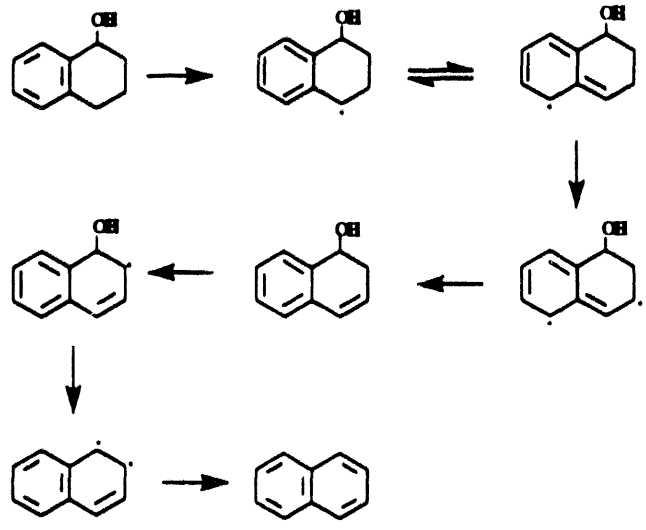

We believe the superior performance of the compound II is due to the fact that it has excellent thermal stability at 450°C in conjunction with the increase in resonance stabilization of the radical scavenger relative to benzyl alcohol. On the other hand, we are uncertain as why compound III is so effective. From GC/MS, we know that compound III is thermally stable at 450°C and that quinoline is formed as a reaction product. From the above results, we intend to propose and synthesize a new series of compounds, that will emphasize thermal stability and enhanced resonance stabilization of radicals at 450°C.

References

1. Yoon, E.M., Coleman, M.M., Song, C., Advanced Thermally Stable Jet Fuels, Technical Progress Report, February 1993-March 1993.
2. Stallman, J.B., Coleman, M.M., Advanced Thermally Stable Jet Fuels, Technical Progress Report, April 1993-June 1993.

## Task 4. Coal-based Fuel Stabilization Studies

### *1. Screening Potential Jet Fuel Stabilizers Using the Model Compound Dodecane*

*(Contributed by Emily M. Yoon, Michael M. Coleman, and John B. Stallman)*

Introduction

This study is a continuation of the work from the previous quarterly report [1]. Dodecane has been used as a model compound to quantitatively study the effect of hydrogen donor additives. In order to understand the hydrogen donor mechanism and compare the free

radical scavenging capabilities of the additives, studies based on molar equivalents were performed. Additionally, new hydrogen donor additives have been evaluated.

## Experimental

The reactants used in these studies were purchased from Aldrich Chemical Co. Dodecane(DoD), 1,2,3,4-tetrahydronaphthalene (I), 9,10-dihydrophenanthrene (II), 1,2,3,4-tetrahydroquinoline (III), benzyl alcohol (IV), benzaldehyde dimethyl acetal (V), phthalan (VI), and 1,2,3,4-tetrahydro-1-naphthol (VII) were used without further purification.

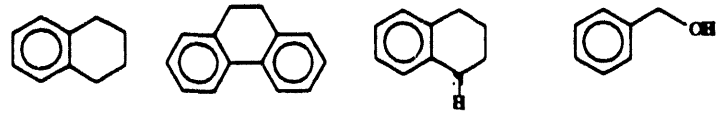

I II III IV

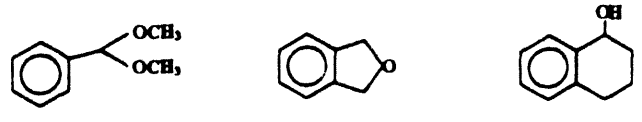

V VI VII

Thermal stressing was performed at 450°C in 25mL type 316 stainless steel microreactors under 0.69 MPa of UHP-grade $N_2$. The microreactor containing the sample was purged five times with UHP-grade $N_2$ at 7.0 MPa to minimize the presence of dissolved oxygen and finally pressurized with 0.69 MPa of $N_2$. It was then placed in a preheated sand bath at 450°C for 10-45 min, followed by quenching into cold water.

The liquid products were quantitatively analyzed using a Hewlett Packard GC with a FID detector. The column temperature was programmed from 40°C to 280°C at a heating rate 4°C/min after 5 min isothermal period at 40°C, followed by 10 min isothermal period at 280°C. The split mode of injection was used. The calculation of dodecane (DoD) conversion (mol%) was described in previous report [1]. A Hewlett Packard GC with mass detector was used for the qualitative analysis of reaction products.

## Results and Discussion

Ten mol% (equivalent to about 5–6 volume%) of each additive was added based upon dodecane. Figures 41a, 41b, and 41c show the effects of the additives on the degradation of

dodecane after thermally stressing for time periods of 10 to 45 min at 450°C. In the absence of additives, the amount of dodecane remaining after 10, 20, 30, 40 min is 96, 73, 65, 56 mol%, respectively. Except for compound V, which is not included in Figure 41, the presence of the additives significantly reduces the amount of dodecane conversion. Additive V was totally ineffective as a radical scavenger, most probably due to the cleavage of the side group at 450°C.

The figure illustrates that compounds II and III are superior to other additives. For example, after 45 min of reaction, about 92 mol% of the original dodecane remains. Compounds I, IV, and VII retard degradation and are in the middle range, *i.e.* about 70 mol% dodecane is left after 45 min of reaction. Compound VI is not a good radical scavenger although it did inhibit the dodecane decomposition somewhat.

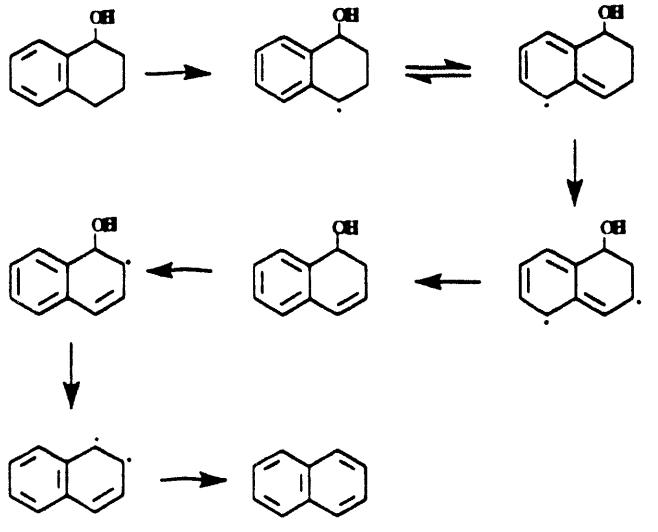

Although compound VII was expected to be superior to benzyl alcohol (IV), because of the additional tetralynic protons [2], the decomposition rate is similar to that of benzyl alcohol. This may be explained by the relatively rapid decomposition of compound VII to naphthalene as the mechanism is shown above. In essence, although compound VII gives up four protons in forming naphthalene, the conversion is too rapid and none of the additive VII exists in the mixture after 25 min as determined by GC/MS. Similarly, but for reasons not fully elucidated, compound VI in dodecane is decomposed after 35 min of reaction.

We believe the superior performance of the compound II is due to the fact that it has excellent thermal stability at 450°C in conjunction with the increase in resonance stabilization of the radical scavenger relative to benzyl alcohol. On the other hand, we are uncertain as why compound III is so effective. From GC/MS, we know that compound III is thermally stable at 450°C and that quinoline is formed as a reaction product. From the above results, we intend to

propose and synthesize a new series of compounds, that will emphasize thermal stability and enhanced resonance stabilization of radicals at 450°C.

References

1. Yoon, E.M., Coleman, M.M., Song, C., Advanced Thermally Stable Jet Fuels, Technical Progress Report, February 1993-March 1993.
2. Stallman, J.B., Coleman, M.M., Advanced Thermally Stable Jet Fuels, Technical Progress Report, April 1993-June 1993.

## Task 5. Exploratory Studies on the Direct Conversion of Coal to High Quality Jet Fuels.

*A Study of the Molecular Structure of Polycadinene from Dammar Resin: the First Phase of a Comparitive Study to Understand the Chemistry and Structure of Resin from Blind Canyon Coal Samples. (Contributed by Lei Hou, David J. Clifford, Daniel E. McKinney, Jacqueline M. Bortiatynski, and Patrick G.Hatcher)*

Introduction

Blind Canyon coals have been chosen as a potential liquefaction feedstock for jet fuels because they are rich in resinite. Resins and resinites (fossilized resins) supposedly contain readily cleaved cycloparaffinic structures which are desirable components in jet fuels due to their thermal stability. We have chosen to examine the structure of the resininite present in Blind Canyon coal in an effort to understand the chemisty of its conversion during liquefaction.

The general consensus regarding the structure of sesquiterpenoid resinites (*i.e.* the resinite from DECS16 coal) is that the maceral exists as two fractions. One fraction consists of a high molecular weight (HMW) polymer proposed to be that of polycadinene (PC) [1,2] and the second fraction is composed of low molecular weight compounds shown by gas chromatography/mass spectrometry (GC/MS) to be dimers and trimers of cadinene and functionalized triterpenoids [3-4]. In our previous report [5], we have demonstrated by spectroscopic techniques including pyrolysis-GC/MS and both liquid and solid-state nuclear magnetic resonance spectrometry (NMR) that the resinite maceral isolated from the Blind Canyon coal is a sesquiterpenoid resinite having a polycadinene-like backbone enveloped by a large proportion of volatile and occluded material. In that report, the resinite sample was not separated into its respective fractions so as to gain an overall understanding

of the chemical constituents contributing the maceral in bulk. We therefore isolated each fraction of the fossilized Blind Canyon resinite as well as the the fractions of a recent resin and subject them to analyses similar to those applied to the intact sample.

In this report, we will discuss the results of a series of experiments which were carried out in an effort to characterize a recent (extant), less-mature resin. By examining the structure of polycadinene from a young resin such as Dammar resin, we can compare its structral characteristics with those of the Blind Canyon resin. From this comparison, the chemical changes that accompany the coalification process can be identified, thus further aiding in the structural identification of the Blind Canyon coal's resinite maceral.

The Damar resin was chosen due to its availability in a relatively pure form. In addition, this particular resin is extremely soluble in $CDCl_3$. Solubility in $CDCl_3$ was an important consideration, since NMR was chosen as the primary structural tool for this study. As we have stated in previous reports, NMR is a powerful structural elucidation tool because it is nondestructive and is not restrictive in terms of examining high molecular weight or polar species, problems often incurred with GC/MS analysis of complex materials. NMR techniques, which include one- and two-dimensional NMR spectra, were used in this study to determine the consistency of the structure of the HMW, methanol-insoluble fraction of the Dammar resin with that of a pure, theoretical polycadinene polymer and to propose possible chemical alterations induced during coalification.

## Experimental

Sample Isolation. The resin selected for this study is a commercially available Dammar resin purchased from Aldrich Chemical Co. The Dammar resin was first dissolved in 50 mL of hexane then approximately 5 mL of methanol was added to precipitate the polymer as a white powder following the procedure described by van Aarrssen et. al. [2]. The powder was then separated by centrifugation and washed with methanol. The methanol was evaporated and replaced with approximately 0.6 mL of $CDCl_3$, a solvent suitable for NMR spectroscopy.

Elemental Analysis. Elemental analysis of the polycadinene isolated from Dammar resin was carried out using a Leco Model CHN-600 elemental analyzer.

NMR Analysis. The high-resolution liquid $^1H$ and $^{13}C$ NMR experiments were performed on a Bruker AMX-360 spectrometer equipped with a 5mm inverse-detected probe. The one-dimensional single pulse $^1H$ and $^{13}C$ experiments were carried out using a 30°flip angle. The pertinent parameters in the measurement of the $^1H$ NMR spectrum were as follows: a 2.8 μs (30°) pulse width, 2 s pulse delay, 15 ppm sweep width, 32 scans and

32K data points. The pertinent parameters for the $^{13}C$ spectra were as follows: 2.2 μs (30°) pulse width, 5 s pulse delay, 250 ppm sweep width, 32K FID data points. An inverse-gated decoupling pulse sequence was utilized to obtain quantitative $^{13}C$ NMR spectra. The $^{13}C$ distortionless polarization transfer (DEPT) experiments were carried out using 45° (3.3 μs), 90° (6.6 μs), and 135° (16.5 μs) $^{13}C$ read pulses, respectively. A solid-state $^{13}C$ CPMAS spectrum was obtained on a Chemagnetics M-100 NMR spectrometer. The pertinent parameters are found elsewhere [1].

A two-dimentional high resolution liquid experiment COSY (homonuclear correlation) with a 45° read pulse was performed on the polycadinene isolated from the Dammar resin using a standard Bruker experiment. The spectral resolution in the F1 dimension is 8.4 Hz/point while the resolution in the F2 dimension is 2.1 Hz/point. The total experimental time for the COSY45 was 14 hours.

Results and Discussion

Elemental analyses of the methanol insoluble fraction of the extant Dammar resin, the Dammar PC, as well as the previously reported data for the whole DECS16 sample are shown in Table 17. Included in Table 17 are the calculated oxygen and hydrogen weight percentages of a pure theoretical polycadinene polymer (structure shown in Figure 42), which has the monomeric formula $C_{15}H_{26}$, and the monomeric formula of the HMW Dammar PC polymer. It can be infered from this table that the polymeric constituent of the Dammar resin does not differ significantly from that of the whole Blind Canyon resinite. Also evident in this table are the considerable differences between the Dammar PC and a pure theoretical polymer composed solely of cadinene monomers. The Dammar PC elemental data suggest the presence of approximately one oxygen atom for every two cadinene monomers (assuming 15 carbons per monomer) and two less hydrogen atoms than the theoretical 26 in polycadinene.

$^{13}C$ NMR was used to identify the functional groups and substitution patterns of the carbons present in the Dammar PC. Figures 43–46 are high resolution $^{13}C$ NMR spectra of the Dammar PC in $CDCl_3$. Figure 43 is a broadband decoupled $^{13}C$ NMR spectrum, while Figures 44–46 are the $^{13}C$ distortionless polarization transfer (DEPT) spectra used to aid in assigning peaks to specific types of carbons. The aliphatic region of the broadband decoupled spectrum in Figure 43 (0 ppm to 60 ppm) is extremely complex and contains a number of sharp signals, far greater than what is anticipated for pure theoretical polycadinene, which might be expected to contain 13 aliphatic peaks. The olefinic region of the spectrum, 120 ppm to 140 ppm, is not as complex; however, but it is not consistent with structure of the theoretical polymer, where there are two olefinic

carbons, one a tertiary carbon and the other a quaternary carbon. The presence of four peaks in the spectrum of Dammar PC is indicative of greater complexity than expected for polycadinene, perhaps indicative of more than two types of olefinic carbons.

The spectra shown in Figures 44–46 are the three $^{13}C$ DEPT experiments (45°, 90°, and 135°). From these spectra and the spectrum in Figure 43, the functional group assignments have been made and are listed in Table 18. Chemical shift analysis of the spectrum in Figure 43 is used as a preliminary means of assigning carbon substitution, while the DEPT spectra provide a means of sorting or spectrally editing the signals. For example, the DEPT 45° spectrum contains peaks only for $CH_3$, $CH_2$, and CH carbons with the most intense signals emanating from the $CH_2$ carbons. The DEPT 90° spectrum contains only CH carbons, and the DEPT 135° spectrum contains positive signals from the CH and $CH_3$ carbons, but negative signals from the $CH_2$ carbons. Thus when the results from the three DEPT specta are compared, all the protonated carbons can be assigned. The non protonated carbons are assigned by difference from the $^{13}C$ broadband decoupled spectrum.

The solid-state CPMAS $^{13}C$ NMR spectrum for the HMW Dammar PC was obtained to ensure that all the carbons of the resin are observed and that some signals are not lost due to selective solubility or signal saturation in the liquid NMR experiments. Although the signals in Figure 47 are relatively broad as compared to those seen in Figure 43, a comparison of spectral regions can reveal major differences in structural characterstics. The only major differnce that is observed in the solid-state spectrum is a signal at 172 ppm seen in Figure 47 but not observed in the high-resolution spectrum. This particular signal has been tentatively assigned as a quaternary carboxyl carbon based entirely on its chemical shift, but further analysis is needed to confirm this assignment. Table 19 contains the complete functional group assignments for the $^{13}C$ CPMAS spectrum shown in in Figure 47.

To further aid in the structural elucidation of the Dammar HMW PC, two-dimensional (2D) NMR data were obtained. 2D-NMR is capable of correlating NMR spectral data in two dimensions, thus providing a means of confirming one-dimensional spectral assignments and, at the same time, providing structural information concerning molecular connectivity. A systematic approach to the 2D-NMR assignments was chosen. The experiment that yields the most valuable information is a heterocorrelated experiment (X-H COR) which provides proton-carbon connectivity, and because the data are yet to be finalized, they will appear in our next report. Before such an experiment can be performed the one dimensional $^{1}H$ and $^{13}C$ NMR spectra must be obtained and assigned.

The $^1H$ spectrum obtained for the Dammar PC is shown in Figure 48. An assignment of the $^1H$ NMR spectrum in Figure 48 is found in Table 20. The assignments of the spectrum shown in Figure 48 were confirmed by a 2D COSY experiment whose results are shown in Figure 49. Figures 50 and 51 contain expanded regions of the COSY spectrum. The $^1H$-$^1H$ COSY is used to assign $^1H$-$^1H$ connectivity through adjacent carbon bonds. For example, the $CH_2$ protons of one carbon are correlated with those protons found on any of the adjacent carbons. The coupled protons were correlated and the results are found in Table 21. With this phase of the spectral analysis complete, the critical 2D heterocorrelated experiment can now be carried out. The next report will contain the assignments of the final phase of the structural analysis of the polycadinene fraction of the Dammar resin.

Preliminary conclusions

The NMR data for Dammar PC, a purified sesquiterpenoid polymer thought to be the primary component of fossil resin, indicates that proposed structures (1) are not entirely correct. Quantitative estimation of the number of olefinic carbons indicates that approximately 1.5 olefins are present per $C_{15}$ substructure. This implies that one out of the $C_{15}$ sesquiterpenoid units is fully saturated. Also, the presence of 4 olefinic peaks of nearly equal intensity in the $^{13}C$ NMR spectrum is a clear indication that the internal double bonds are not located at the same positions in the two substructures containing olefinic carbons. The DEPT spectra give us clues that at least half of the olefins are quaternary. Thus, the information provided from the NMR studies indicates a new structural composition must be proposed for the polycadinene-like resin polymers from Dammar resin. Considering the fact that the Dammar PC is very similar to resinite from the Blind Canyon coal, we can expect to now have developed a working structural model for this component of a potential coal feedstock for liquefaction to jet fuels.

References

1. van Aarssen, B.G.K., Cox, H.C., Hoogendoorn, P., and de Leeuw, J.W. (1991) A cadinene biopolymer of fossil and extant dammar resins as a source for cadinanes and bicadinanes in crude oils from South East Asia. Geochem. Cosmochim. Acta. 54, 3021-3031.
2. Anderson, K.B., Winans, R.E., and Botto, R.E. (1992) The nature and fate of resins in the geosphere-II. Identification, classification and nomenclature of resinites. Org. Geochem. 18(6), 829-841.

3. Crelling, J.C., Pugmire, R.J., Meuzelaar, H.L.C., McClennen, W.H., Huai, H. and Daras, J. (1991) The chemical structure and petrology of resinite from the Hiawatha "B" coal seam. Energy & Fuels 5, 688-694.
4. Meuzelaar, H.L.C., Huai, H., Lo, R., and Dworzanski, J.P. (1991) Chemical composition and origin of fossil resins from Utah Wasatch Plateau coal. Fuel Proc. Technol. 28, 119-134.
5. Clifford, D.J., Hou, L., Bortiatynski, J.M. and Hatcher, P.G. (1993) Characterization of isolated resinite maceral. Technical Progress Report February 1993- March 1993, Prepared for the U.S. DOE under Contract No. DE-FG22-92PC92104, p. 46-50.

# APPENDIX 1

## TABLES

Table 1. Operating Parameters and Some Raw Data Collected from Each Run

| Sample number | Reaction temperature (°C) | Rate of NB ml/min | Rate of $N_2$ ml/min | Volume product gas ml | Duration gas collection min | Receiver before reaction, g | Receiver after reaction g | Liquid weight g | Duration liquid collection min |
|---|---|---|---|---|---|---|---|---|---|
| NB4 | 600 | 0.1269 | 7.16 | 153 | 9.75 | 33.434 | 32.456 | 0.978 | 10.25 |
| NB5 | 600 | 0.1269 | 26.60 | 320 | 9.58 | 35.080 | 34.134 | 0.946 | 10.00 |
| NB6 | 600 | 0.1269 | 50.00 | 523 | 9..00 | 33.304 | 32.472 | 0.832 | 10.25 |
| NB7 | 600 | 0.1269 | 100.14 | 1083 | 10.42 | 33.382 | 32.544 | 0.838 | 10.72 |
| NB8 | 600 | 0.3399 | 19.11 | 142 | 5.08 | 35.671 | 34.143 | 1.528 | 5.40 |
| NB9 | 600 | 0.1679 | 19.11 | 264 | 10.00 | 33.747 | 32.460 | 1.287 | 10.17 |
| NB10 | 600 | 0.0670 | 19.11 | 198 | 9.63 | 33.020 | 32.537 | 0.483 | 10.00 |
| NB11 | 600 | 0.03343 | 19.11 | 352 | 21.50 | 34.398 | 34.145 | 0.253 | 21.72 |
| NB12 | 600 | 0.1269 | 20.80 | 181 | 9.57 | 33.363 | 32.528 | 0.835 | 10.00 |
| NB13 | 600 | 0.2517 | 42.75 | 451 | 9.70 | 36.185 | 34.127 | 2.058 | 10.00 |
| NB14 | 600 | 0.0670 | 11.23 | 110 | 9.75 | 32.981 | 32.536 | 0.445 | 10.00 |
| NB15 | 600 | 0.0256 | 4.55 | 160 | 21.08 | 32.670 | 32.453 | 0.217 | 21.33 |
| NB16 | 600 | 0.6671 | 111.71 | 233 | 4.67 | 36.853 | 32.453 | 4.400 | 4.92 |
| NB18 | 500 | 0.1269 | 20.85 | 178 | 9.67 | 33.686 | 32.471 | 1.215 | 10.00 |
| NB19 | 500 | 0.6671 | 111.79 | 397 | 3.80 | 36.522 | 34.130 | 2.392 | 4.00 |
| NB20 | 500 | 0.03343 | 5.64 | 166 | 39.70 | 33.580 | 32.519 | 1.061 | 40.00 |
| NB21 | 500 | 0.0129 | 2.48 | 42.3 | 39.58 | 34.167 | 34.122 | 0.045 | 40.00 |
| NB22 | 500 | 0.2517 | 42.39 | 436 | 10.67 | 34.876 | 32.453 | 2.423 | 11.00 |
| NB24 | 550 | 0.2517 | 42.78 | 411 | 9.60 | 36.283 | 34.135 | 2.148 | 10.00 |
| NB25 | 550 | 0.1269 | 21.15 | 199 | 8.716 | 33.483 | 32.454 | 1.029 | 10.00 |
| NB26 | 550 | 0.0129 | 2.27 | 232 | 10.00 | 34.226 | 34.124 | 0.102 | 10.27 |
| NB27 | 550 | 0.0670 | 11.57 | 222 | 9.65 | 33.509 | 32.443 | 1.066 | 10.00 |
| NB28 | 550 | 0.6671 | 111.11 | 444 | 3.78 | 36.608 | 34.147 | 2.461 | 4.00 |

Table 3. Retention Times (min) of Jet Fuels at 0, 10, 30, 50, 70, 90, and 100 Weight Percent Points.

| | Weight percent distilled | | | | | | |
|---|---|---|---|---|---|---|---|
| Fuel | 0 | 10 | 30 | 50 | 70 | 90 | 100 |
| JP-8P | 3.3 | 7.0 | 11.3 | 15.7 | 20.2 | 27.1 | 38.7 |
| JP-8P2 | 3.3 | 9.4 | 15.4 | 19.2 | 23.3 | 28.9 | 38.5 |
| Jet A | 3.2 | 9.1 | 13.9 | 18.3 | 23.4 | 29.8 | 39.4 |
| Jet A-1 | 7.3 | 11.3 | 14.2 | 16.3 | 19.6 | 23.8 | 33.5 |
| JP-7 | 10.9 | 15.4 | 17.9 | 19.8 | 21.8 | 25.5 | 33.2 |
| JPTS | 3.2 | 8.2 | 11.8 | 14.8 | 18.3 | 23.7 | 30.4 |
| JP-8C | 2.2 | 3.2 | 7.4 | 15.9 | 22.3 | 30.4 | 42.0 |
| JP-8CA | 2.1 | 3.2 | 7.0 | 13.7 | 19.6 | 28.7 | 39.7 |
| JP-8CB | 2.2 | 3.8 | 9.6 | 16.4 | 23.8 | 31.2 | 41.3 |

Table 4. Simulated Distillation Temperatures (°F) of Jet Fuels at Different Weight Percent Points Obtained by ASTM D2887.

| | Weight percent distilled | | | | | | |
|---|---|---|---|---|---|---|---|
| Fuel | 0 | 10 | 30 | 50 | 70 | 90 | 100 |
| JP-8P | 242 | 304 | 345 | 385 | 424 | 489 | 595 |
| JP-8P2 | 242 | 326 | 382 | 416 | 453 | 506 | 593 |
| Jet A | 240 | 324 | 367 | 407 | 453 | 513 | 602 |
| Jet A-1 | 307 | 345 | 370 | 390 | 418 | 457 | 548 |
| JP-7 | 341 | 382 | 404 | 422 | 438 | 474 | 546 |
| JPTS | 240 | 316 | 350 | 376 | 407 | 456 | 520 |
| JP-8C | 195 | 240 | 308 | 386 | 443 | 520 | 625 |
| JP-8CA | 190 | 240 | 304 | 366 | 418 | 504 | 605 |
| JP-8CB | 195 | 257 | 328 | 390 | 457 | 527 | 620 |

Table 5. Constants in Equation 4.

| Percent distilled | a | b | c |
|---|---|---|---|
| 0 | 6.0154 | 0.7445 | 0.2879 |
| 10 | 4.2262 | 0.7944 | 0.2671 |
| 30 | 4.8882 | 0.7719 | 0.3450 |
| 50 | 24.1357 | 0.5425 | 0.7132 |
| 70 | 1.0835 | 0.9867 | 0.0486 |
| 90 | 1.0956 | 0.9834 | 0.0354 |
| 100 | 1.9073 | 0.9007 | 0.0625 |

Table 6. ASTM D86 Temperatures (°F) of Jet Fuels at Different Volume Percent Points Converted from Simulated Distillation Temperatures at corresponding Weight Percent Points.

| | Volume percent distilled | | | | | | |
|---|---|---|---|---|---|---|---|
| Fuel | 0 | 10 | 30 | 50 | 70 | 90 | 100 |
| JP-8P | 298 | 332 | 352 | 379 | 409 | 463 | 539 |
| JP-8P2 | 303 | 355 | 388 | 410 | 438 | 480 | 538 |
| Jet A | 300 | 352 | 374 | 401 | 438 | 486 | 546 |
| Jet A-1 | 351 | 367 | 373 | 386 | 403 | 433 | 499 |
| JP-7 | 384 | 403 | 407 | 419 | 424 | 450 | 499 |
| JPTS | 295 | 341 | 354 | 371 | 392 | 431 | 474 |
| JP-8C | 259 | 278 | 322 | 377 | 427 | 492 | 564 |
| JP-8CA | 252 | 275 | 315 | 358 | 402 | 477 | 546 |
| JP-8CB | 260 | 293 | 339 | 382 | 441 | 499 | 560 |

Table 7. Related Properties of Jet Fuels for Determination of Critical Properties.

| Fuel | Specific gravity | VABP, F | API gravity | ASTM slope, F/% |
|---|---|---|---|---|
| JP-8P | 0.790 | 387 | 47.6 | 1.64 |
| JP-8P2 | 0.798 | 414 | 45.8 | 1.56 |
| Jet A | 0.803 | 410 | 44.7 | 1.68 |
| Jet A-1 | 0.799 | 392 | 45.6 | 0.83 |
| JP-7 | 0.790 | 421 | 47.6 | 0.59 |
| JPTS | 0.782 | 378 | 49.4 | 1.13 |
| JP-8C | 0.834 | 379 | 38.2 | 2.68 |
| JP-8CA | 0.834 | 365 | 38.2 | 2.53 |
| JP-8CB | 0.839 | 391 | 37.2 | 2.58 |

Table 8. Estimated Critical Temperatures and Pressures of Jet Fuels.

| Fuel | Critical Temperature Tc/F | Critical Pressure Pc/psia |
|---|---|---|
| JP-8P | 722 | 355 |
| JP-8P2 | 750 | 330 |
| Jet A | 749 | 345 |
| Jet A-1 | 731 | 340 |
| JP-7 | 751 | 305 |
| JPTS | 710 | 340 |
| JP-8C | 738 | 475 |
| JP-8CA | 725 | 490 |
| JP-8CB | 752 | 460 |

Table 9. Temperature Distributions along Axial Direction of the Furnace

| Distance from thermocouple probe/cm | Temperature/F Test 1 | Test 2 | Test 3 |
|---|---|---|---|
| 0 | 776 | 753 | 725 |
| 1 | 775 | 752 | 724 |
| 2 | 773 | 750 | 722 |
| 3 | 771 | 748 | 721 |
| 4 | 770 | 747 | 720 |

Table 10. Critical Temperature Comparison of Four Compounds.

| Compound | Measured Tc/F Sample 1 | Sample 2 | Literature value Tc/F |
|---|---|---|---|
| Tetralin | 837 | 837 | 836.6 [17] |
| n-Decane | 654 | 654 | 652.2 [18] |
| n-Dodecane | 726 | 726 | 725.5 [18] |
| n-Tetradecane | 784 | 784 | 786.5 [18] |

Table 11. Measured and Estimated Critical Temperatures of Jet Fuels.

| Fuel | Measured Tc/F Sample 1 | Sample 2 | Selected | Estimated Tc/F |
|---|---|---|---|---|
| JP-8P | 741 | 740 | 740 | 722 |
| JP-8P2 | 757 | 757 | 757 | 750 |
| Jet A | 752 | 751 | 752 | 749 |
| Jet A-1 | 732 | 732 | 732 | 731 |
| JP-7 | 761 | 761 | 761 | 751 |
| JPTS | 719 | 719 | 719 | 710 |
| JP-8C | 762 | 761 | 761 | 738 |
| JP-8CA | 754 | 753 | 753 | 725 |
| JP-8CB | 773 | 774 | 773 | 752 |

Table 12. Yield of Liquids and Solid Products before and after Stressing Experiments at 450°C for 5h in $N_2$ on JPTS Jet Fuel Pretreated with PX-21 and Pressure Buildup.

| Process conditions | Liquid yield before stressing, ml | Increase of weight of carbon, % | Liquid color after stressing | Solid on reactor walls, mg | Liquid yield after stressing, ml | Gas pressure (cold), psi |
|---|---|---|---|---|---|---|
| JPTS treated with 100 mg PX-21 | 13.7 | 68 | dark brown | 86 | 3.1 | 550 |
| JPTS treated with 150 mg PX-21 | 13.5 | 70 | dark brown | 80 | 3.2 | 500 |
| JPTS treated with 200 mg PX-21 | 12.5 | 76 | brown | 45 | 3.6 | 500 |
| JPTS treated with 300 mg PX-21 | 12.1 | 81 | reddish | - | 4.5 | 200 |
| JPTS treated with 500 mg PX-21 | 11.5 | 86 | very light brown | - | 4.8 | 100 |

Table 13. Yields of Liquids and Solid Products before and after Stressing Experiments at 425°C for 5h in $N_2$ and Air on JPTS Jet Fuel Pretreated with PX-21 and Pressure Buildup.

| Process conditions | Liquid yield before stressing, ml | Increase of weight of carbon, % | Liquid color after stressing | Solid on reactor walls, mg | Liquid yield after stressing, ml | Gas pressure (cold), psi |
|---|---|---|---|---|---|---|
| JPTS treated with 50 mg PX-21 in $N_2$ | 13.8 | 70 | yellowish | - | 6.5 | 200 |
| JPTS treated with 100 mg PX-21 in $N_2$ | 13.6 | 66 | yellowish | - | 6.8 | 200 |
| JPTS treated with 200 mg PX-21 in $N_2$ | 12.7 | 78 | yellowish | - | 6.9 | 100 |
| JPTS treated with 50 mg PX-21 in air | 13.6 | 68 | light yellow | - | 6.4 | 250 |

Table 14. Weight Percents of Selected Compounds of JPTS Neat and the Liquids Obtained from JPTS Treated with PX-21 and JPTS Stressed after Treatment with JPTS at 425°C, 5h in $N_2$.

| Compounds identified | JPTS neat, wt% | JPTS treated with PX-21, wt% | JPTS stressed after treatment with PX-21, wt% |
|---|---|---|---|
| n Pentane | - | - | 0.43 |
| n-Hexane | - | - | 0.47 |
| n-Heptane | 0.03 | 0.03 | 0.16 |
| n-Octane+$C_2$ cyclohexane | 0.45 | 0.42 | 0.43 |
| n-Nonane+$C_2$ cyclohexane | 1.62 | 1.53 | 1.27 |
| n-Decane | 4.83 | 4.70 | 4.31 |
| n-Undecane | 5.90 | 5.96 | 5.84 |
| n-Dodecane | 3.33 | 3.27 | 3.48 |
| n-Tridecane | 2.14 | 2.05 | 2.31 |
| n-Tetradecane | 1.72 | 1.70 | 1.87 |
| n-Pentadecane | 0.55 | 0.54 | 0.60 |
| Toluene | 0.04 | 0.02 | 0.13 |
| Ethyl benzene | 0.05 | 0.08 | 0.01 |

Table 15. Weight Percents of Selected Compounds of JPTS (Neat) and Liquids Obtained after Stressing of JPTS at 425°C, 5h, in $N_2$ with and without PX-21.

| Compounds identified | JPTS neat, wt% | JPTS stressed after treatment with PX-21, wt% | JPTS stressed alone, wt% | JPTS stressed with 50 mg PX-21, wt % |
|---|---|---|---|---|
| n Pentane | - | 0.43 | coeluted with pentene-0.83 | coeluted with pentene-1.15 |
| n-Hexane | - | 0.47 | 0.70 | 1.29 |
| n-Heptane | 0.03 | 0.16 | 0.79 | 0.87 |
| n-Octane+ $C_2$ cyclohexane | 0.45 | 0.43 | 1.09 | 1.11 |
| n-Nonane+ $C_2$ cyclohexane | 1.62 | 1.27 | n-Nonane alone-1.76 | n-Nonane alone-1.87 |
| n-Decane | 4.83 | 4.31 | 3.43 | 3.82 |
| n-Undecane | 5.90 | 5.84 | 3.88 | 4.29 |
| n-Dodecane | 3.33 | 3.48 | 2.05 | 2.38 |
| n-Tridecane | 2.14 | 2.31 | 1.37 | 1.68 |
| n-Tetradecane | 1.72 | 1.87 | coeluted with naphthalene-0.95 | coeluted with naphthalene-1.31 |
| n-Pentadecane | 0.55 | 0.60 | 0.31 | 0.40 |
| Toluene | 0.04 | 0.13 | 0.54 | 0.53 |
| Ethyl benzene | 0.05 | 0.01 | 0.20 | 0.37 |
| 2 Methyl naphthalene | - | - | 0.07 | 0.16 |
| 1 Metrhyl naphthalene | - | - | 0.04 | 0.11 |
| Dimethyl naphthalene | - | - | 0.02 | 0.07 |

Table 16. Surface Area of PX-21 Activated Carbon before and after Different Treatments.

| Treatment conditions | BET $N_2$ surface area, $m^2/g$ |
|---|---|
| Untreated PX-21 | 2090 |
| PX-21 treated 3 days with JPTS jet fuel | 1150 |
| PX-21 stressed with JPTS at 425°C, 5h, $N_2$ | 785 |
| PX-21 stressed with JPTS at 425°C, 5h, air | 630 |
| PX-21 stressed with JPTS at 450°C, 5h, $N_2$ | 550 |
| PX-21 stressed with JPTS at 450°C, 5h, air | 320 |

Table 17. Ultimate analysis (DMMF) of the HMW fraction from a Dammar resin, the resinite from a Blind Canyon DECS-16 coal sample, and pure polycadinene.

| Sample | % C | % H | % O | Monomeric Formula |
|---|---|---|---|---|
| | | | | |
| Polycadinene (Dammar PC) | 84.2 | 11 | 4.8 | $C_{15}H_{24}O_{0.65}$ |
| Whole resinite (DECS16) | 86.2 | 10.4 | 3.4 | |
| Polycadinene (theoretical polymer) | 87.3 | 12.7 | 0 | $C_{15}H_{26}$ |

*Obtained by difference.

Table 18. The assignment of the high resolution liquid $^{13}C$ NMR spectra obtained for the the Dammar PC.

| Carbon Substitution | CH (Methine) | $CH_2$ (Methylene) | $CH_3$ (Methyl) | C (Quaternary) |
|---|---|---|---|---|
| | | | | |
| Chemical shifts* (ppm) | | | | |
| | 15.23 | 19.41 | 17.51 | 131.5 |
| | 21.26 | 21.76 | | 135.4 |
| | 26.43 | 24.29 | | 147.4 |
| | 32.59 | 26.84 | | 218.14 |
| | 36.25 | 28.58 | | |
| | 37.37 | 29.35 | | |
| | 38.07 | 30.85 | | |
| | 41.86 | 32.98 | | |
| | 43.86 | 33.43 | | |
| | 46.54 | 35.49 | | |
| | 50.04 | 39.41 | | |
| | 54.68 | 41.32 | | |
| | 55.23 | 49.01 | | |
| | 76.40 | 106.31 | | |
| | 79.42 | 112.18 | | |
| | 123.3 | | | |
| | 125.9 | | | |

*Chemical shifts relative to TMS.

Table 19. Assignment of the $^{13}C$ CPMAS NMR spectrum of the Dammar PC.

| Carbon type | CH (Methine) | $CH_2$ (Methylene) | $CH_3$ (Methyl) | C (Quaternary) |
|---|---|---|---|---|
| | | | | |
| Chemical shifts* (ppm) | | | | |
| | 14.08 | 24.24 | 19.57 | 133.3 |
| | 45.12 | 34.68 | | 147.0 |
| | 71.77 | | | 172.0 |
| | 76.20 | | | 215.0 |
| | 124.8 | | | |

*Chemical shifts relative to TMS.

Table 20 The functional group assignment of the $^1H$ NMR spectrum of the Dammar PC.

| Functional Group | Chemical Shifts* (ppm) |
|---|---|
| Carbonyl | 9.41 |
| | 9.33 |
| Internal Olefin | 5.51 |
| | 5.48 |
| | 5.13 |
| External Olefin | 4.85 |
| | 4.75 |
| | 4.72 |
| | 4.68 |
| CH (methine) | 3.48 |
| CH(cyclic) | 2.47 |
| CH(alpha) | 2.14 |
| $CH_2$(cyclic) | 1.74 |
| $CH_2$(gamma) | 1.63 |
| | 1.59 |
| | 1.26 |
| $CH_3$(terminal) | 1.13 |
| | 1.10 |
| | 1.07 |
| | 1.05 |
| | 1.01 |
| | 0.98 |
| | 0.96 |
| | 0.92 |
| | 0.90 |
| | 0.86 |
| | 0.84 |
| | 0.80 |
| | 0.79 |

*Chemical shifts relative to TMS.

Table 21. The assignment of the $^{1}H$-$^{1}H$ COSY 45 spectrum obtained for the Dammar PC.

| Functional Group | Chemical Shift Region (ppm) | Correlated Chemical Shifts (ppm) | Correlated Functional Group |
|---|---|---|---|
| $CH_3$ (terminal) | 0.79 -1.1 | 2.0<br>2.2 -2.4 | CH (Alpha)<br>CH (cyclic) |
| CH (isopropyl) | 2.0 | 2.2 | CH (cyclic) |
| $CH_2$ (cyclic) | 1.2 - 1.6 | 1.7 - 1.8 | $CH_2$ (cyclic) |
| $CH_2$ (cyclic) | 1.8 | 2.5 | CH (cyclic) |
| CH (cyclic) | 2.0 -2.6 | 1.5 - 2.0 | $CH_2$ (cyclic) |
| CH (bridge) | 3.3 | 1.6 | $CH_2$ (cyclic) |
| Olefin (external) | 4.7<br><br>4.8 | 4.8<br>2.3<br>4.7<br>2.3 | Olefin (external)<br>CH (cyclic)<br>Olefin (external)<br>CH (cyclic) |
| Olefin (internal) | 5.2<br><br>5.5 | 2.1<br>1.6 | CH (cyclic)<br>$CH_2$ (cyclic) |
| Carbonyl | 9.4 | | |

# APPENDIX 2

## FIGURES

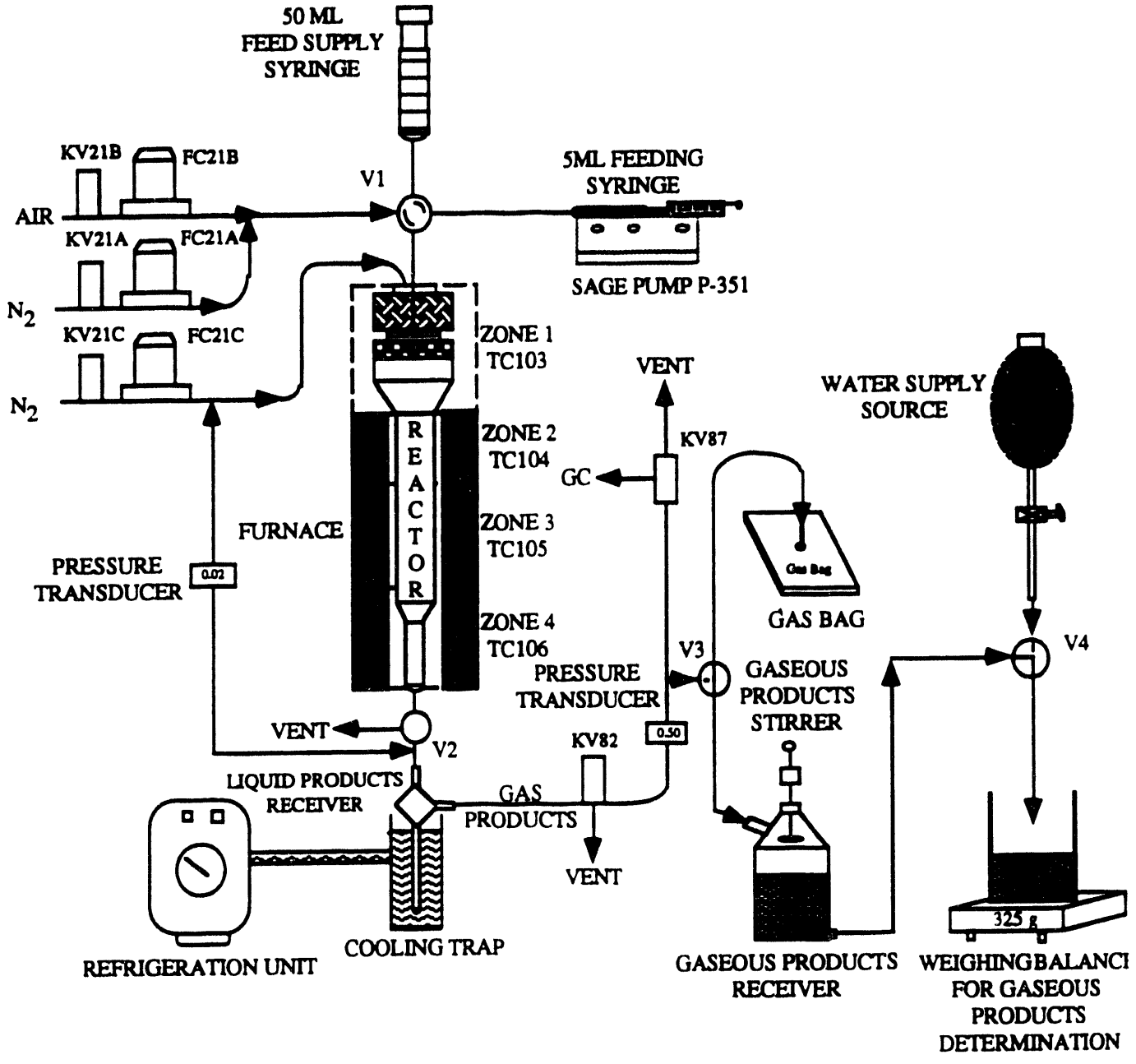


Figure 1. Schematic Diagram of the Xytel Equipment.

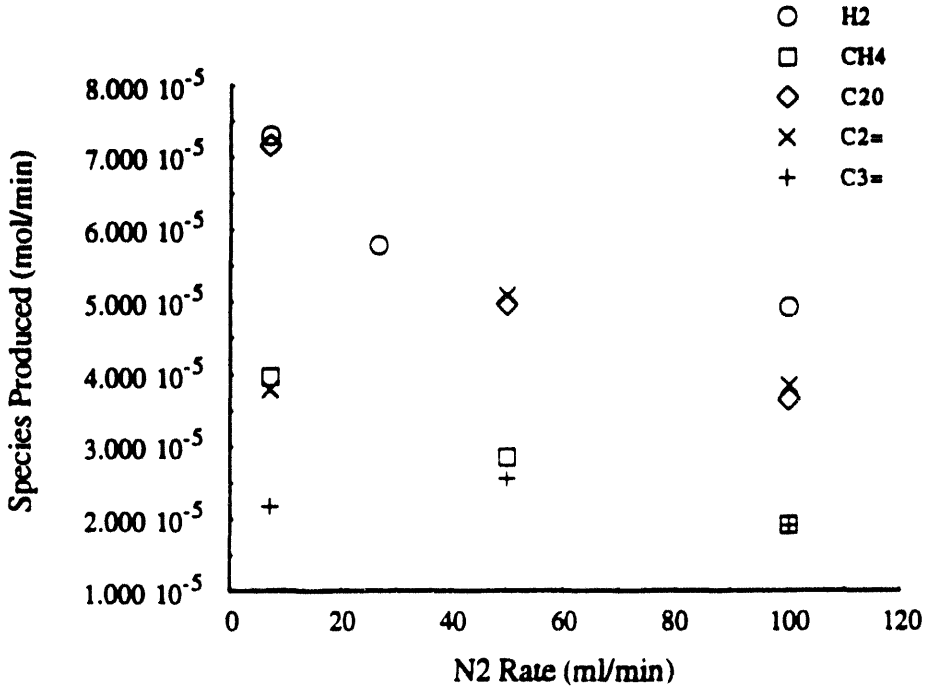


Figure 2. Variations of Some Gaseous Products with $N_2$ Flow Rate at 600°C.

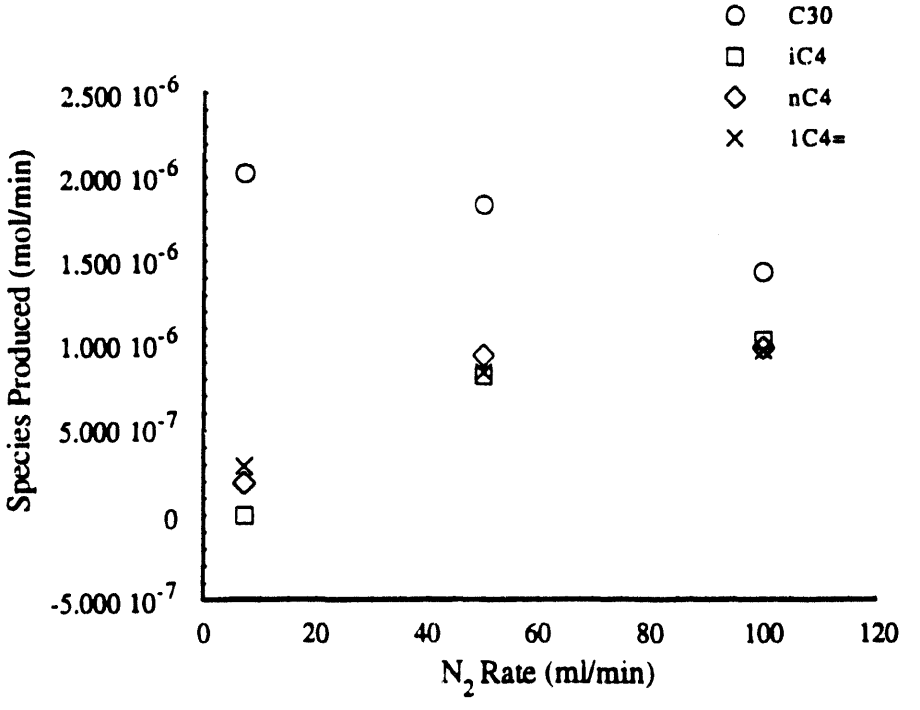


Figure 3. Variations of Some Gaseous Products with $N_2$ Flow Rate at 600°C.

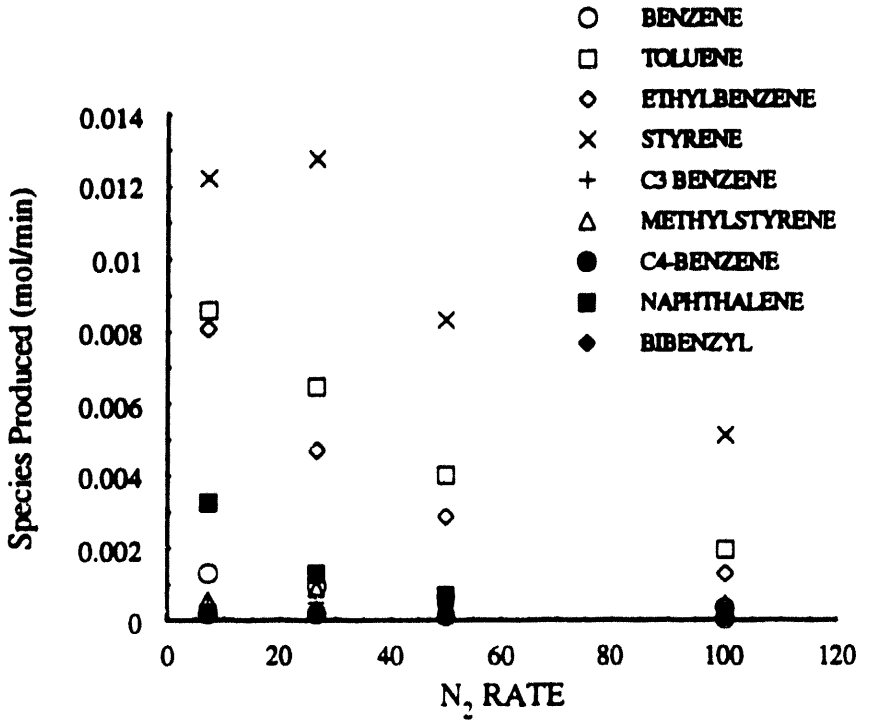


Figure 4. Variations of Some Major Liquid Products with $N_2$ Flow Rate at 600°C.

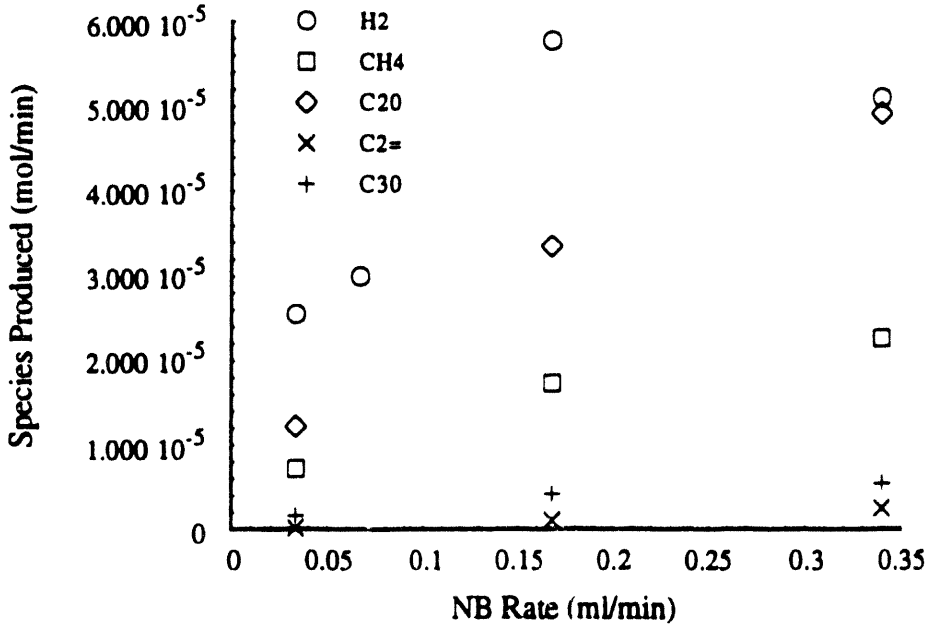


Figure 5. Variations of Some Gaseous Products with n-Butylbenzene Flow Rate at 600°C.

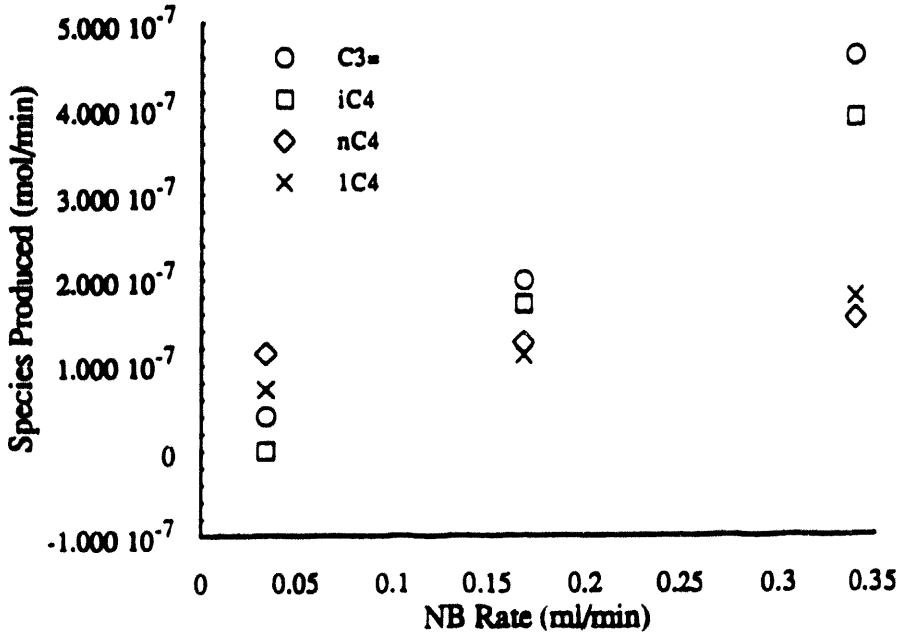


Figure 6. Variations of Some Gaseous Products with n-Butylbenzene Flow Rate at 600°C.

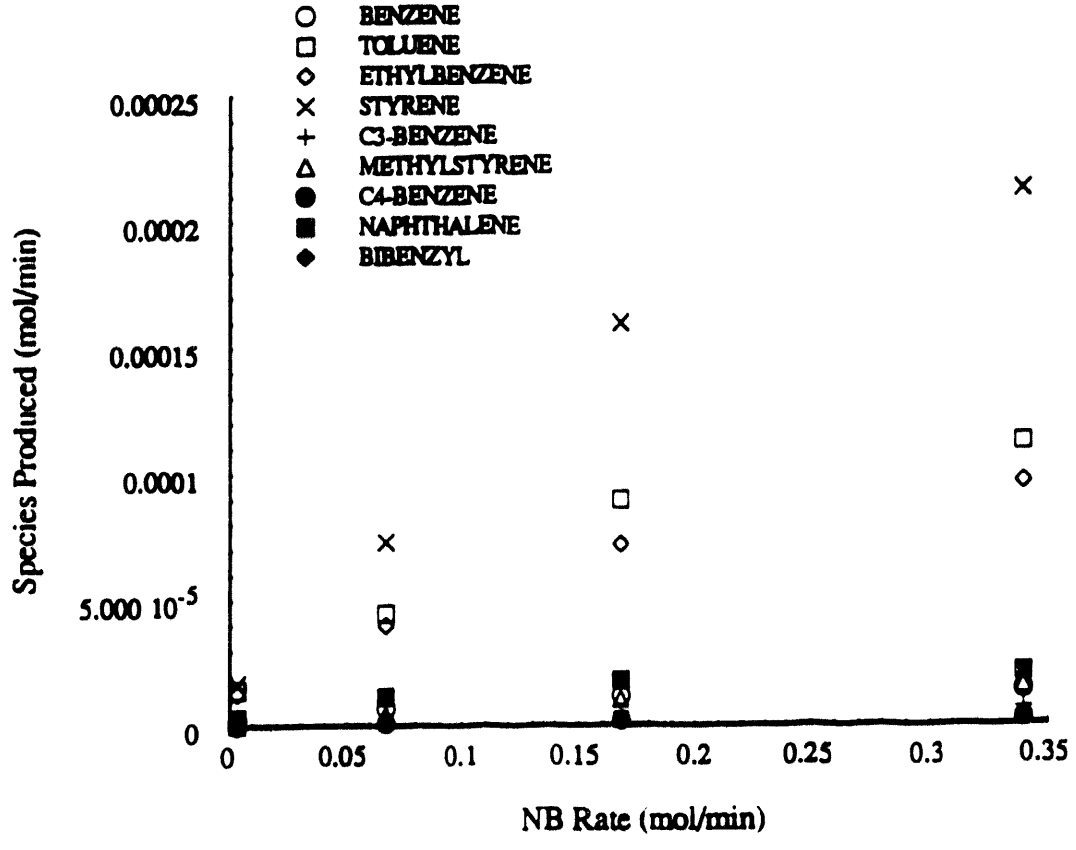


Figure 7. Variations of Some Major Liquid Products with n-Butylbenzene Flow Rate at 600°C.

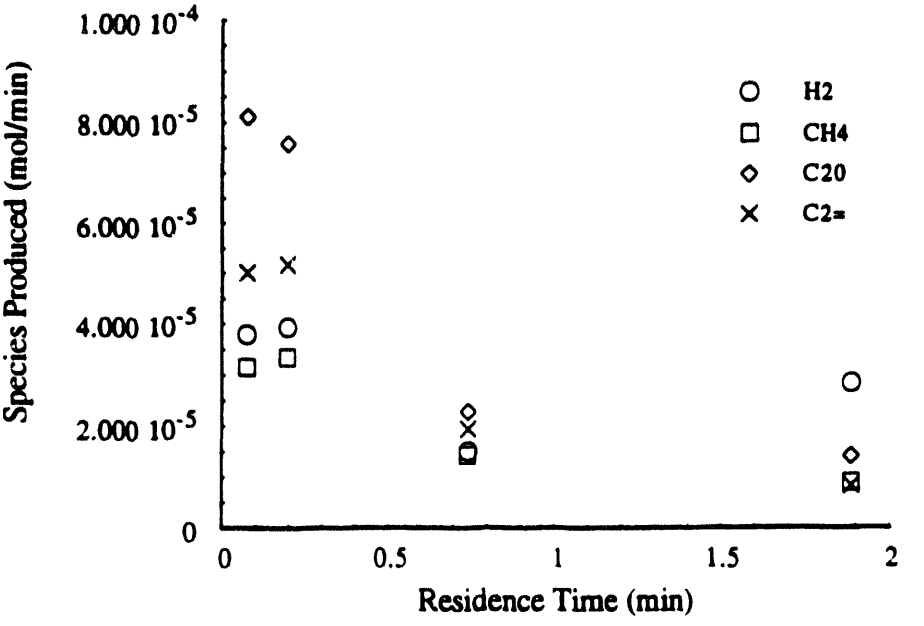


Figure 8. Variations of Some Gaseous Products with Residence Time at 600°C.

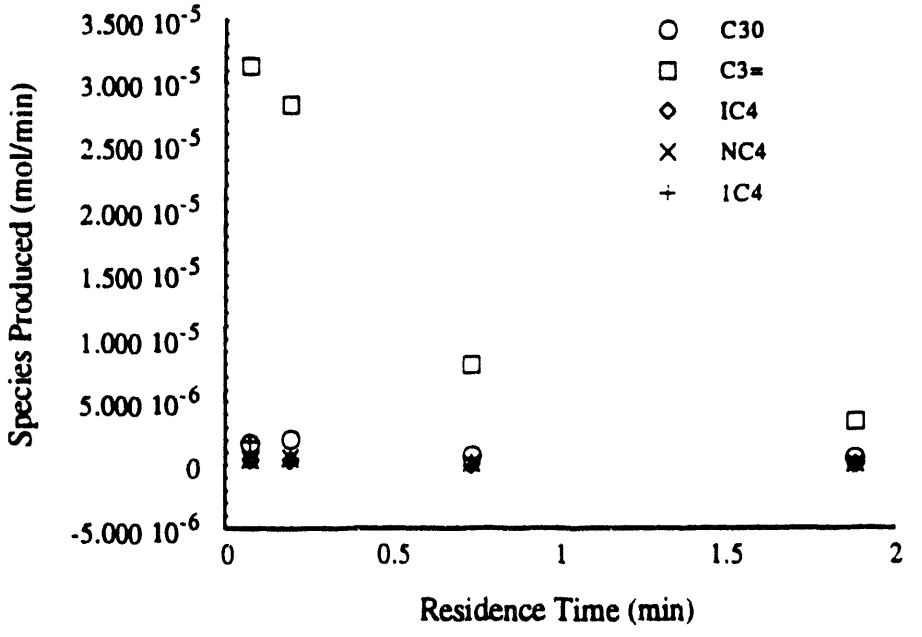


Figure 9. Variations of Some Gaseous Products with Residence Time at 600°C.

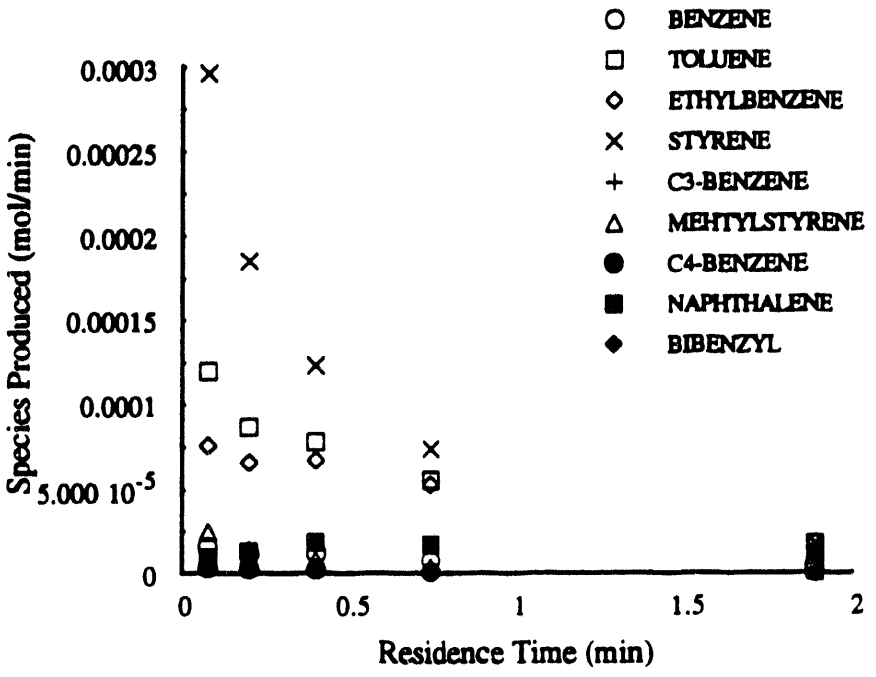


Figure 10. Variations of Major Liquid Products with Residence Time at 600°C.

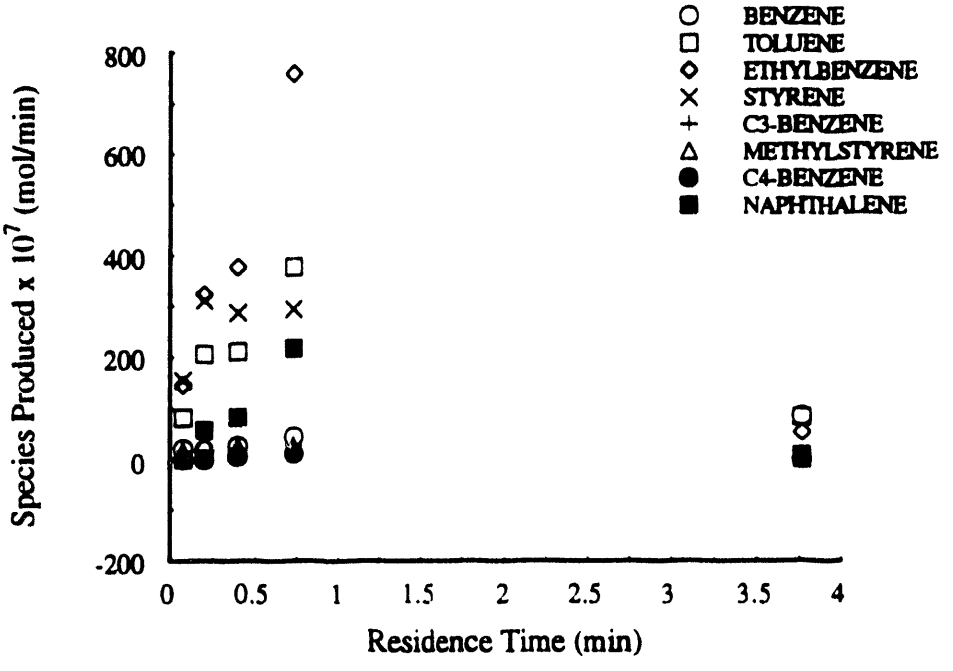


Figure 11. Variations of Some Major Liquid Products with Residence Time at 550°C.

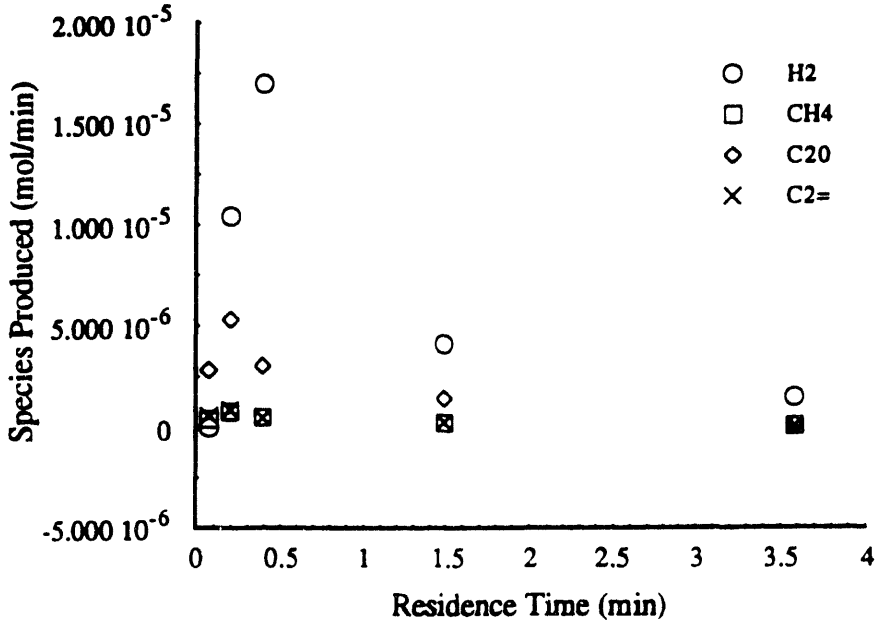


Figure 12. Variations of Some Gaseous Products with Residence Time at 500°C.

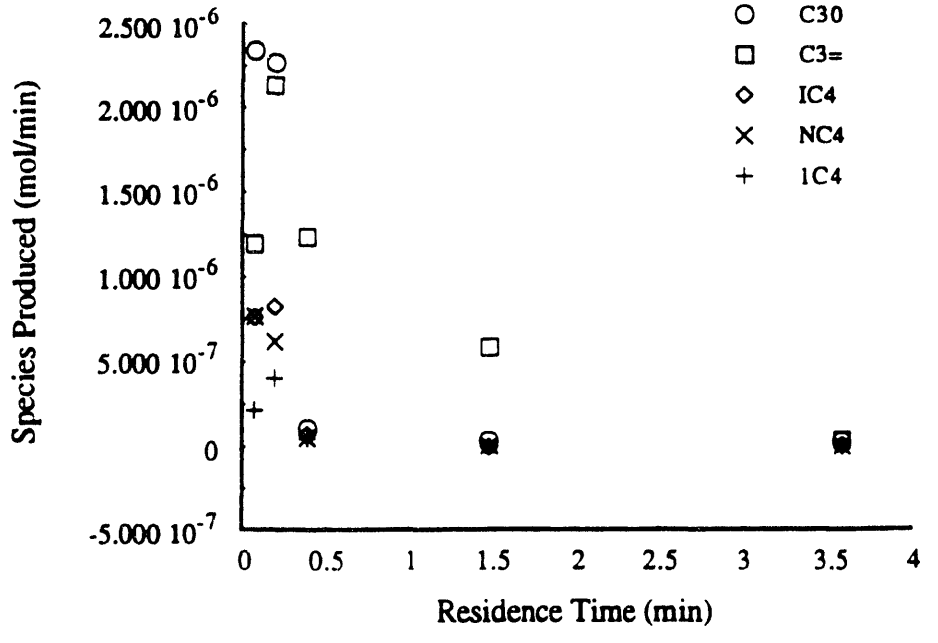


Figure 13. Variations of Some Gaseous Products with Residence Time at 500°C.

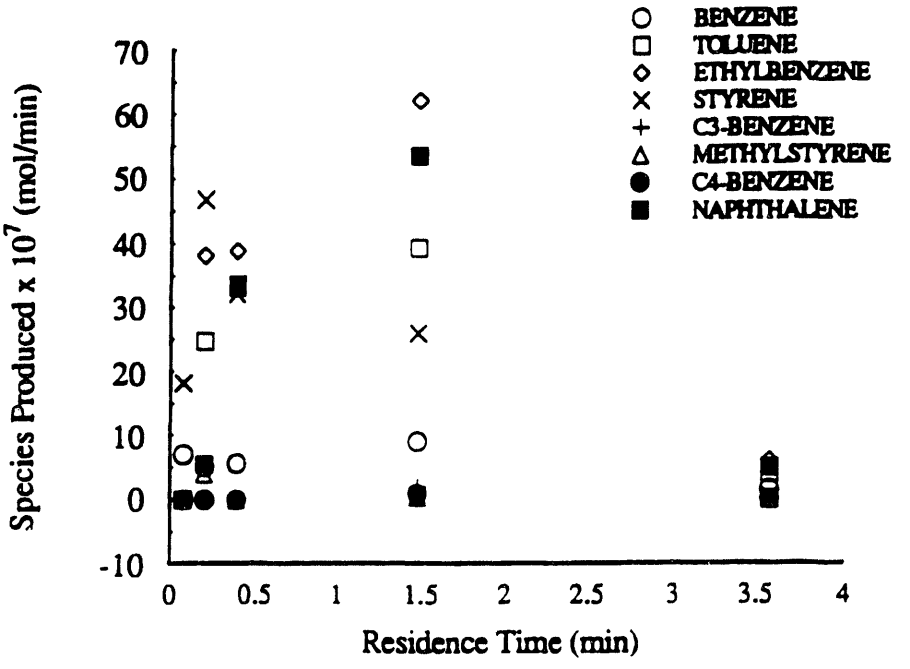


Figure 14. Variations of Major Liquid Products with Residence Time at 500°C.

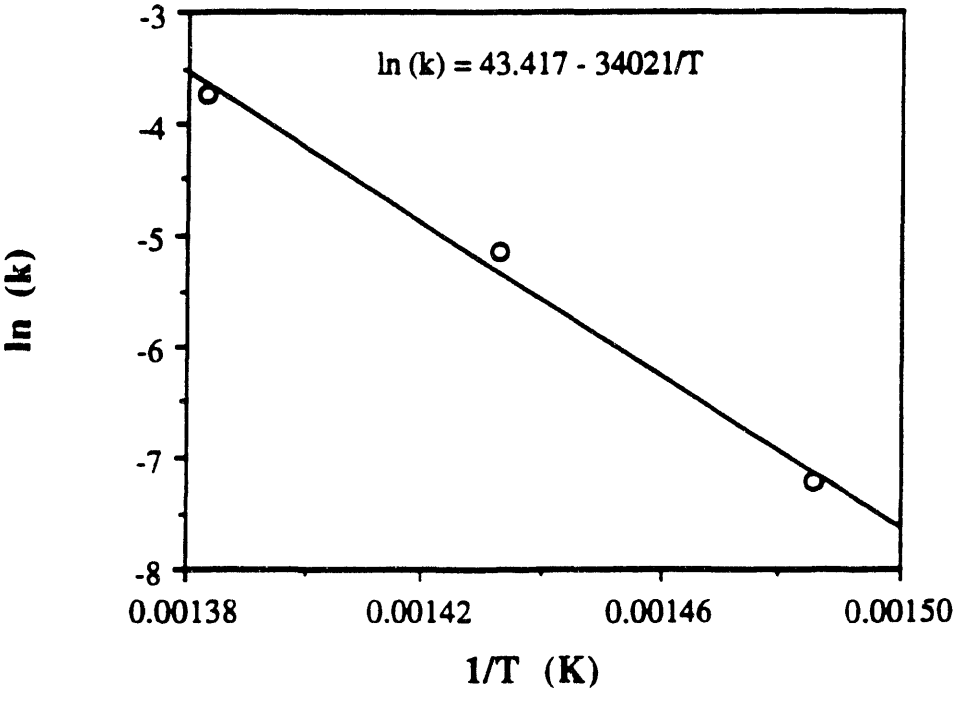


Figure 15. Arrhenius Plot for the Pyrolysis of n-Tetradecane.

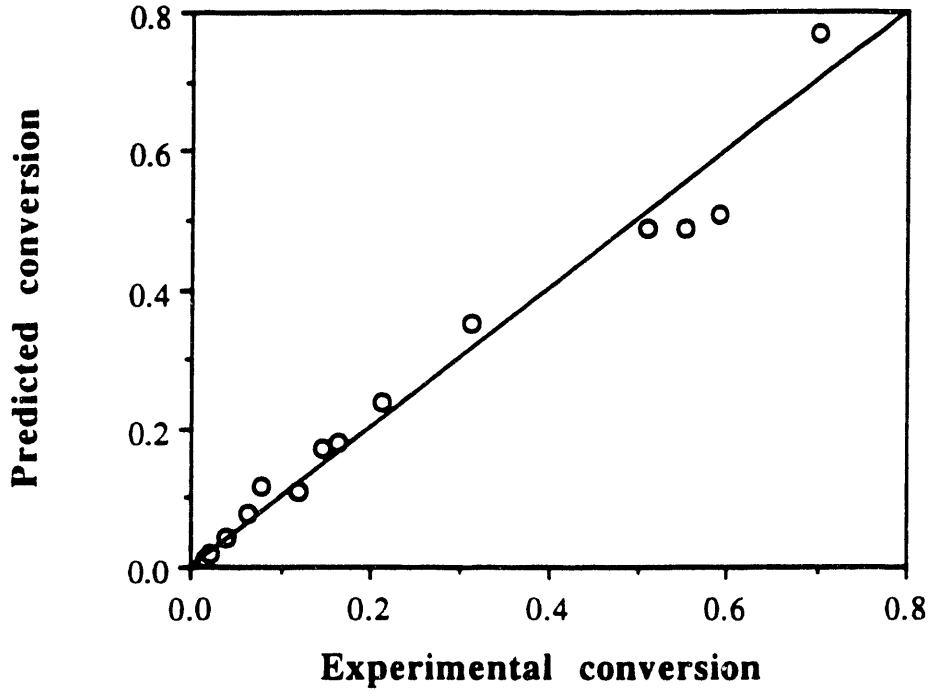


Figure 16. Predicted versus Measured Values of n-Tetradecane Conversion between 400 and 450°C.

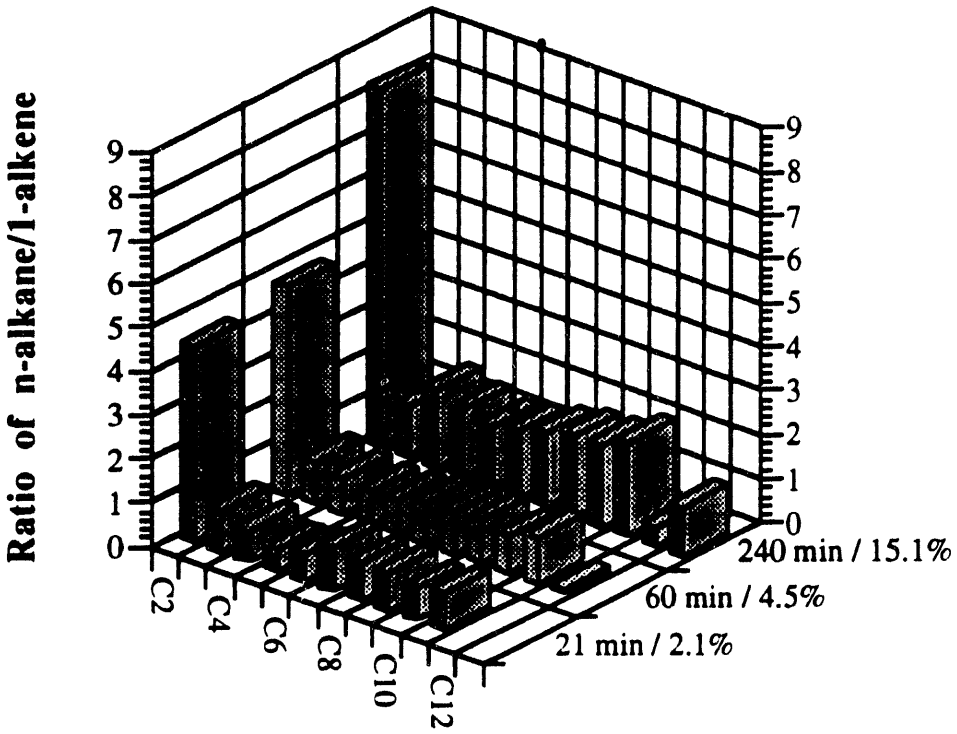


Figure 17. Ratio of n-Alkane to the Corresponding 1-Alkene for $C_2$-$C_{13}$ Products from the Pyrolysis of n-Tetradecane at 400°C.

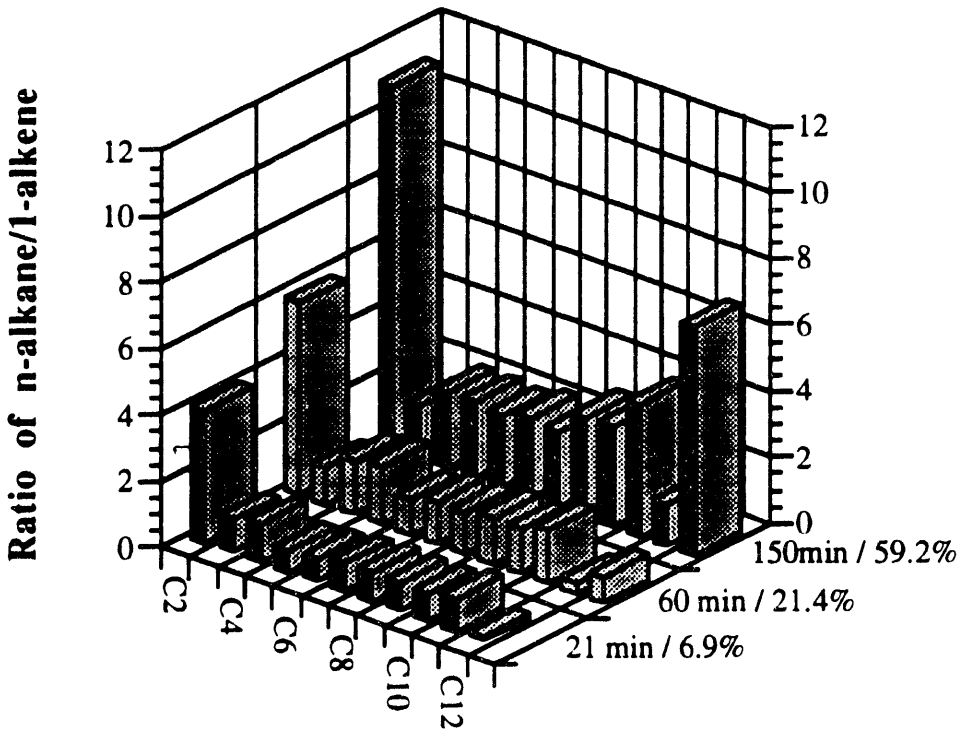


Figure 18. Ratio of n-Alkane to the Corresponding 1-Alkene for $C_2$-$C_{13}$ Products from the Pyrolysis of n-Tetradecane at 425°C.

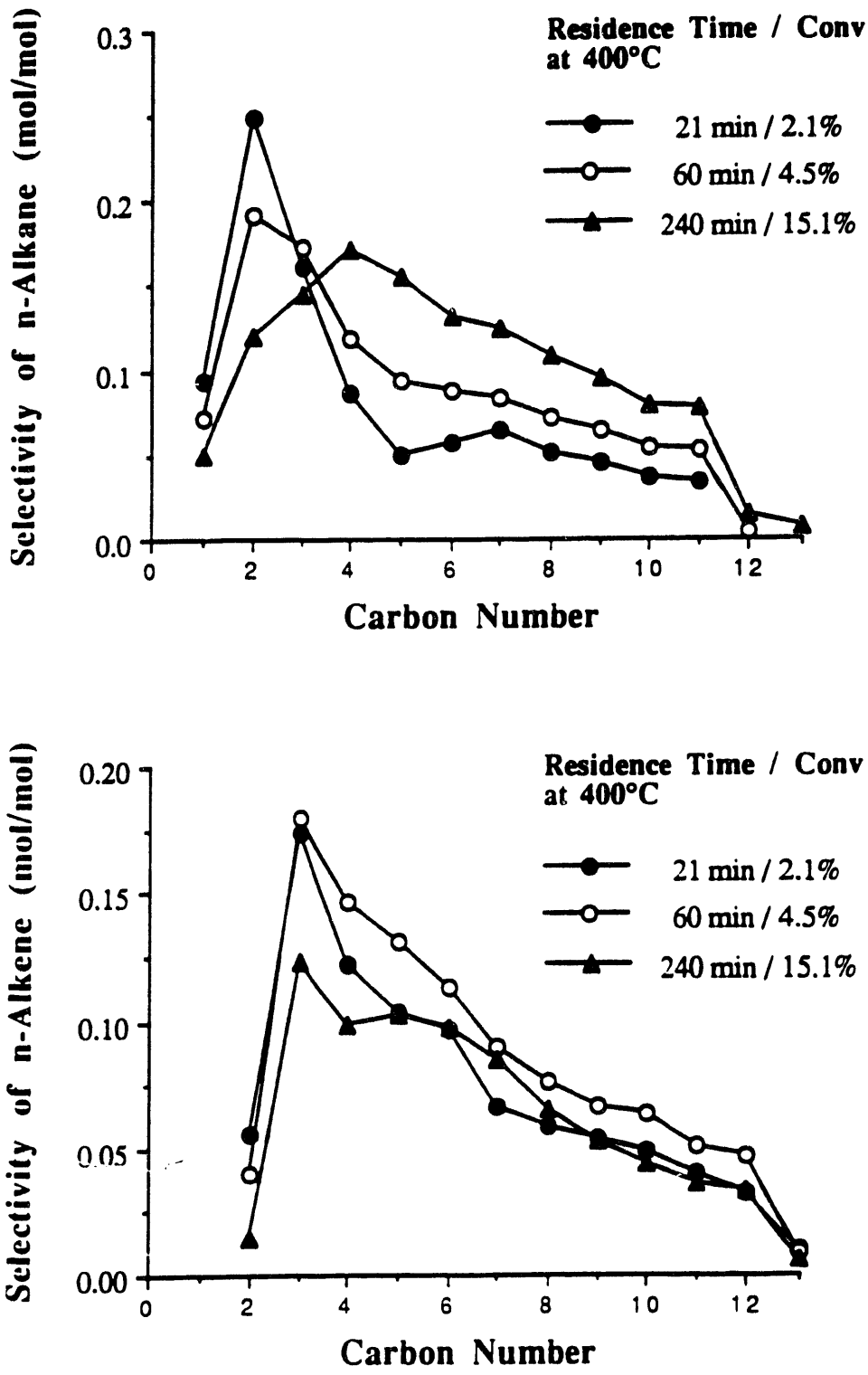


Figure 19. The n-$C_{14}$Selectivity to n-Alkanes (Top) and 1-Alkenes (Bottom) at 400 °C under Initial $N_2$ Pressure of 0.69 MPa (Cold

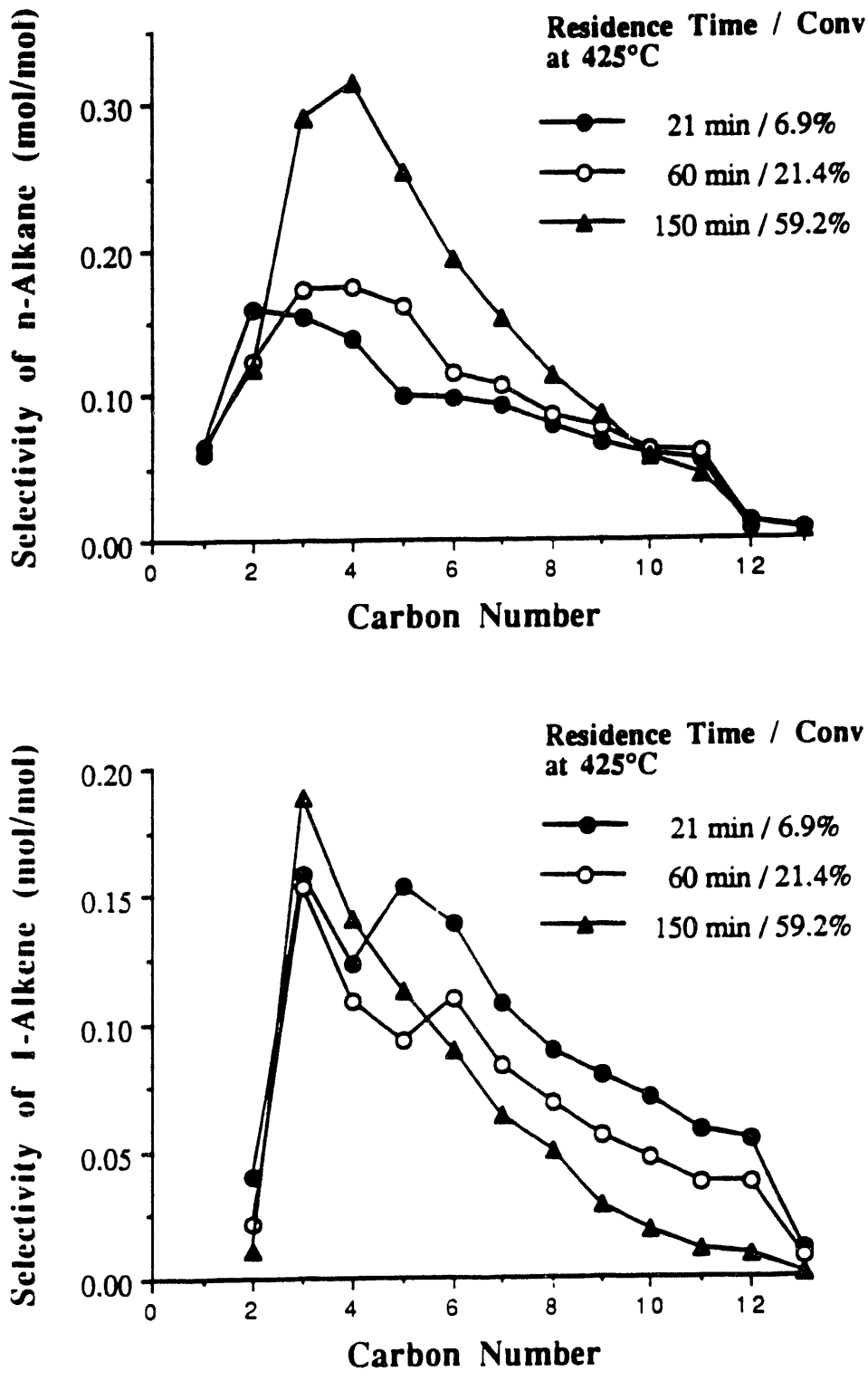


Figure 20. The n-$C_{14}$ Selectivity to n-Alkanes (Top) and 1-Alkenes (Bottom) at 425°C under Initial $N_2$ Pressure of 0.69 MPa (Cold).

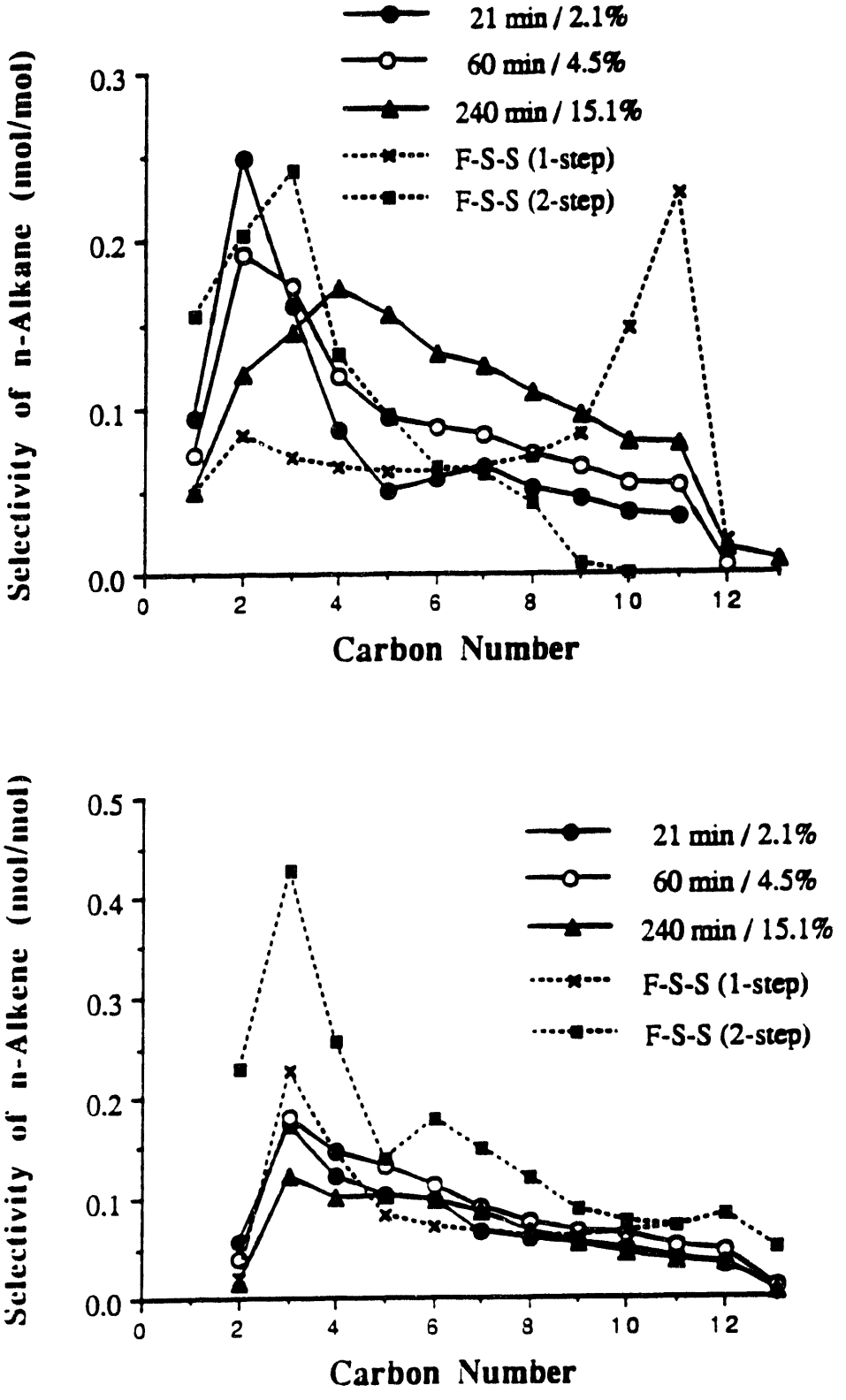


Figure 21. The Predicted versus Measured n-$C_{14}$ Selectivity to n-Alkanes (Top) and 1-Alkenes (Bottom) at 400 °C under Initial $N_2$Pressure of 0.69 MPa (Cold).

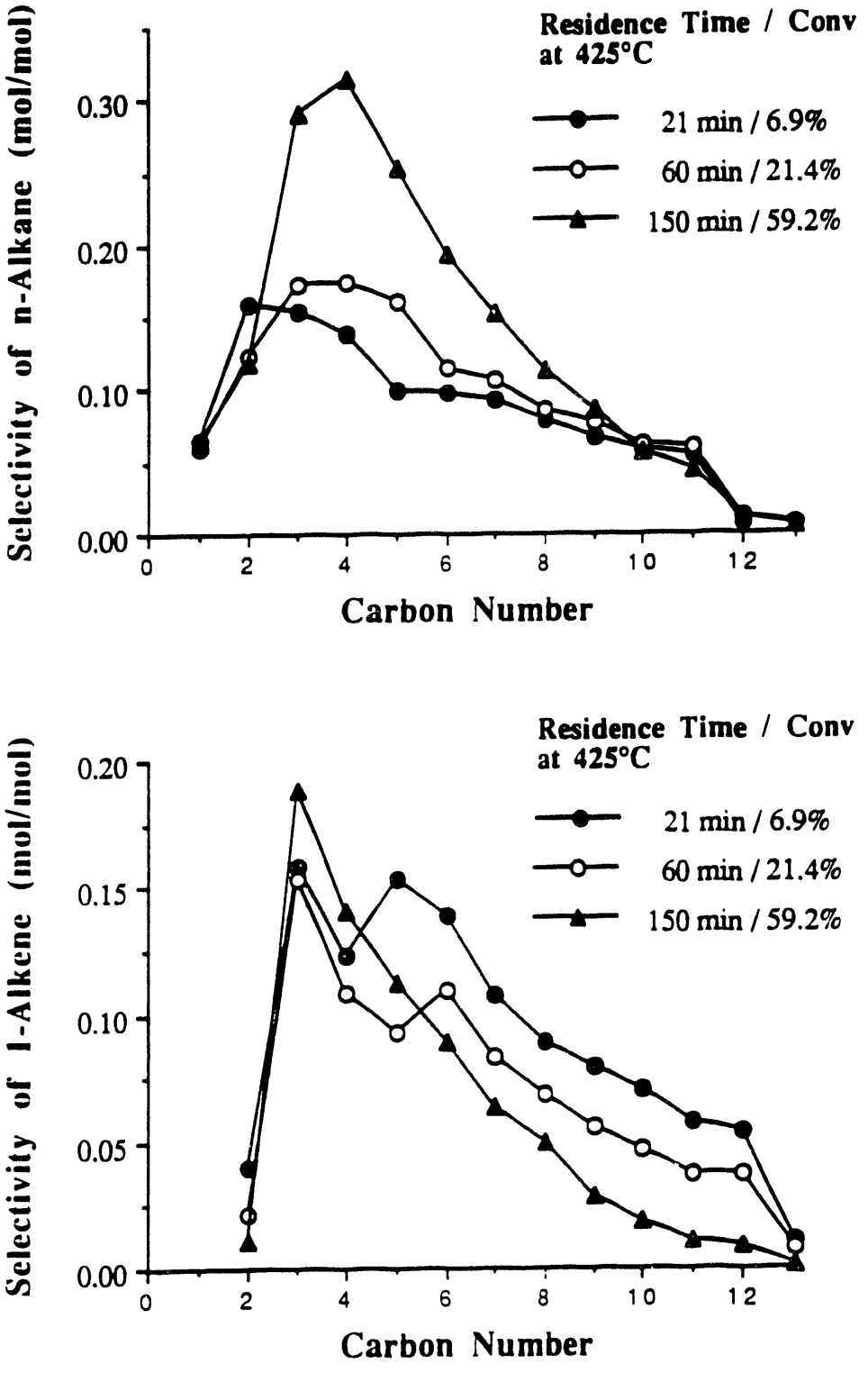


Figure 20. The n-$C_{14}$ Selectivity to n-Alkanes (Top) and 1-Alkenes (Bottom) at 425°C under Initial $N_2$ Pressure of 0.69 MPa (Cold).

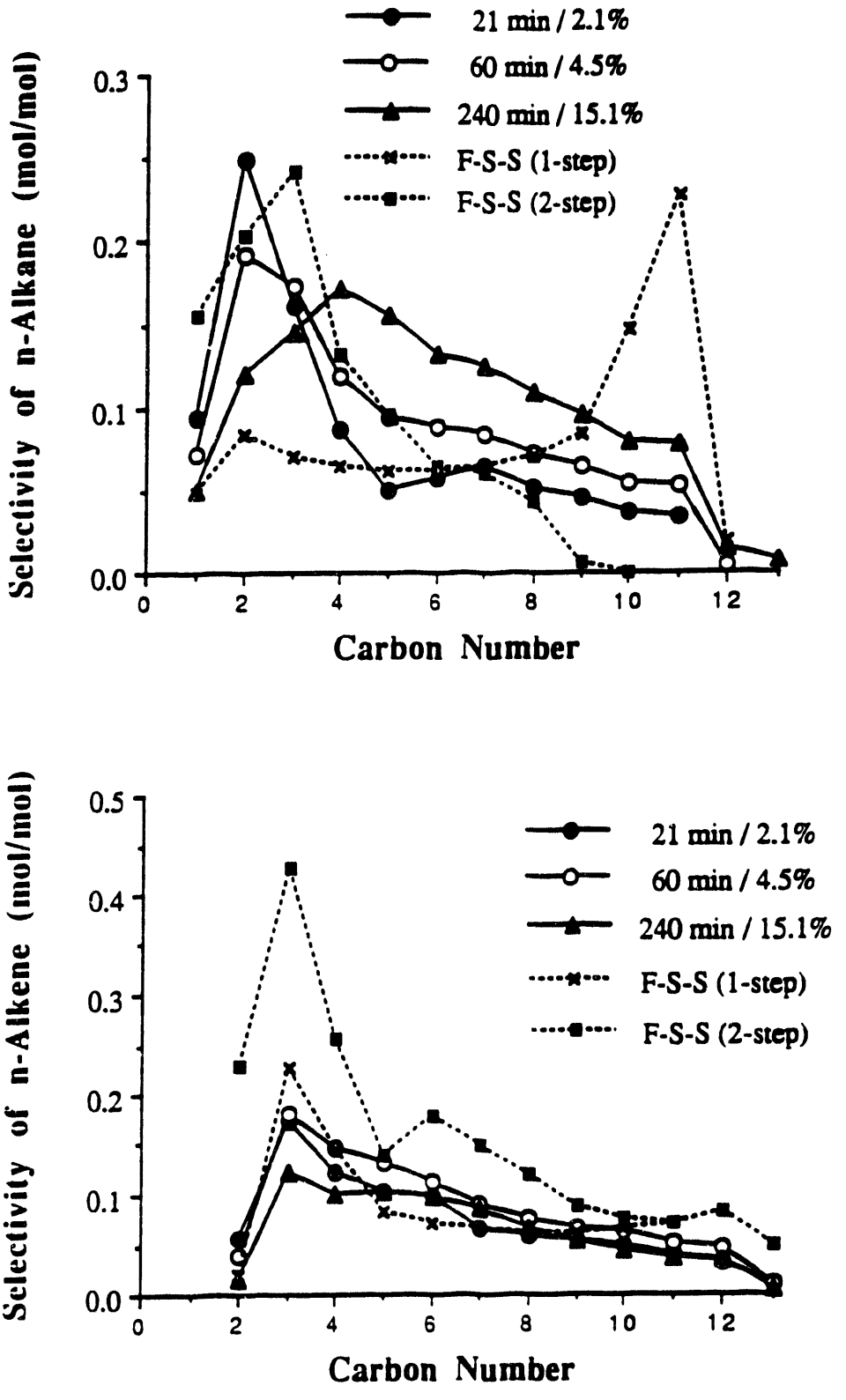


Figure 21. The Predicted versus Measured n-$C_{14}$ Selectivity to n-Alkanes (Top) and 1-Alkenes (Bottom) at 400 °C under Initial $N_2$Pressure of 0.69 MPa (Cold).

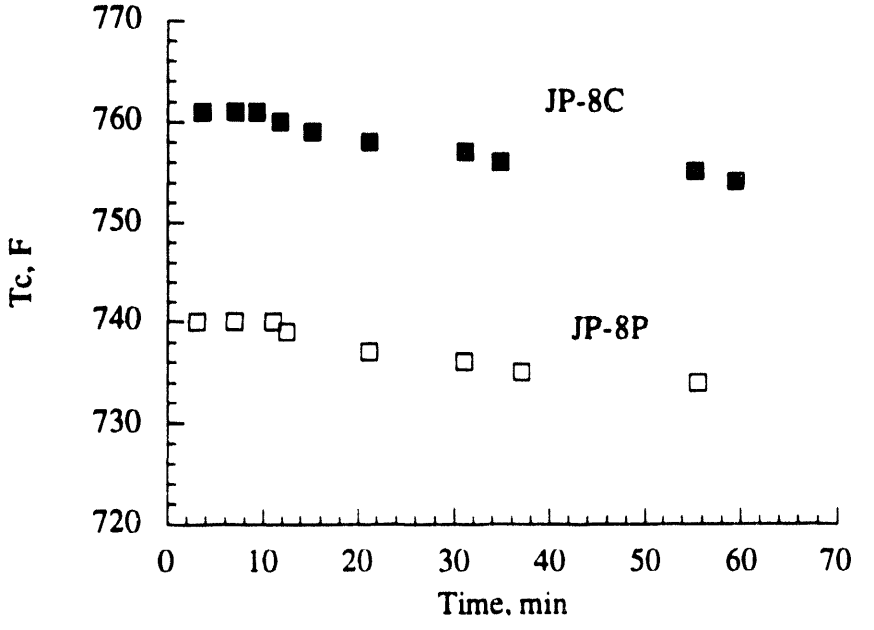


Figure 22. Change of Observed Critical Temperature with Time for JP-8P and JP-8C.

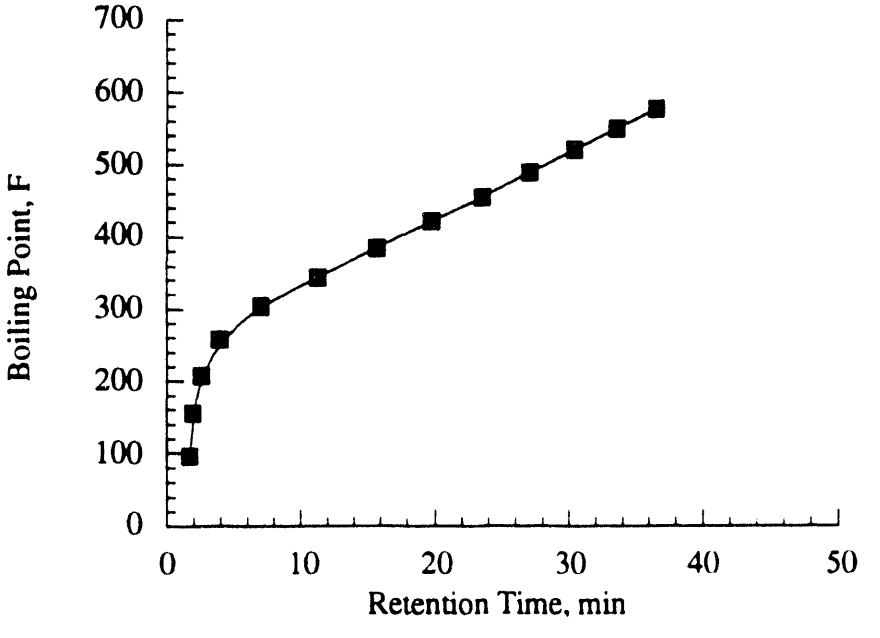


Figure 23. Calibration Curve.

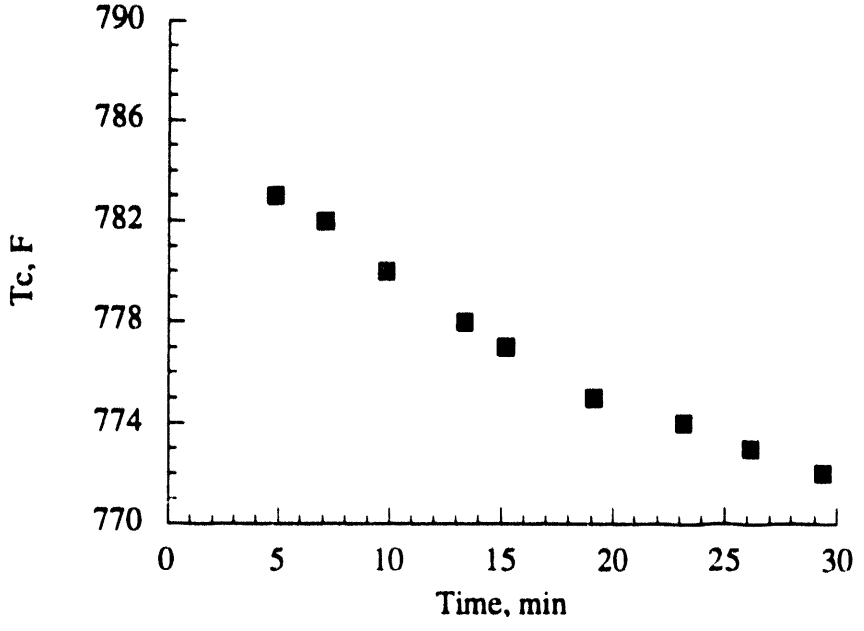


Figure 24. Change of Observed Critical Temperature with Time for n-Tetradecane

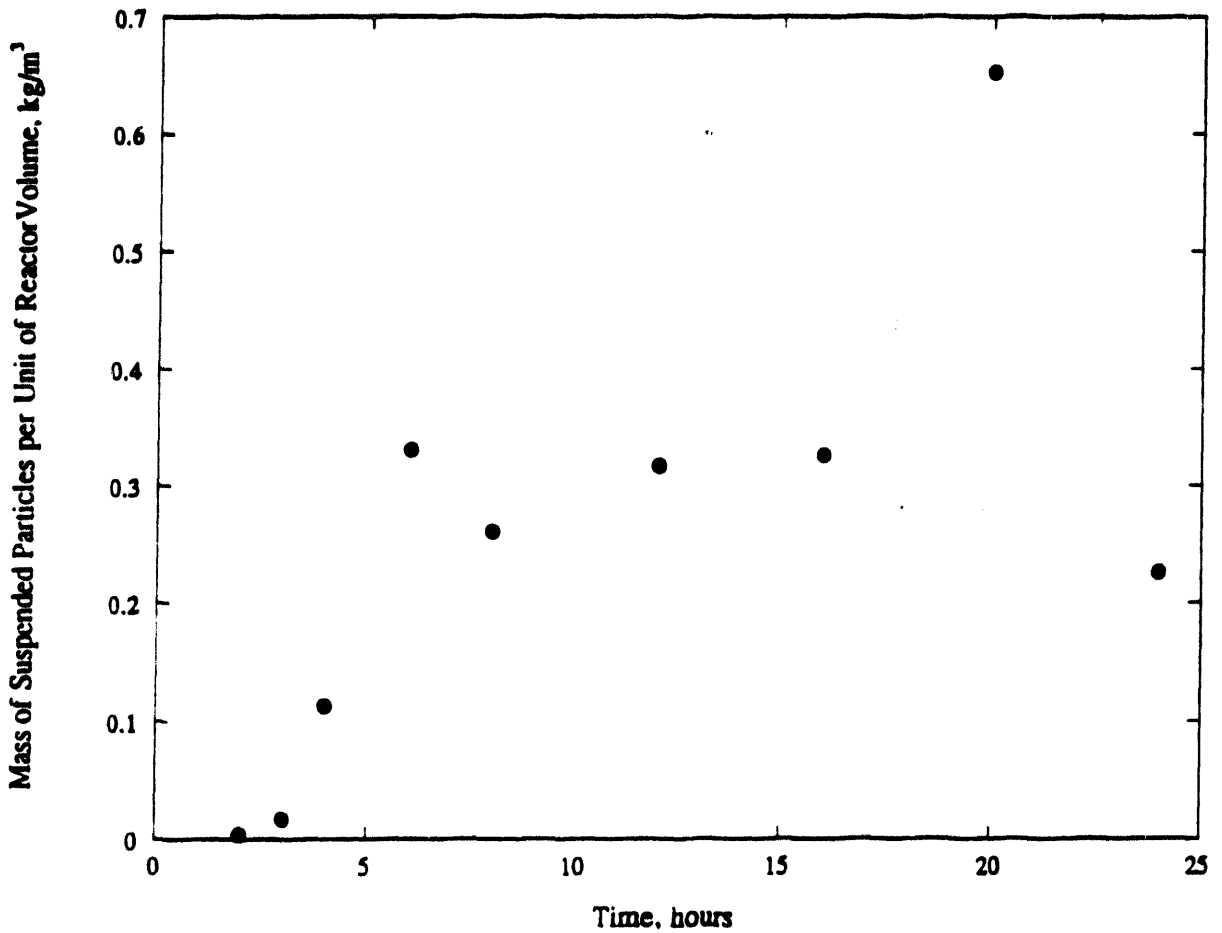


Figure 25. Concentration of Particles suspended in the Liquid Products at the End of the Stressing Period. The Particles are Assumed, for the Purposes of the Calculations of Deposit Growth, to be Uniformly Distributed Throughout tthe Fuel Vapor in the Reactor, under the High Temperature and High Pressure Conditions of the Experiments.

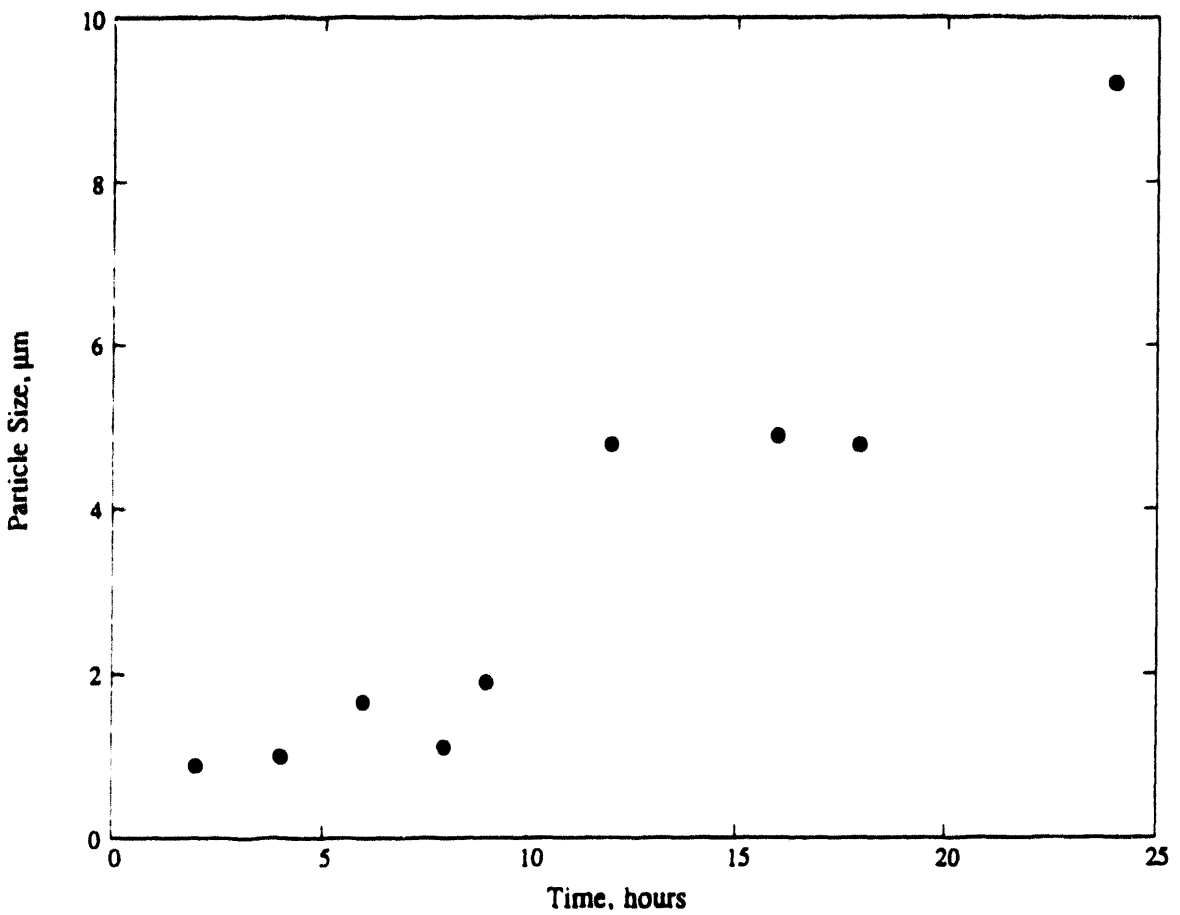


Figure 26. Volumne-Based Mean Size of Suspended Particles as a Function of Time, Determined by Light Scattering (Horiba LA-900).

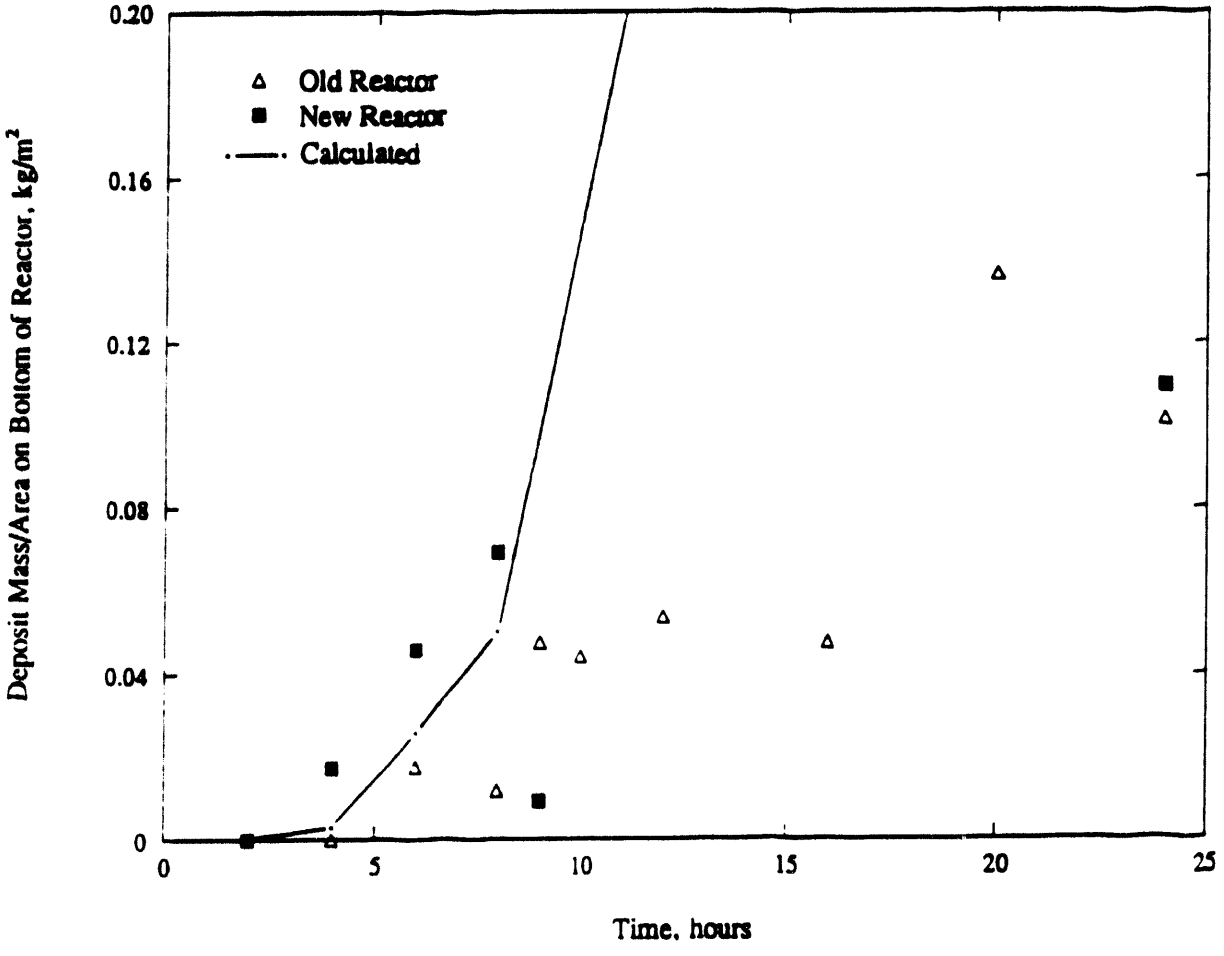


Figure 27. Measured Mass/Area of Deposits Formed from Mixtures of 81.5 wt% JP-8C and 18.5 wt% Tetradecane at 450°C under Nitrogen, and comparison with Calculated growth of Deposits by Settling.

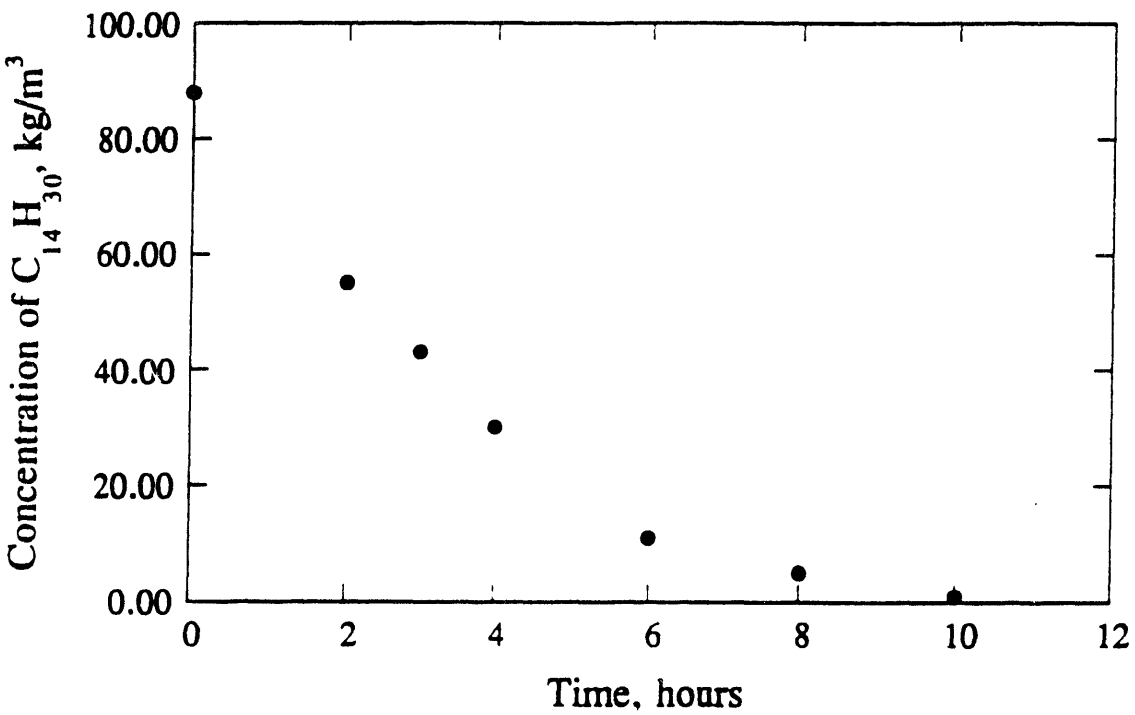


Figure 28. Disappearance of tetradecane with stressing time, in mixtures of 18.5wt% tetradecane with coal-derived jt fue, determined by GC-MS analysis of the liquid remaining at the end of each experiment

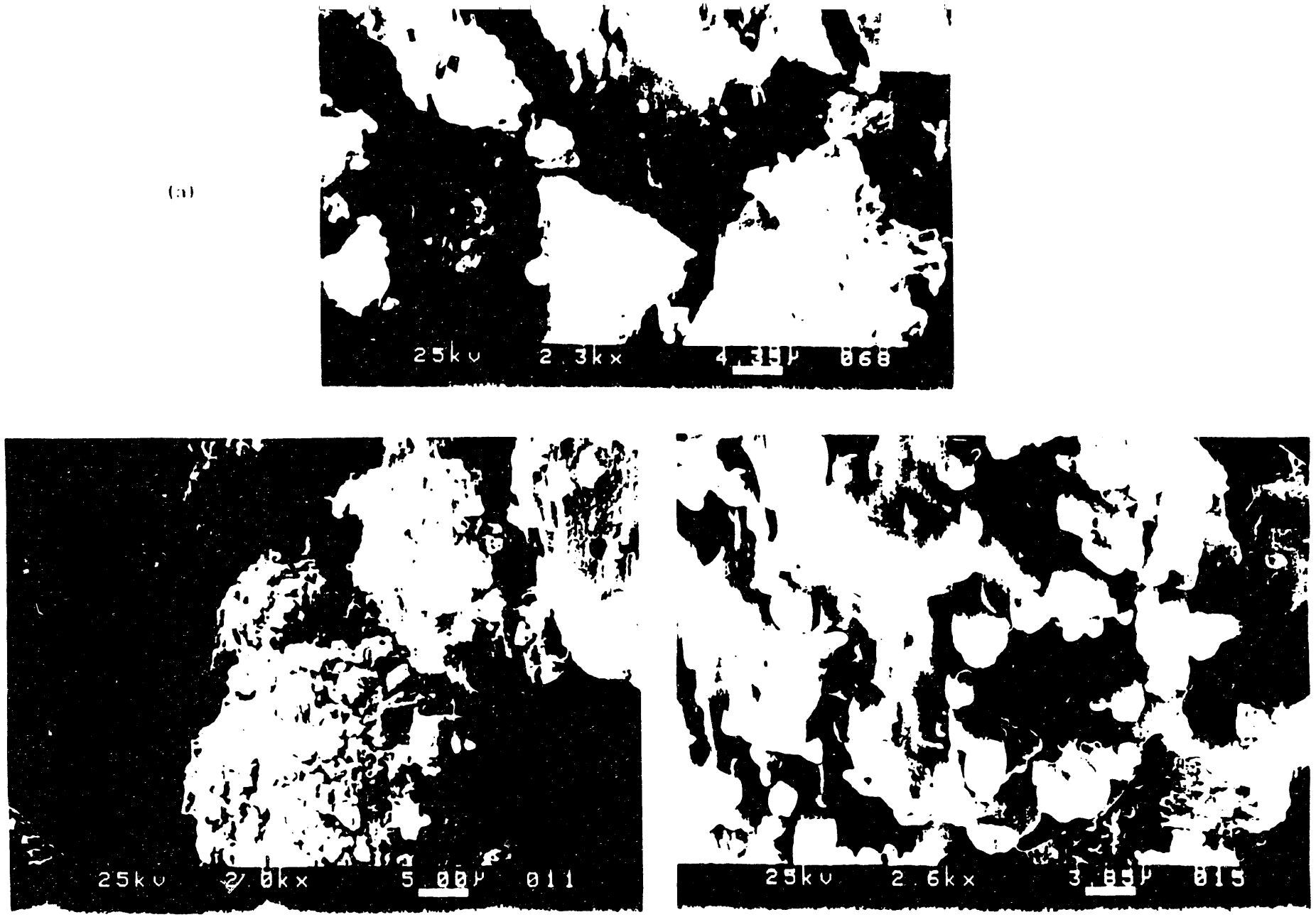


Figure 29. Scanning-Electron Micrographs of Activated Carbon PX-21. (a) - Original Activated Carbon PX-21; (b) - PX-21 Treated 3 days with JPTS Jet Fuel, not Stressed; (c) - PX-21 Stressed with JPTS, 450°C, 5hNitrogen

(a)

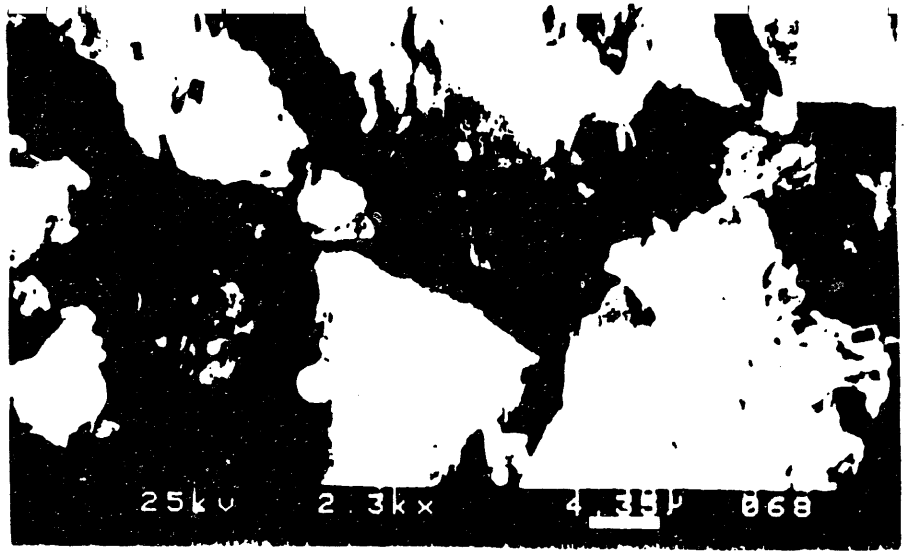


(b)

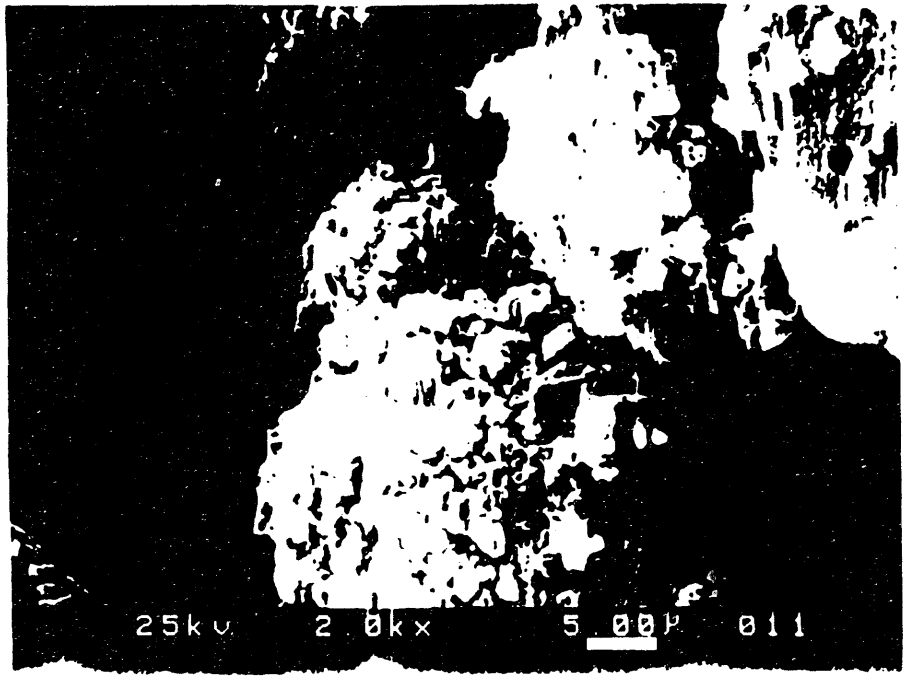


(c)

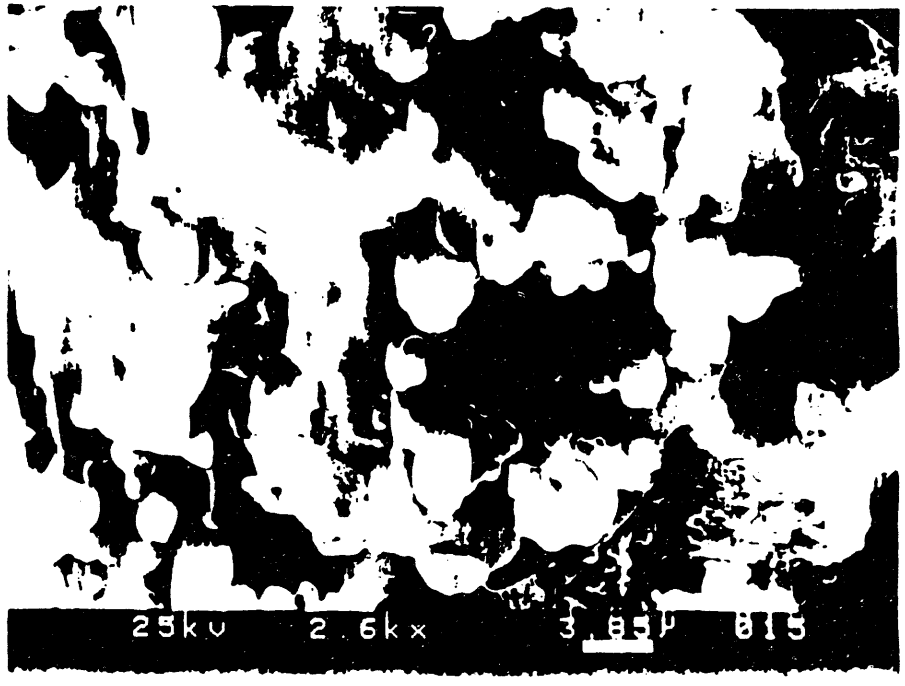


Figure 29. Scanning-Electron Micrographs of Activated Carbon PX-21. (a) - Original Activated Carbon PX-21; (b) - PX-21 Treated 3 days with JPTS Jet Fuel, not Stressed; (c) - PX-21 Stressed with JPTS, 450°C, 5hNitrogen

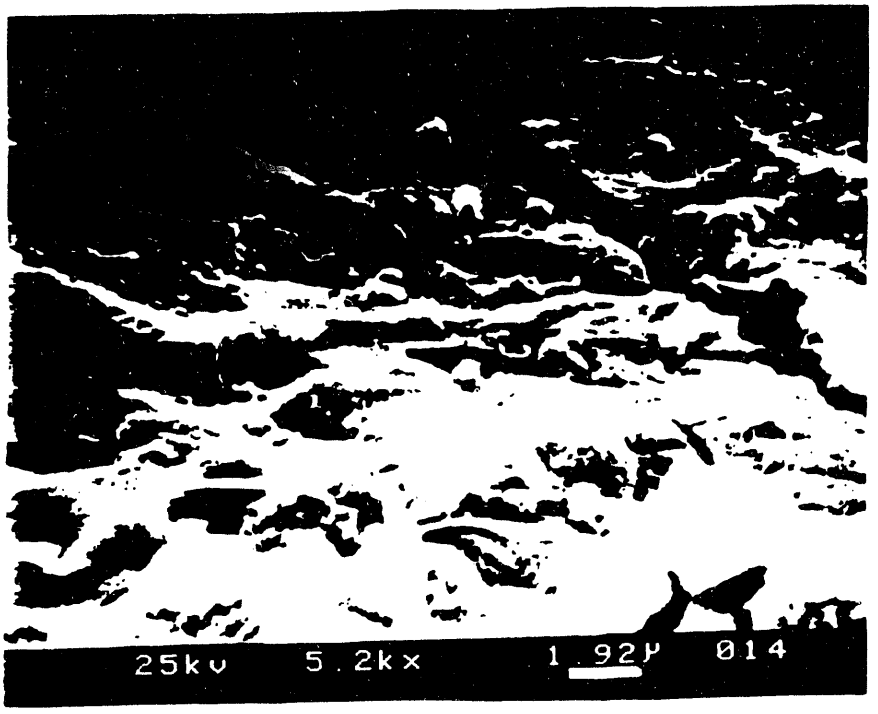


(a)

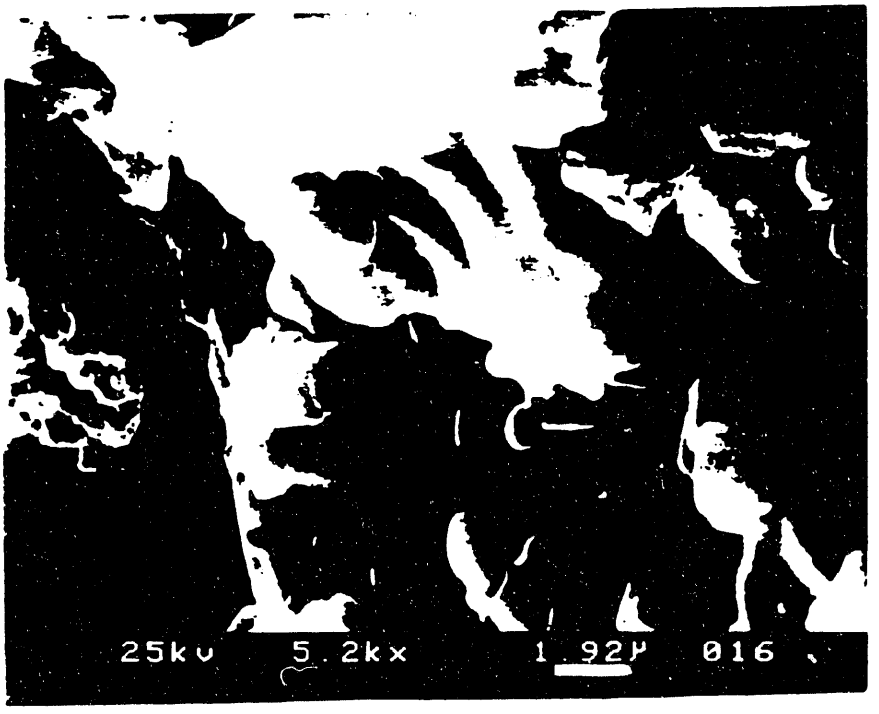


(b)

Figure 30. Scanning-Electron Micrographs of Activated Carbon PX-21
(a) - PX-21 Treated 3 Days with JPTS Jet Fuel, not Stressed;
(b) - PX-21 Stressed with JPTS, 450°C, 5h, Nitrogen

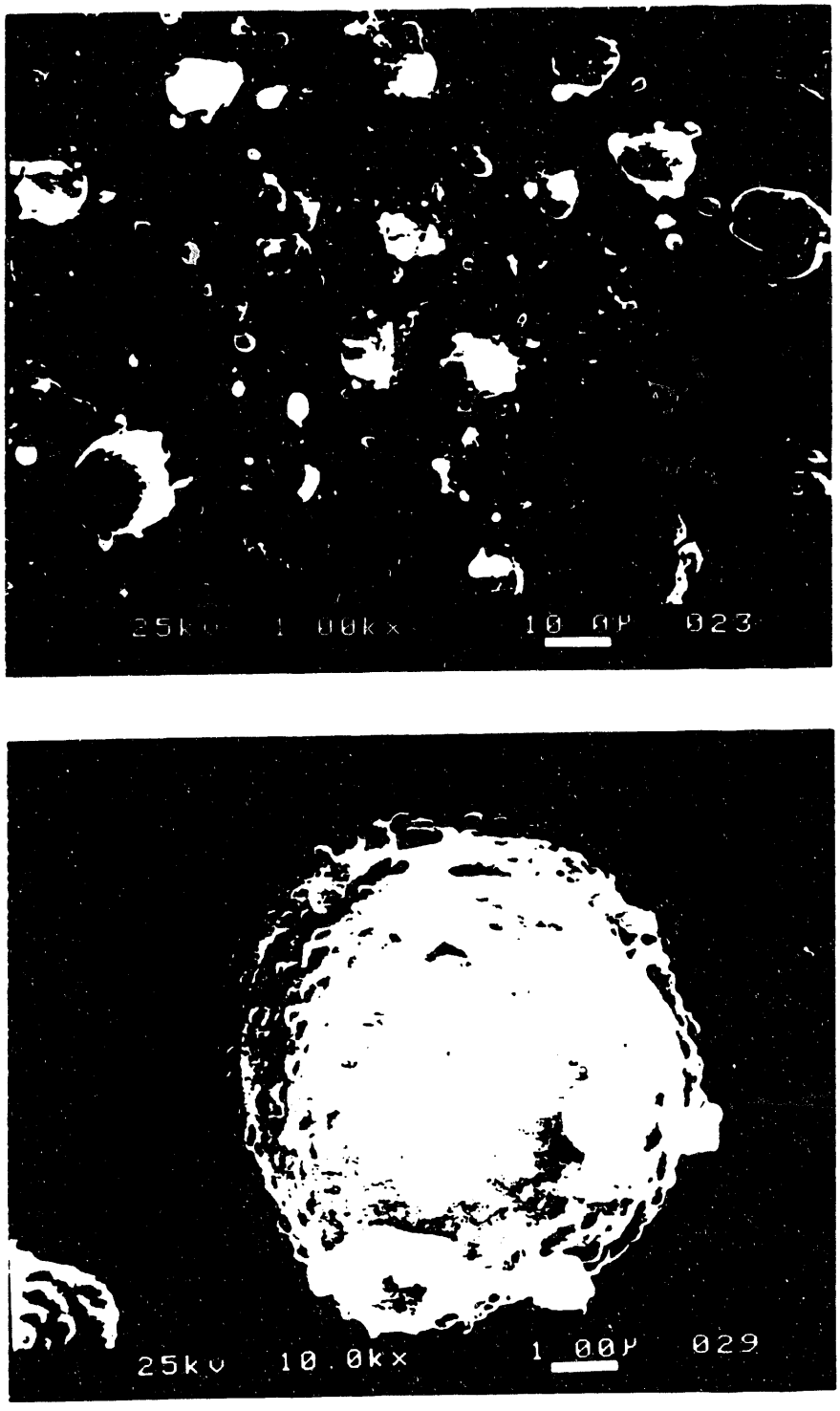


Figure 31. (a) Particulate Carbon Deposit on Top Nickel Coupon after 3 Hour Reaction at 450 °C, (b) Particulate Carbon Deposit on Bottom Nickel Coupon under the Same Condition.

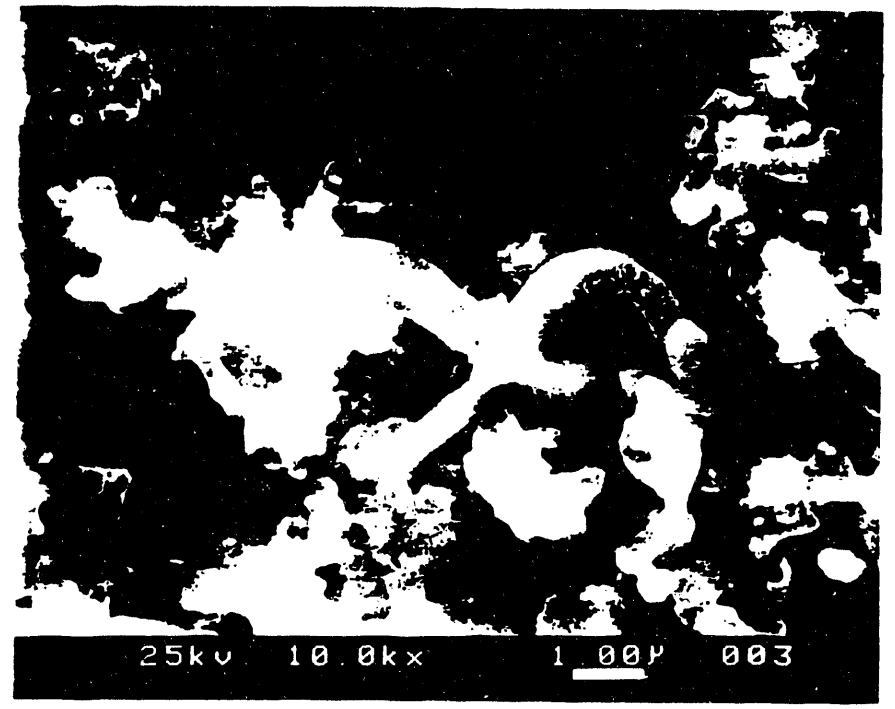


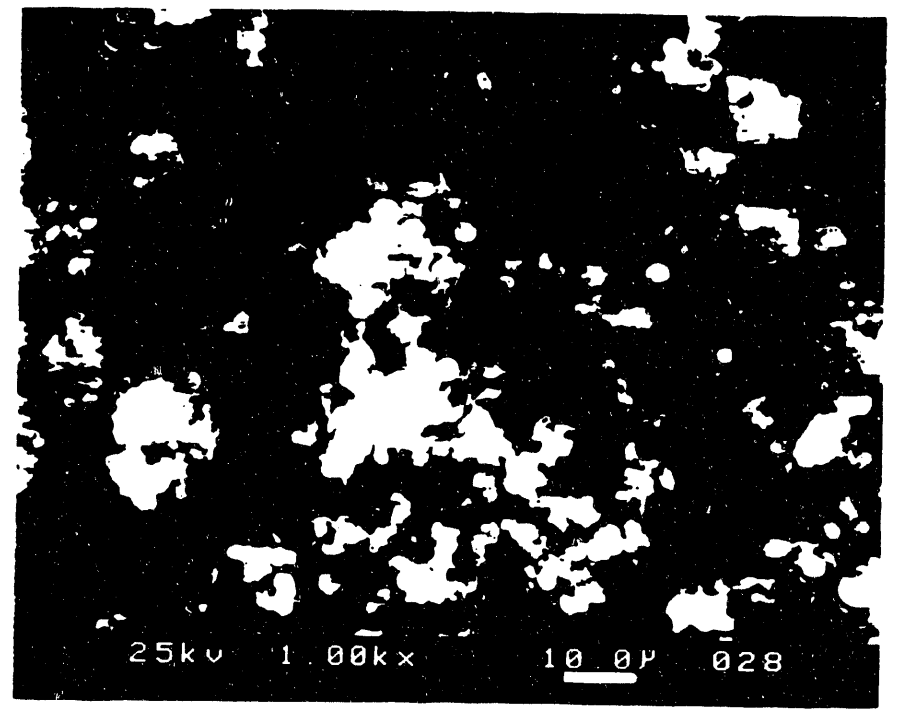


Figure 32. (a) Filamentous Carbon Deposit Formation on Bottom Nickel Coupon after 5 Hour Reaction at 450 °C. (b) Porous Carbon Deposit Aggregates on Top Nickel Coupon after 5 Hour Reaction at 450 °C.

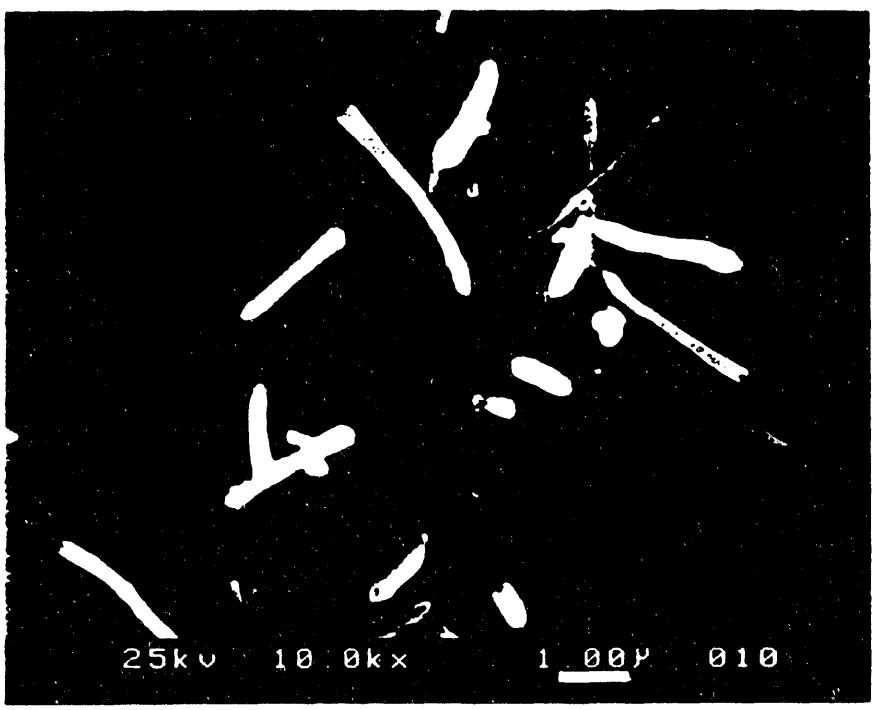


Figure 33. Needle-Like Deposit on Top Copper Coupon after 1 Hour Reaction At 450 °C.

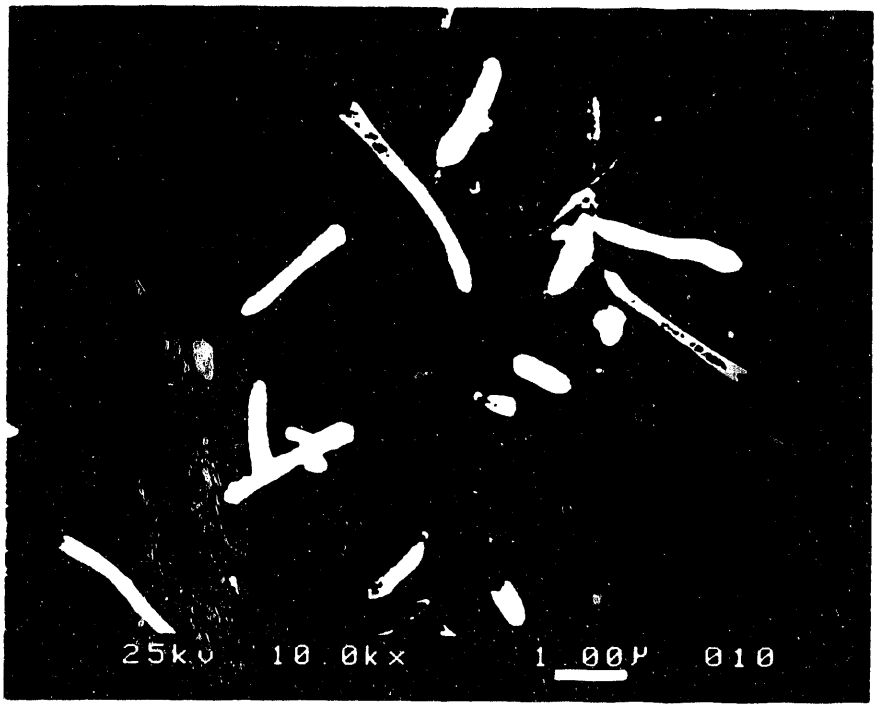


Figure 33. Needle-Like Deposit on Top Copper Coupon after 1 Hour Reaction At 450 °C.

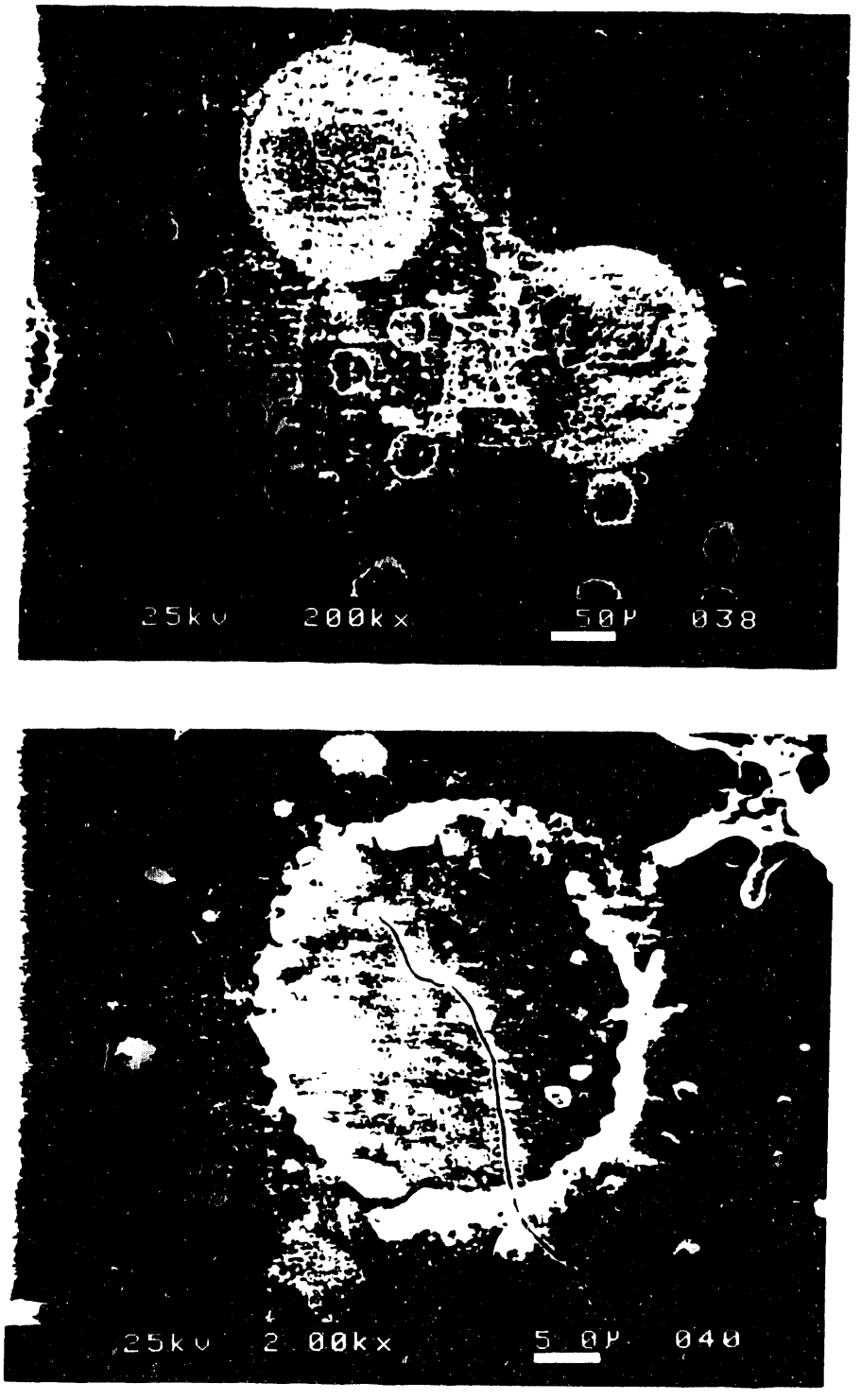


Figure 34. (a) Deposit Rings Formed on Bottom Copper Coupon after 3 Hour Reaction at 450 °C. (b) Same Condition, Showing the Initial Growth Stages of These Deposit Rings on Carbon Surface.

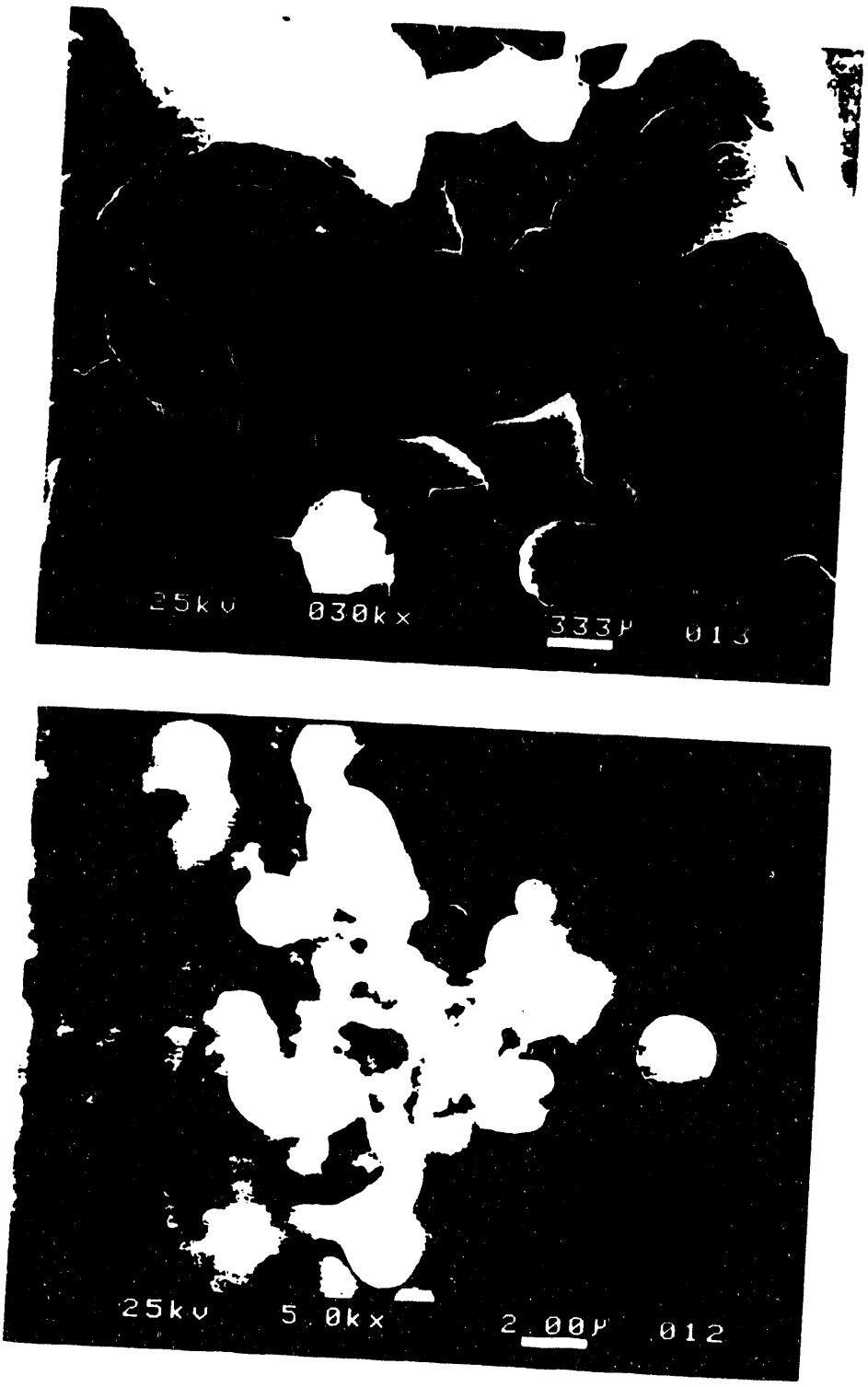


Figure 35. (a) Circular Strips of Deposit Layer and Rings on Top Copper Coupon after 5 Hour Reaction at 450 °C, (b)Same Condition,Showing Briefly Coalesced Carbon Particles to Form the Deposit Rings.

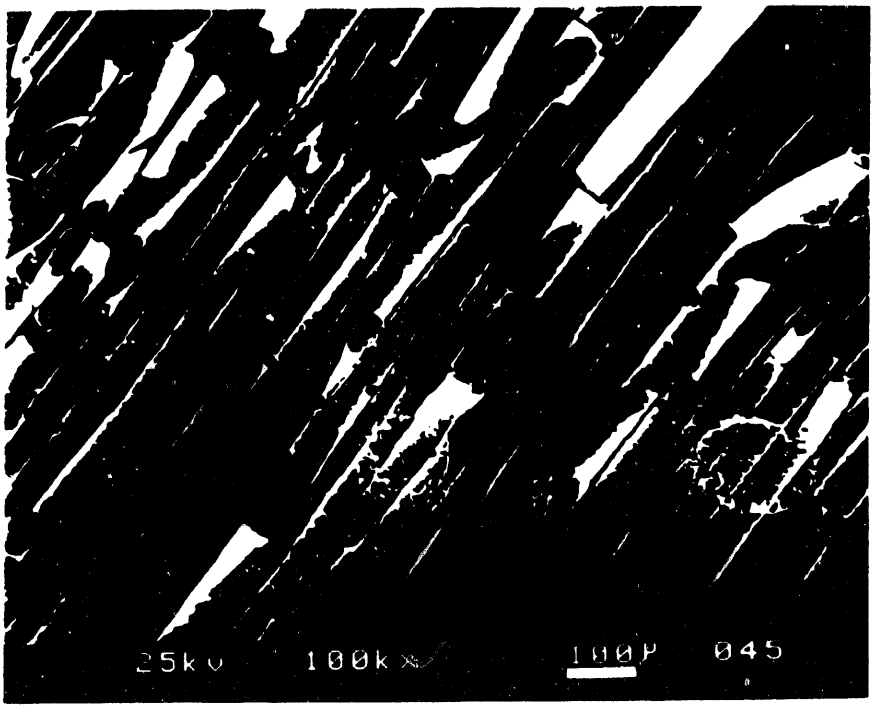


Figure 36. Straight Strips of Deposit Layer and Rings on Top Aluminum Coupon after 3 Hour Reaction at 450 °C.

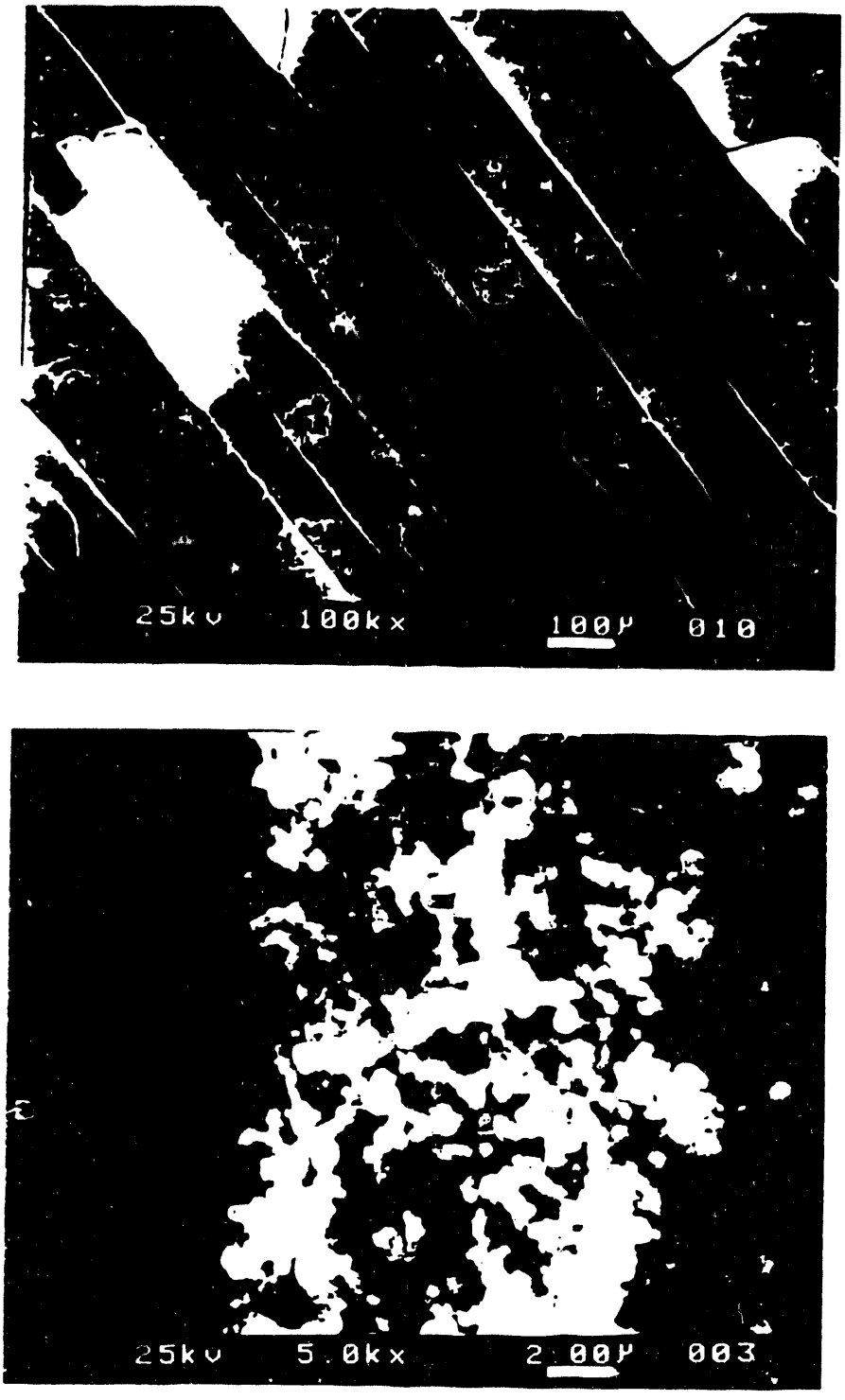


Figure 37. (a) Straight Strips of Deposit Layer and Rings On Bottom Aluminum Coupon after 5 Hour Reaction at 450 °C, (b) Same Condition, ShowingBriefly

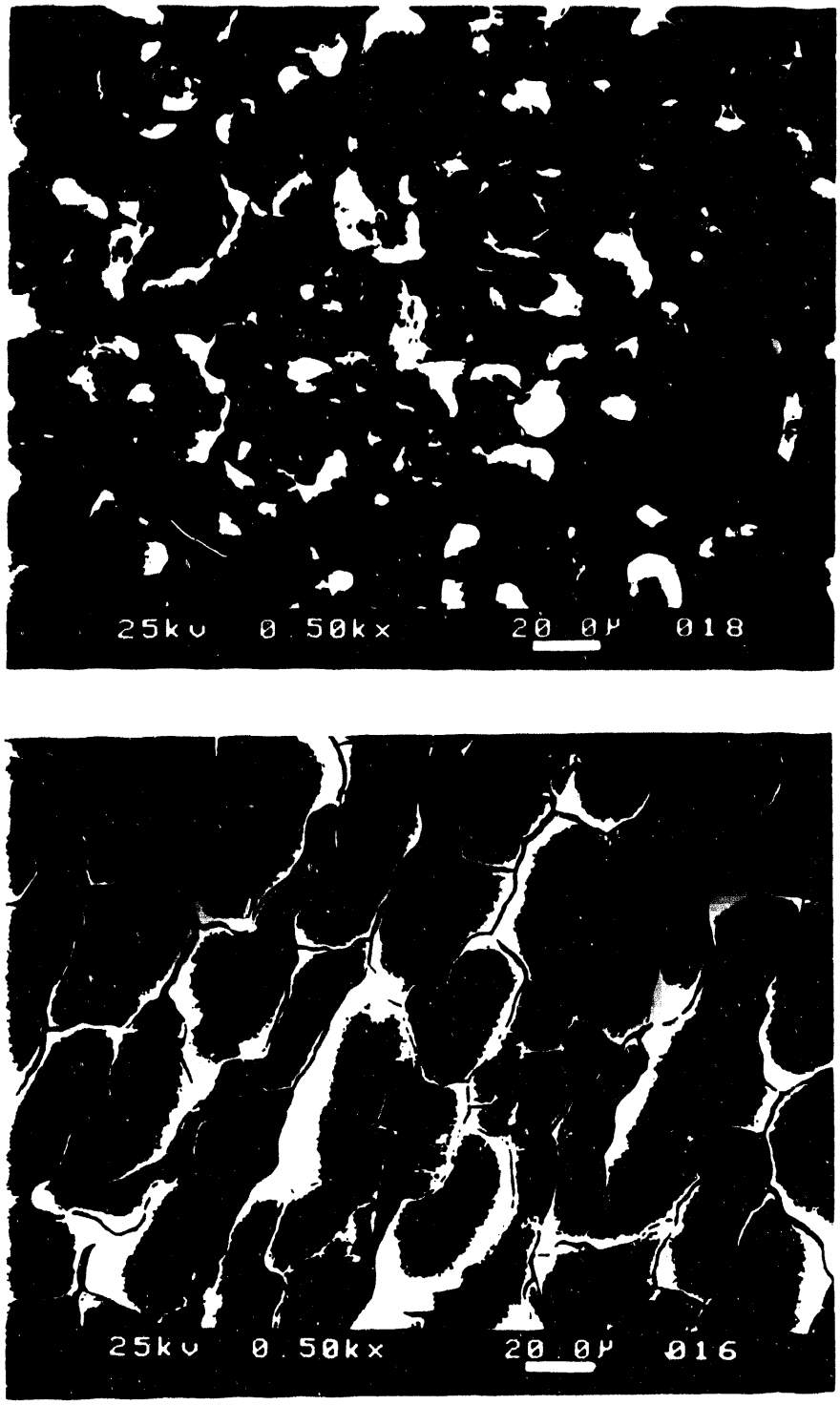


Figure 38. (a) Highly Coalesced Deposit Layer on Bottom Titanium Coupon after 3 Hour Reaction at 450 °C. (B) Fragments of Deposit Layer on Top Titanium Coupon after 3 Hour Reaction at 450 °C.

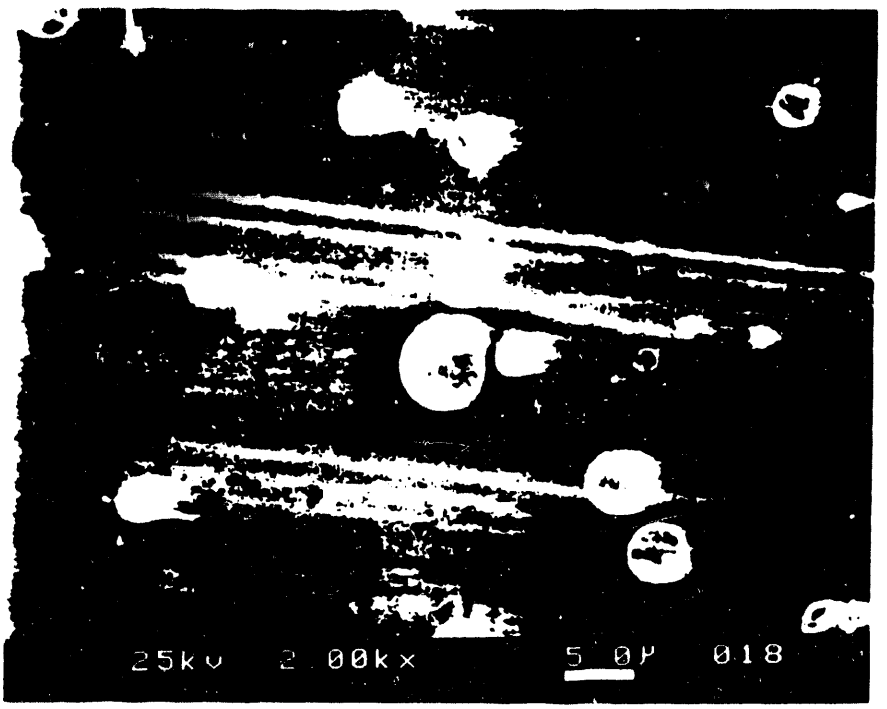


Figure 39. Initial Deposit Formation on Top 304 Stainless Steel Coupon after 3 Hour Reaction at 450 °C.

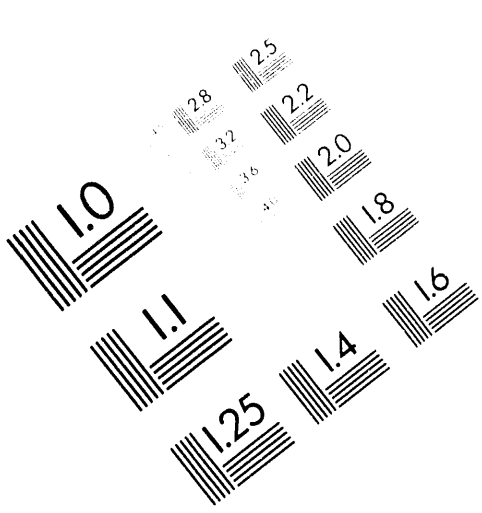



**Association for Information and Image Management**

1100 Wayne Avenue, Suite 1100
Silver Spring, Maryland 20910
301 587 8202

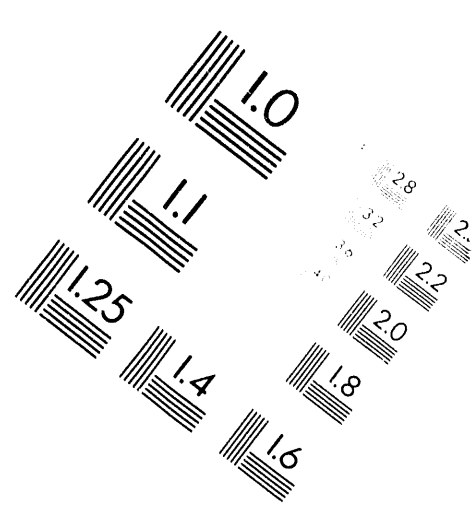


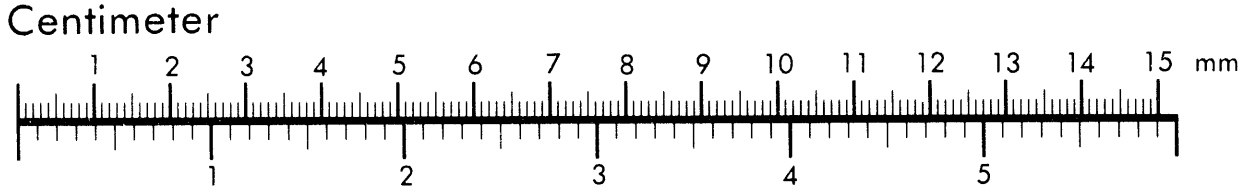


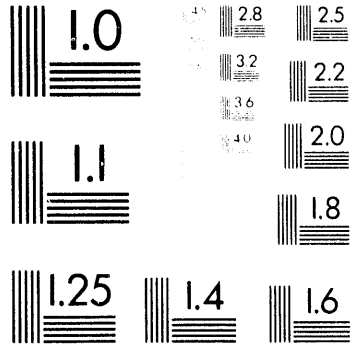


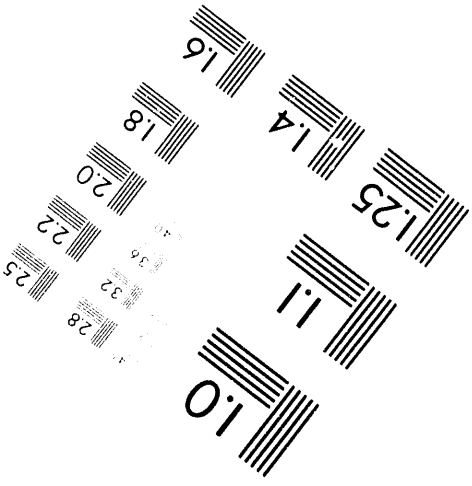


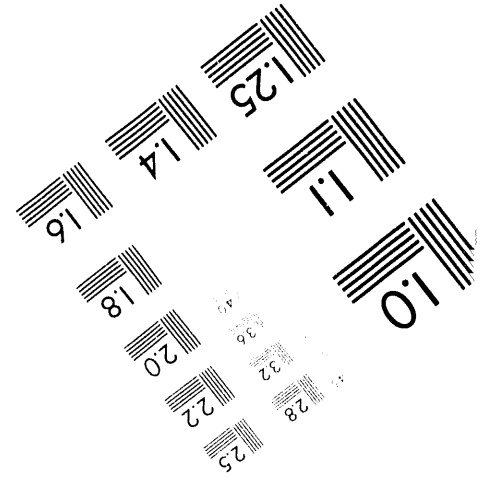


MANUFACTURED TO AIIM STANDARDS
BY APPLIED IMAGE, INC.

2 of 2

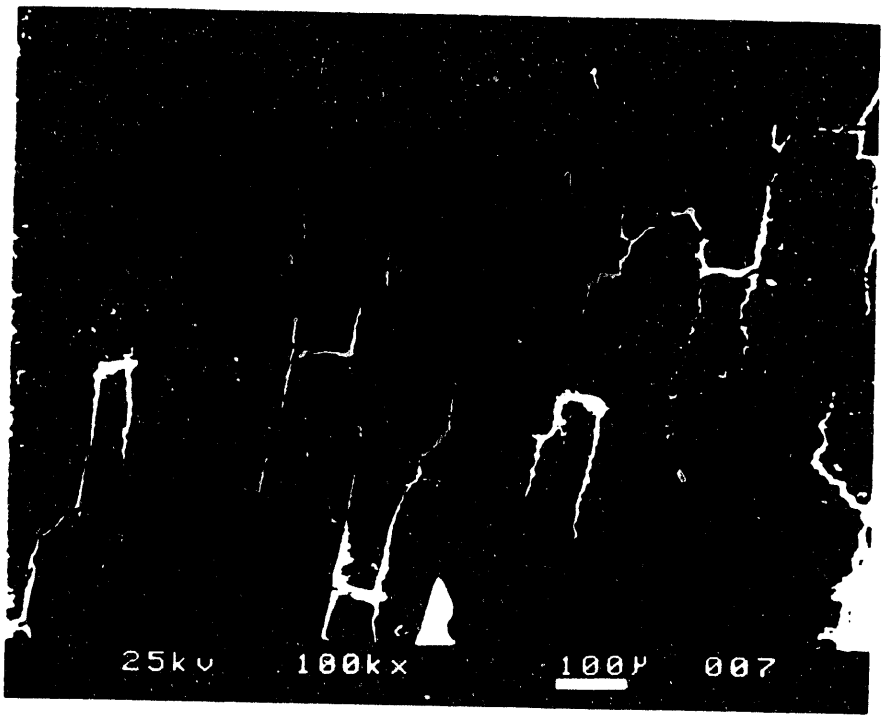


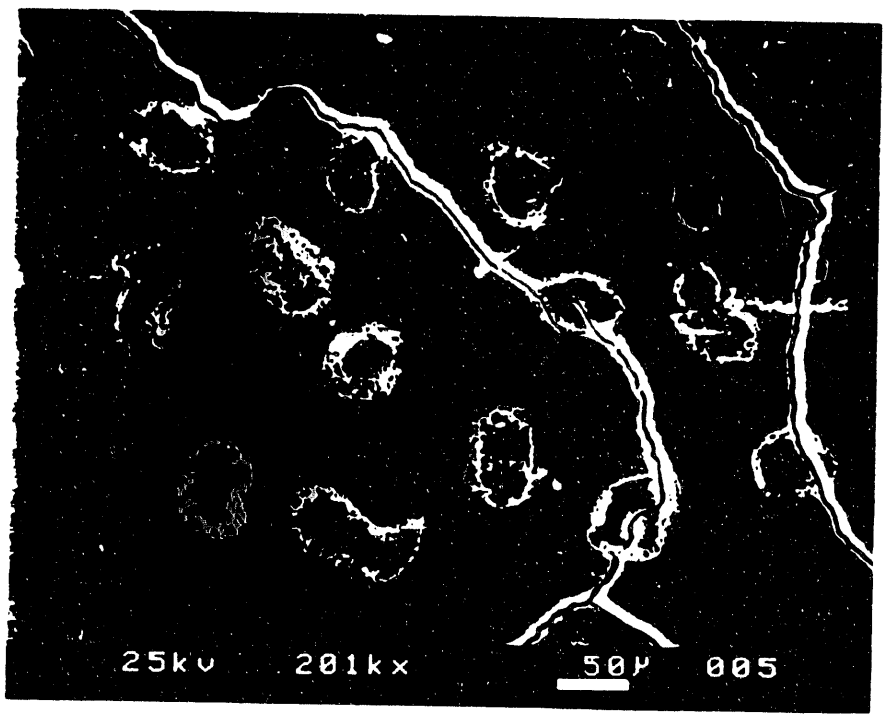


Figure 40. (a) Straight Strips of Deposit Layer on Bottom 321 Stainless Steel Coupon after 5 Hour Reaction at 450 °C, (b) Deposit Layer on Top 321 Stainless Steel Coupon after 5 Hour Reaction at 450 °C.

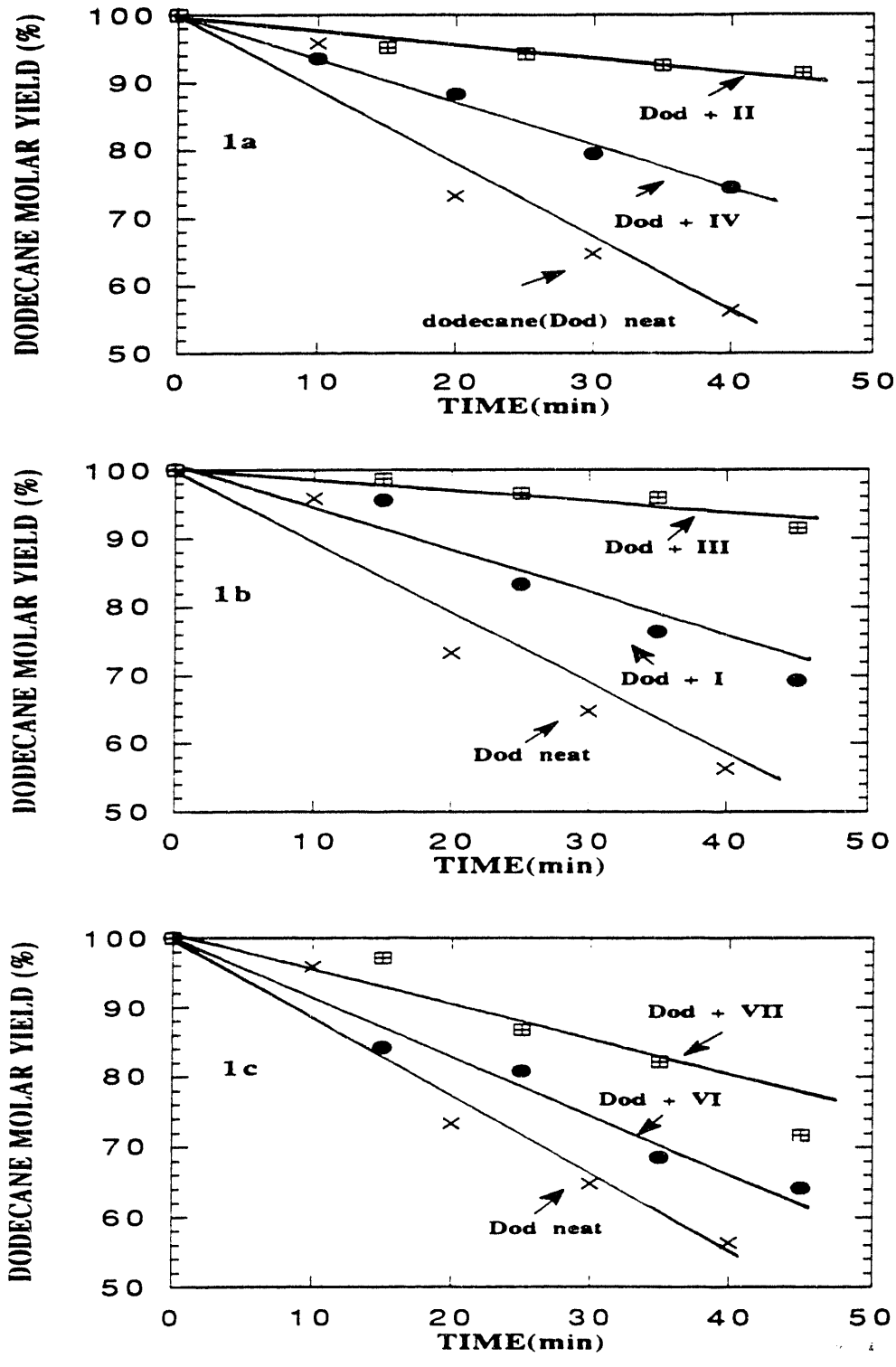


Figure 41. Effects of Hydrogen donor additives (10mol%) I, II, III, IV, VI, and VII on the Molar Yields of Dodecane at 450°C under initial $N_2$ Pressure of 0.69 MPa.

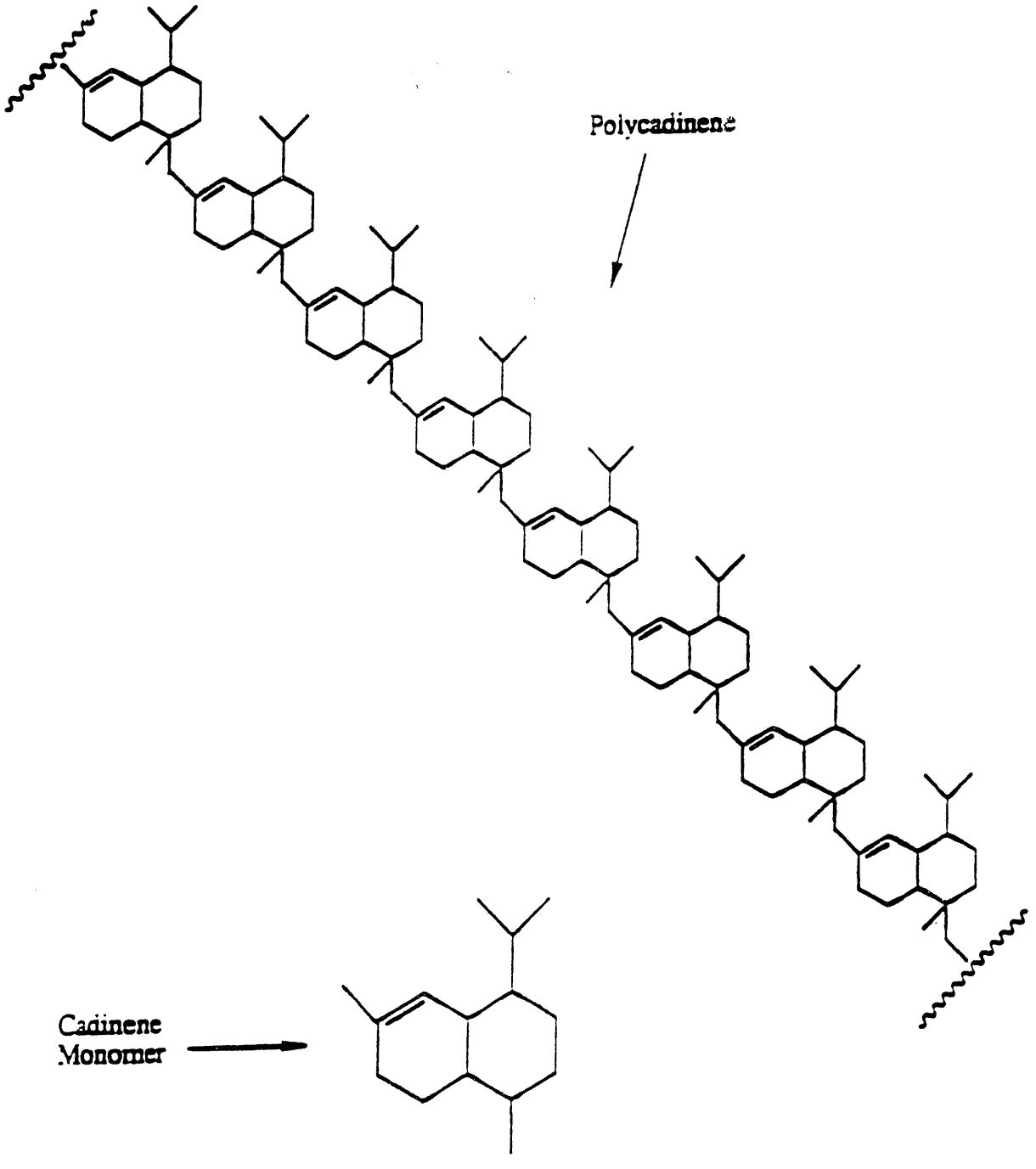


Figure 42. Cadinene and polycadinene structures.

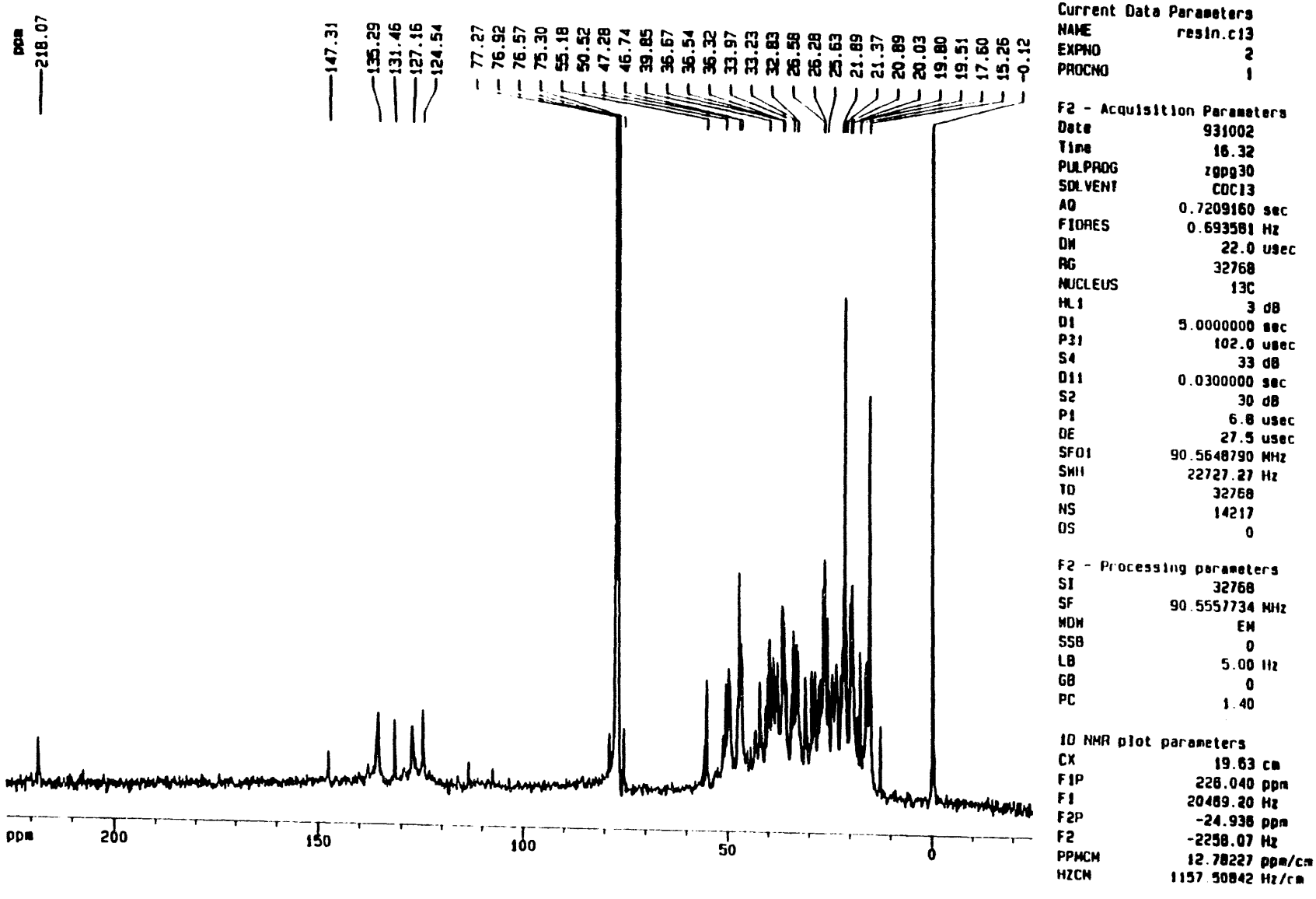


Figure 43. $^{13}C$ broadband decoupled NMR spectrum of Dammar PC in $CDCl_3$.

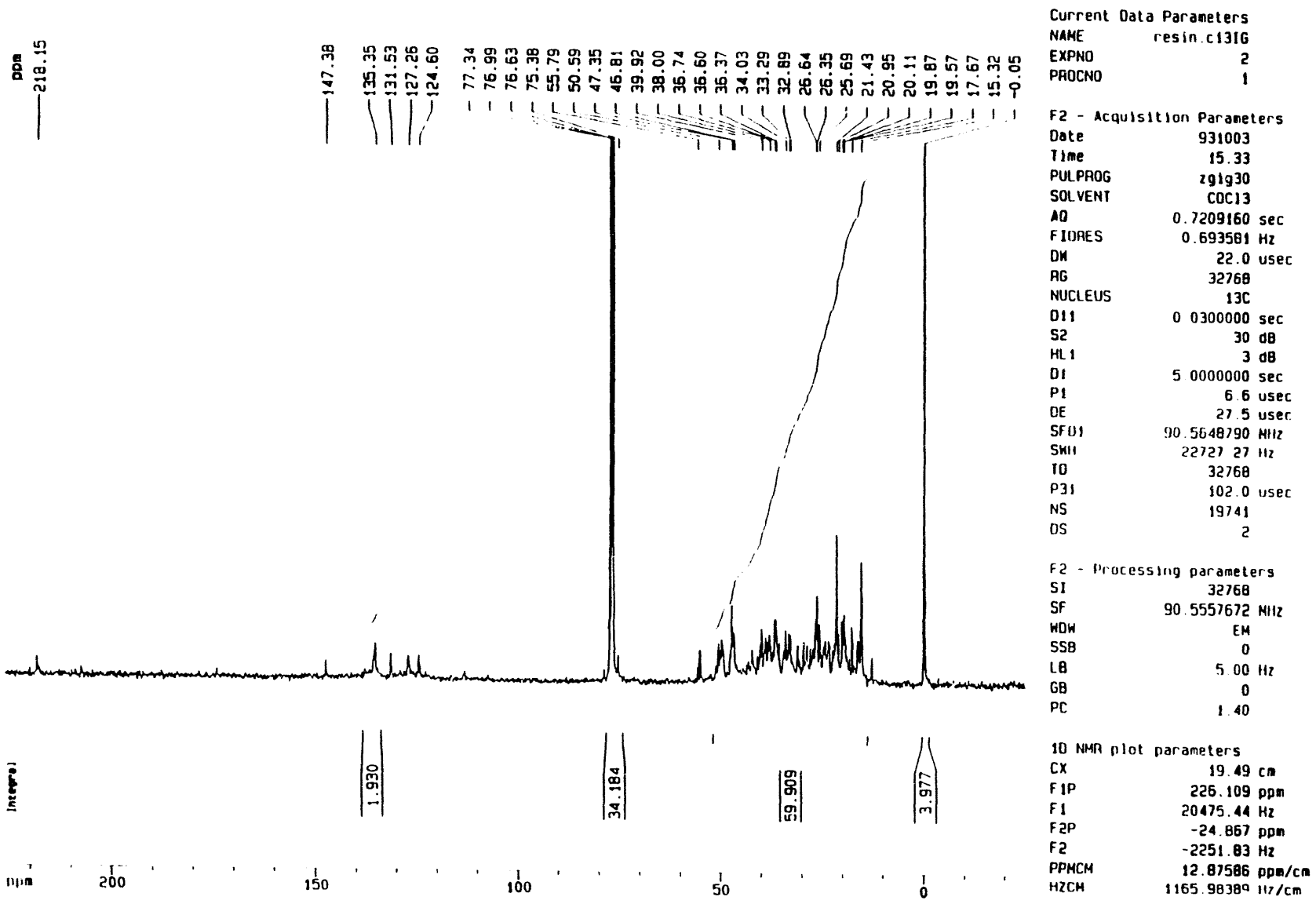


Figure 44. $^{13}C$ inverse-gated NMR spectrum ofpolycadinene from Dammar resin in $CDCl_3$.

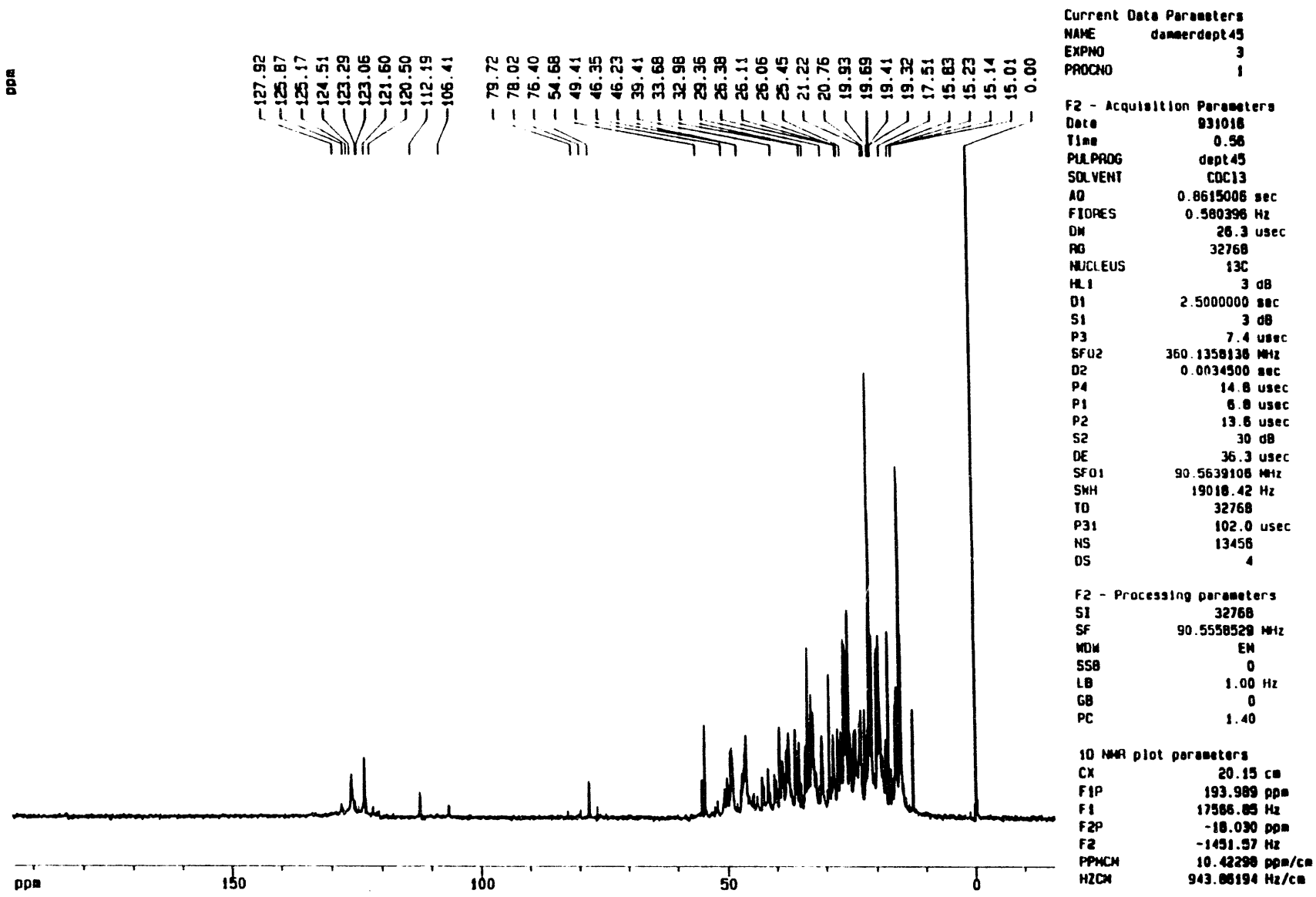


Figure 45. $^{13}C$ DEPT 45° NMR spectrum of Dammar PC in $CDCl_3$.

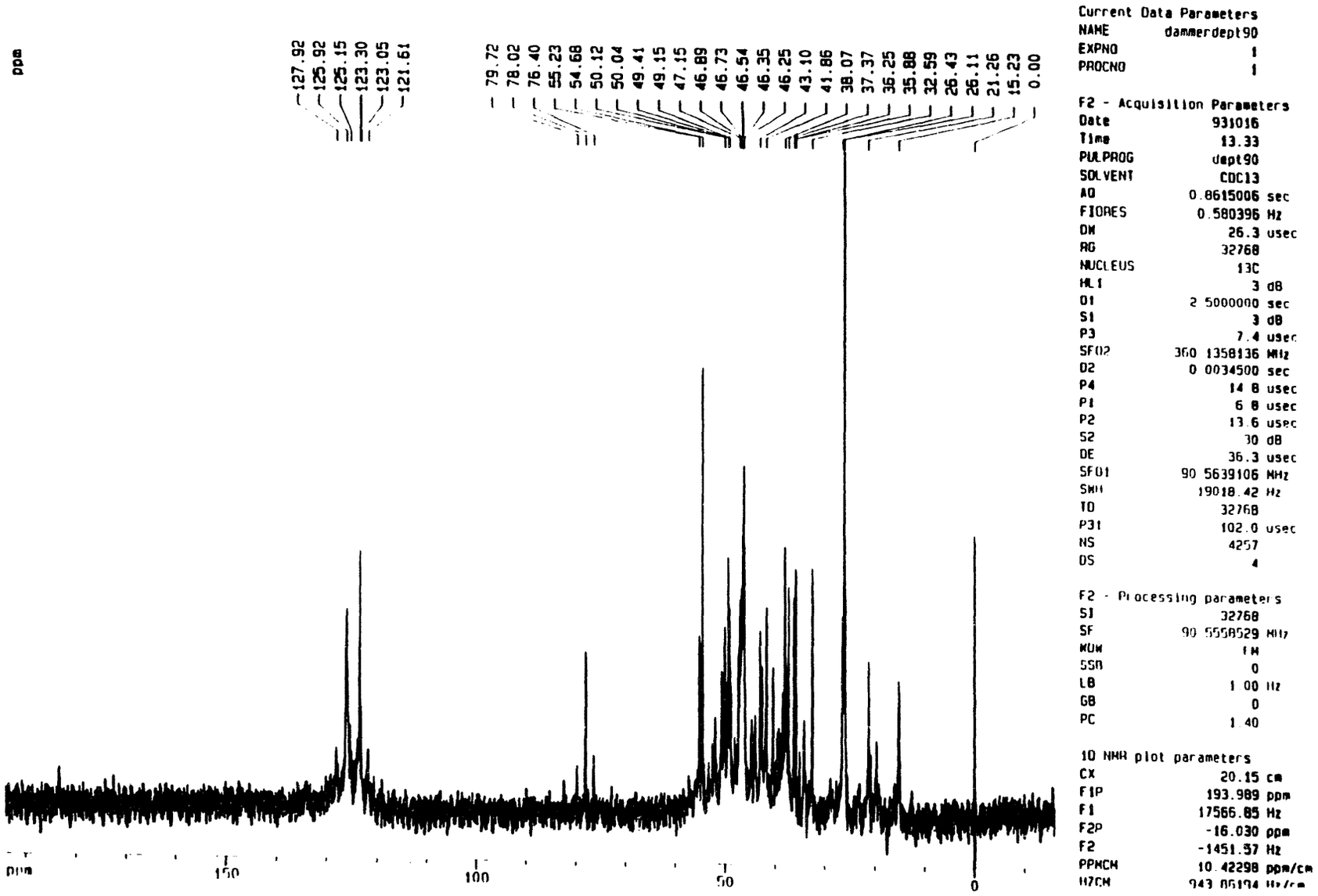


Figure 46. $^{13}C$ DEPT 90° NMR spectrum of Dammar PC in $CDCl_3$.

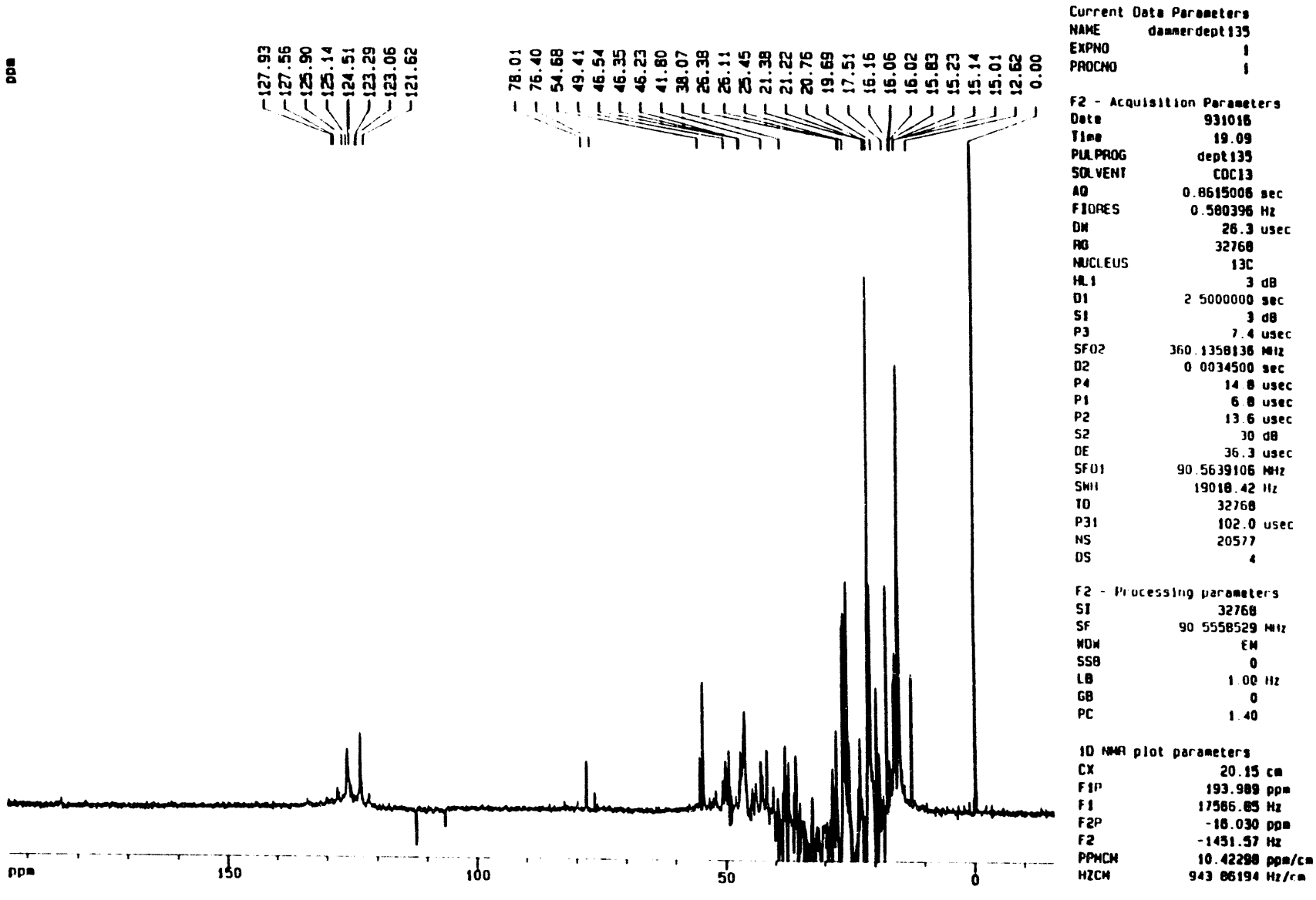


Figure 47. $^{13}C$ DEPT 135° NMR spectrum of Dammar PC in $CDCl_3$.

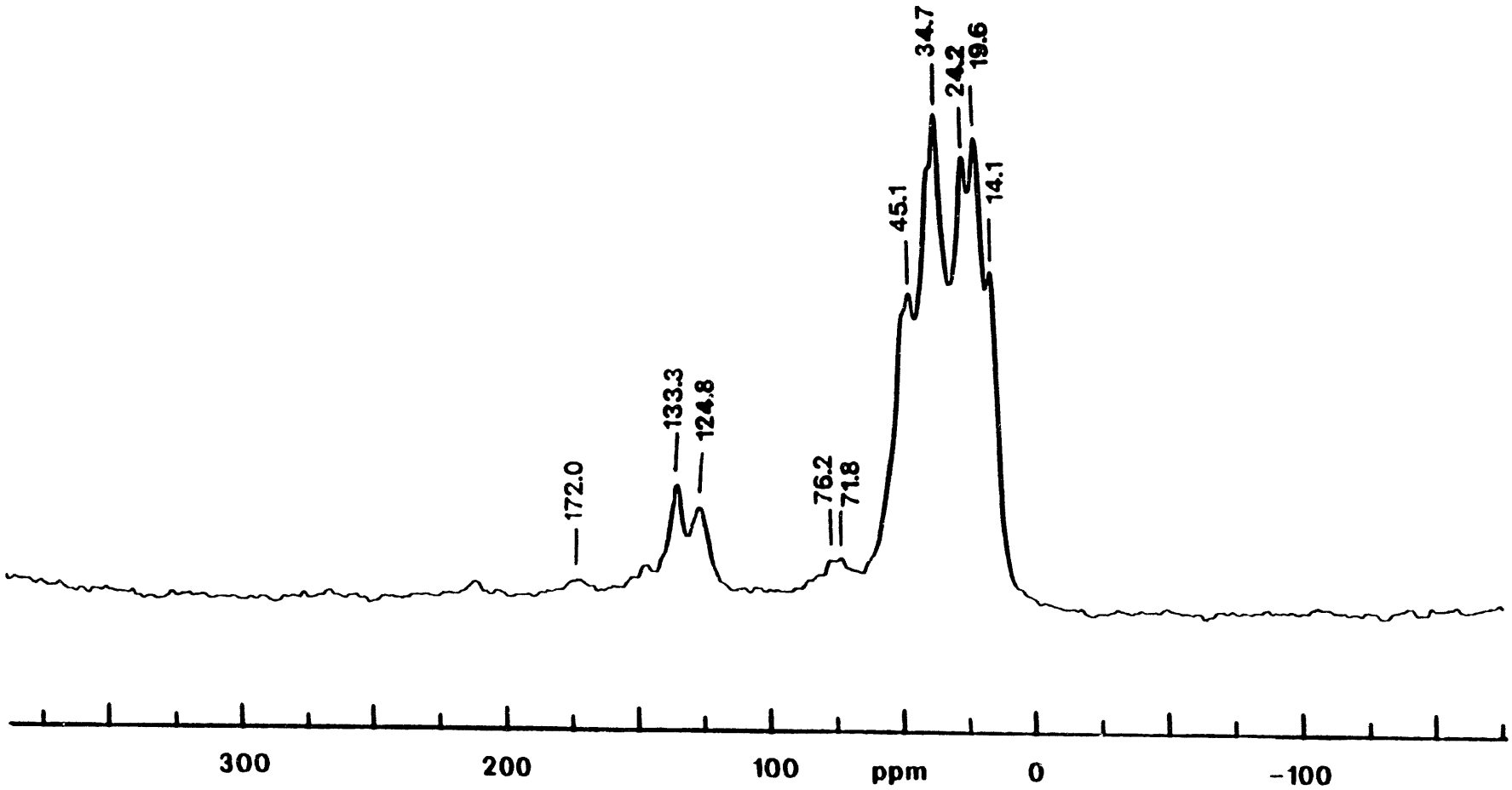


Figure 48. $^{13}C$ CPMAS spectrum of Dammar PC.

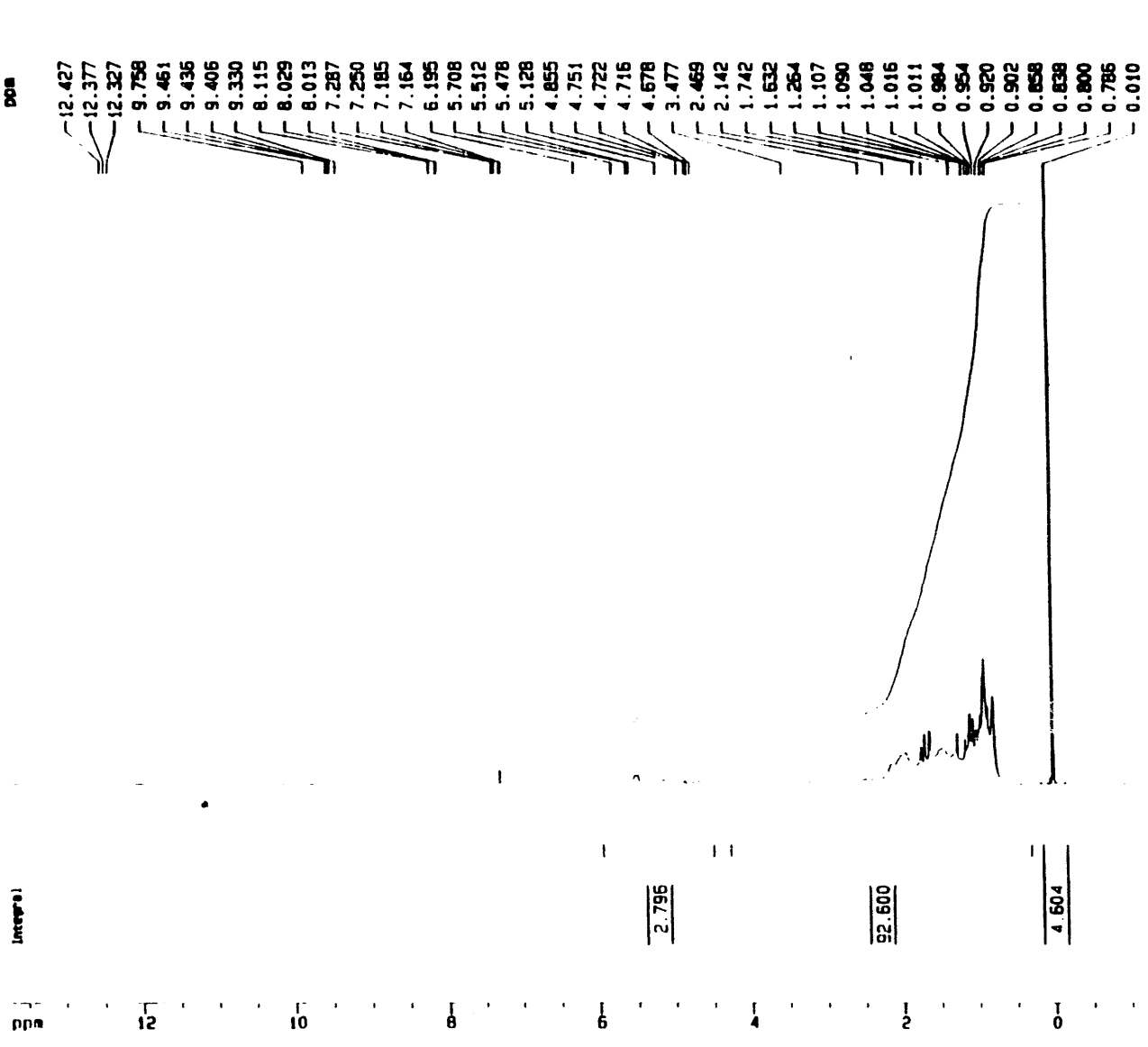


Current Data Parameters

| | |
|---|---|
| NAME | damres.hi |
| EXPNO | 1 |
| PROCNO | 1 |

F2 - Acquisition Parameters

| | |
|---|---|
| Date | 931011 |
| Time | 15.28 |
| PULPROG | zg30 |
| SOLVENT | CDCl3 |
| AQ | 3.0146761 sec |
| FIDRES | 0.165856 Hz |
| DW | 92.0 usec |
| RG | 16 |
| NUCLEUS | 1H |
| HL1 | 3 dB |
| D1 | 2.0000000 sec |
| P1 | 7.9 usec |
| DE | 115.0 usec |
| SFO1 | 360.1362041 MHz |
| SWH | 5434.78 Hz |
| TD | 32768 |
| NS | 32 |
| DS | 0 |

F2 - Processing parameters

| | |
|---|---|
| SI | 16384 |
| SF | 360.1339736 MHz |
| WDW | EM |
| SSB | 0 |
| LB | 0.30 Hz |
| GB | 0 |
| PC | 1.00 |

1D NMR plot parameters

| | |
|---|---|
| CX | 19.02 cm |
| F1P | 13.739 ppm |
| F1 | 4947.83 Hz |
| F2P | -1.352 ppm |
| F2 | -486.96 Hz |
| PPMCM | 0.79326 ppm/cm |
| HZCM | 285.68152 Hz/cm |

Figure 49. $^{1}H$ NMR spectrum of Dammar PC in $CDCl_3$ with 1% TMS.

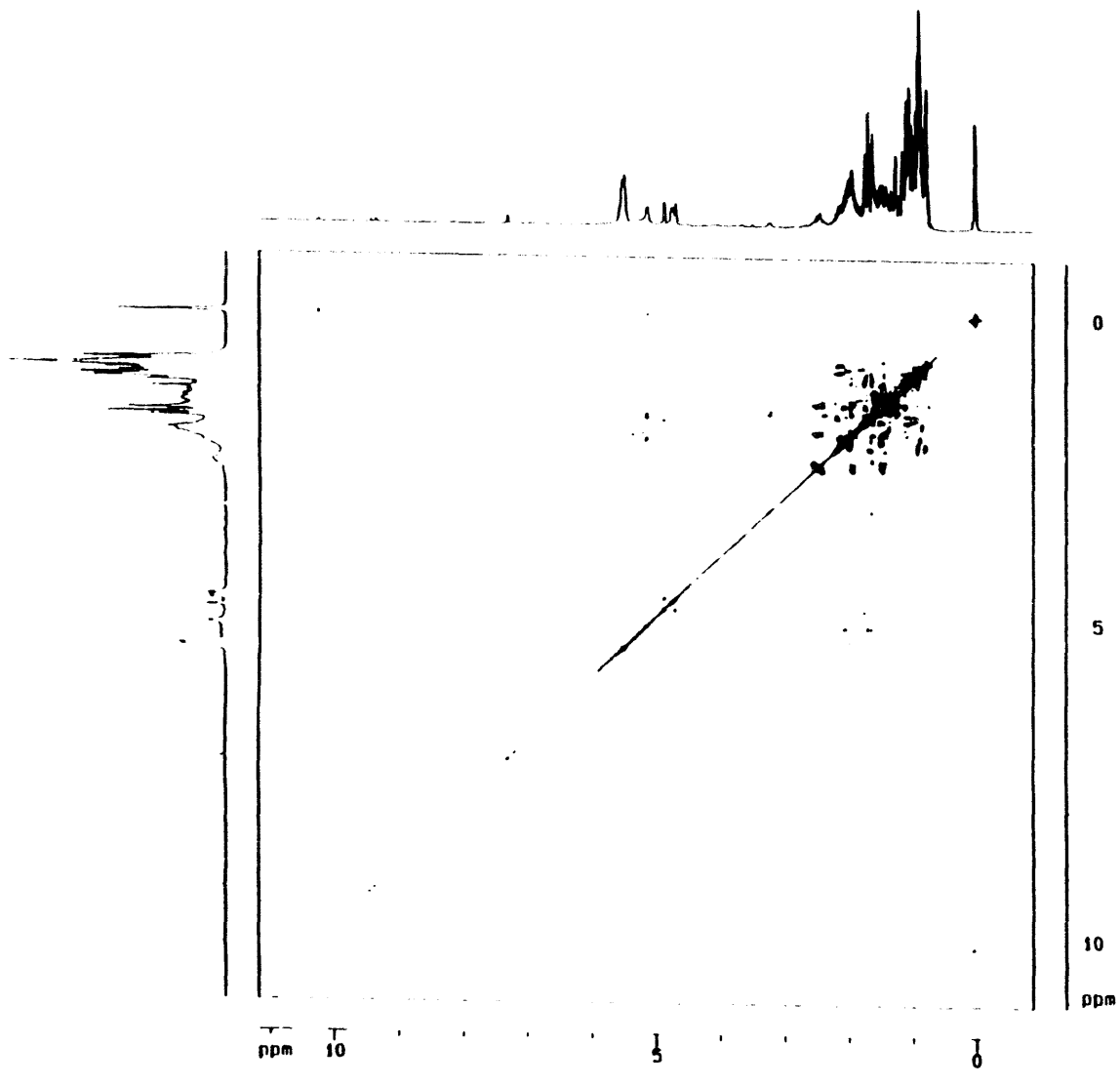


Current Data Parameters

| | |
|---|---|
| NAME | demres2dcosy h |
| EXPNO | 4 |
| PROCNO | 1 |

F2 - Acquisition Parameters

| | |
|---|---|
| Date | 931013 |
| Time | 22.12 |
| PULPROG | cosy45 |
| SOLVENT | cdcl3 |
| AQ | 0.2355480 sec |
| FIDRES | 2.122962 Hz |
| DW | 115.0 usec |
| RG | 32 |
| NUCLEUS | 1H |
| PL1 | 3 dB |
| D1 | 1.0000000 sec |
| P1 | 8.3 usec |
| D0 | 0.0000030 sec |
| DE | 143.8 usec |
| SFO1 | 360.1358136 MHz |
| SWH | 4347.83 Hz |
| TD | 2048 |
| NS | 96 |
| DS | 2 |
| FNO | 0.0002314 sec |

F1 - Acquisition parameters

| | |
|---|---|
| NDO | 1 |
| TD | 512 |
| SFO1 | 360.1372 MHz |
| FIDRES | 8.441715 Hz |
| SW | 12.090 ppm |

F2 - Processing parameters

| | |
|---|---|
| SI | 2048 |
| SF | 360.1313577 MHz |
| WDW | SINE |
| SSB | 0 |
| LB | 0.00 Hz |
| GB | 0 |
| PC | 1.40 |

F1 - Processing parameters

| | |
|---|---|
| SI | 1024 |
| MC2 | QF |
| SF | 360.1353258 MHz |
| WDW | SINE |
| SSB | 0 |
| LB | 0.00 Hz |
| GB | 0 |

2D NMR plot parameters

| | |
|---|---|
| CX2 | 11.85 cm |
| CX1 | 11.85 cm |
| F2PLO | 11.190 ppm |
| F2LO | 4027.82 Hz |
| F2PHI | -0.883 ppm |
| F2HI | -319.01 Hz |
| F1PLO | 11.093 ppm |
| F1LO | 3994.98 Hz |
| F1PHI | -0.907 ppm |
| F1HI | -326.86 Hz |
| F2PPMCM | 1.01080 ppm/cm |
| F2HZCM | 368.90585 Hz/cm |
| F1PPMCM | 1.01264 ppm/cm |
| F1HZCM | 369.57481 Hz/cm |

Figure 50. $^{1}H$-$^{1}H$ correlation spectrum (COSY 45°) of Dammar PC in $CDCl_3$.

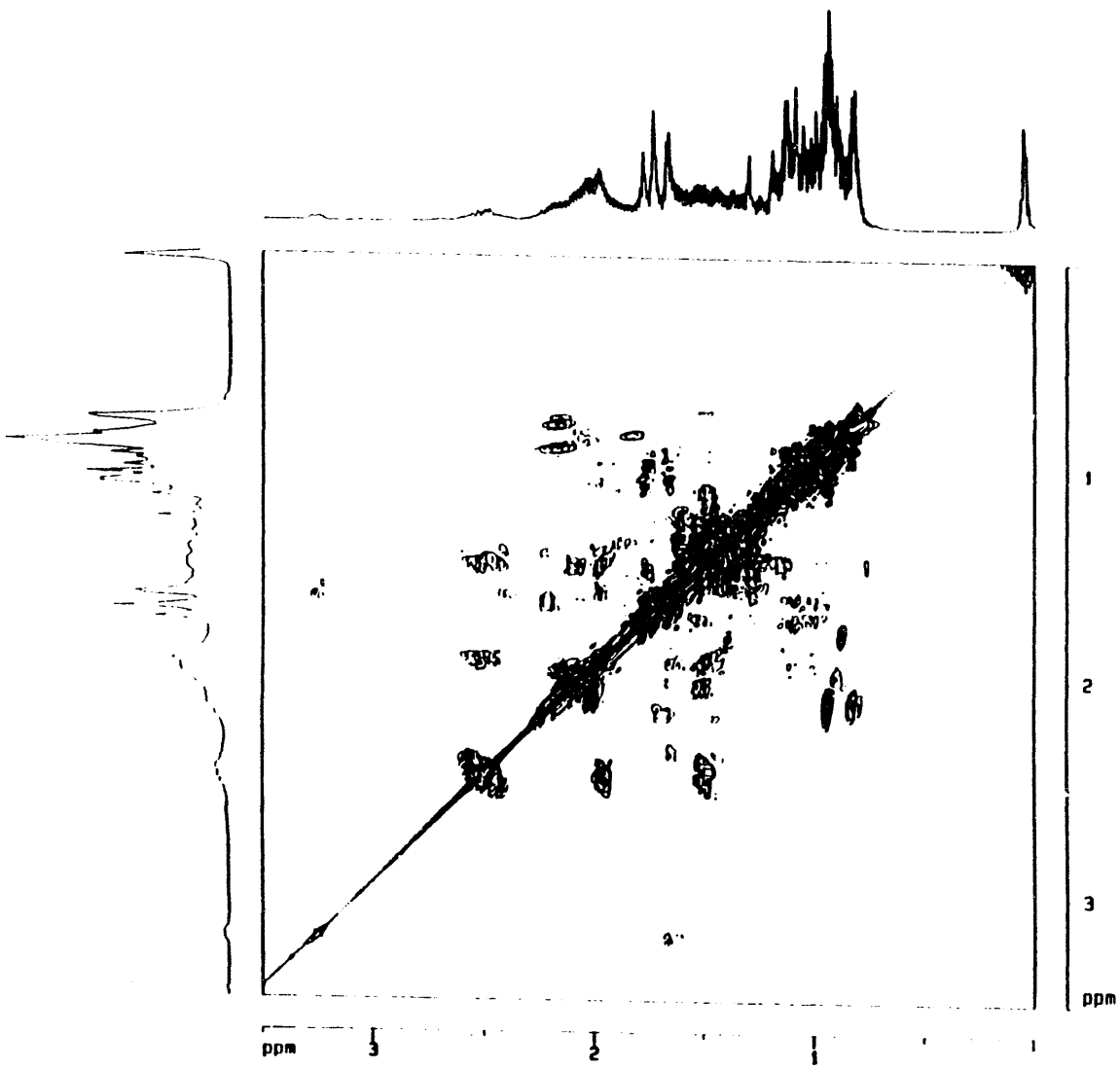


Current Data Parameters

| | |
|---|---|
| NAME | dewres2dcosy h |
| EXPNO | 4 |
| PROCNO | 1 |

F2 Acquisition Parameters

| | |
|---|---|
| Date | 931013 |
| Time | 22.12 |
| PULPROG | cosy45 |
| SOLVENT | cdcl3 |
| AQ | 0.2355400 sec |
| FIDRES | 2.122962 Hz |
| DW | 115.0 usec |
| RG | 32 |
| NUCLEUS | 1H |
| NL1 | 3 dB |
| D1 | 1.0000000 sec |
| P1 | 8.3 usec |
| D0 | 0.0000030 sec |
| DE | 143.8 usec |
| SFO1 | 350.1358136 MHz |
| SW1 | 4347.83 Hz |
| TD | 2048 |
| MS | 96 |
| DS | 2 |
| TD0 | 0.0002314 sec |

F1 Acquisition parameters

| | |
|---|---|
| ND0 | 1 |
| TD | 512 |
| SFO1 | 350.1372 MHz |
| FIDRES | 8.449715 Hz |
| SW | 12.000 ppm |

F2 Processing parameters

| | |
|---|---|
| SI | 2048 |
| SF | 350.1113577 MHz |
| WDW | SINE |
| SSB | 0 |
| LB | 0.00 Hz |
| GB | 0 |
| PC | 1.40 |

F1 Processing parameters

| | |
|---|---|
| SI | 1024 |
| MC2 | QF |
| SF | 350.1353258 MHz |
| WDW | SINE |
| SSB | 0 |
| LB | 0.00 Hz |
| GB | 0 |

2D NMR plot parameters

| | |
|---|---|
| CX2 | 11.05 cm |
| CX1 | 11.05 cm |
| F2PLO | 3.500 ppm |
| F2LO | 1260.47 Hz |
| F2PHI | -0.005 ppm |
| F2HI | -1.80 Hz |
| F1PLO | 3.500 ppm |
| F1LO | 1260.47 Hz |
| F1PHI | -0.005 ppm |
| F1HI | -1.69 Hz |
| F2PPMCM | 0.29575 ppm/cm |
| F2HZCM | 106.51007 Hz/cm |
| F1PPMCM | 0.29576 ppm/cm |
| F1HZCM | 106.51200 Hz/cm |

**Figure 51. Expanded $^{1}H$-$^{1}H$ correlation spectrum (COSY 45°) of Dammar PC in $CDCl_3$ (0.0 ppm -3.5 ppm).**

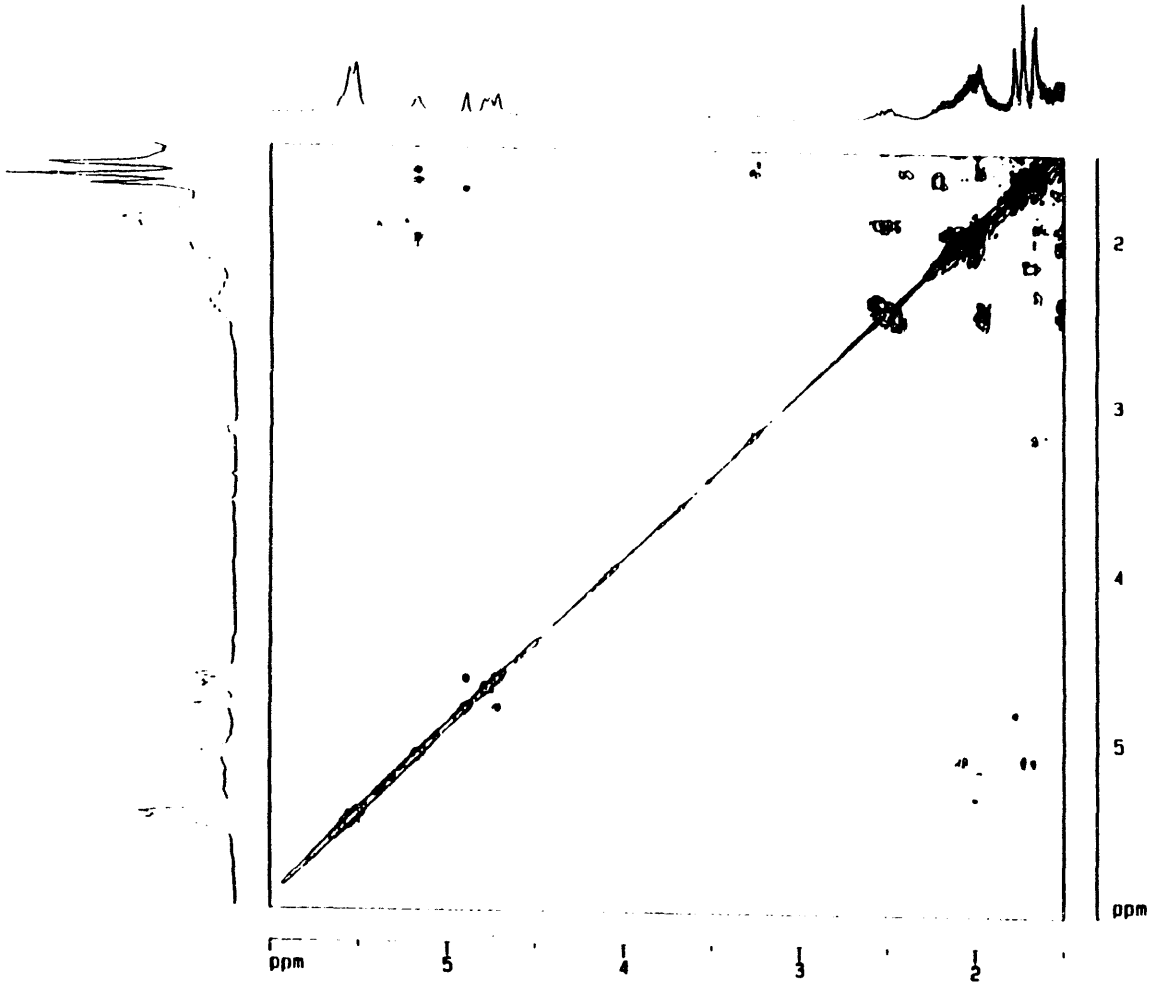


Current Data Parameters

| | |
|---|---|
| NAME | demres2dcosy h |
| EXPNO | 4 |
| PROCNO | 1 |

F2 Acquisition Parameters

| | |
|---|---|
| Date | 931013 |
| Time | 22.12 |
| PULPROG | cosy45 |
| SOLVENT | cdcl3 |
| AQ | 0.2355400 sec |
| FIDRES | 2.122962 Hz |
| DW | 115.0 usec |
| RG | 32 |
| NUCLEUS | 1H |
| HL1 | 3 dB |
| D1 | 1.0000000 sec |
| P1 | 8.3 usec |
| D0 | 0.0000030 sec |
| DE | 143.8 usec |
| SFO1 | 360.1350136 MHz |
| SW1 | 4147.83 Hz |
| TD | 2048 |
| NS | 16 |
| DS | 2 |
| TD0 | 0.0002314 sec |

F1 Acquisition parameters

| | |
|---|---|
| NDO | 1 |
| TD | 512 |
| SFO1 | 360.1372 MHz |
| FIDRES | 8.449715 Hz |
| SW | 12.000 ppm |

F2 Processing parameters

| | |
|---|---|
| SI | 2048 |
| SF | 360.1313577 MHz |
| WDW | SINE |
| SSB | 0 |
| LB | 0.00 Hz |
| GB | 0 |
| PC | 1.00 |

F1 Processing parameters

| | |
|---|---|
| SI | 1024 |
| MC2 | QF |
| SF | 360.1313578 MHz |
| WDW | SINE |
| SSB | 0 |
| LB | 0.00 Hz |
| GB | 0 |

2D plot parameters

| | |
|---|---|
| CX2 | 11.85 cm |
| CY1 | 11.85 cm |
| F2PLO | 6.402 ppm |
| F2LO | 2181.81 Hz |
| F2PHI | 1.493 ppm |
| F2HI | 531.67 Hz |
| F1PLO | 8.007 ppm |
| F1LO | 2163.35 Hz |
| F1PHI | 1.500 ppm |
| F1HI | 540.20 Hz |
| F2PPMCM | 0.38006 ppm/cm |
| F2HZCM | 196.87282 Hz/cm |
| F1PPMCM | 0.38034 ppm/cm |
| F1HZCM | 196.97438 Hz/cm |

Figure 52. Expanded $^{1}H$-$^{1}H$ correlation spectrum (COSY 45°) of Dammar PC in $CDCl_3$ (1.0 ppm -6.0 ppm).

DATE
FILMED
7/5/94
END